ORNL/TM-11525

ornl

OAK RIDGE NATIONAL LABORATORY

MARTIN MARIETTA

Subsidence of Residual Soils in a Karst Terrain

E. C. Drumm
W. F. Kane
R. H. Ketelle
J. Ben-Hassine
J. A. Scarborough

OPERATED BY
MARTIN MARIETTA ENERGY SYSTEMS, INC.
FOR THE UNITED STATES
DEPARTMENT OF ENERGY

ORNL/TM-11525

ENERGY DIVISION

SUBSIDENCE OF RESIDUAL SOILS IN A KARST TERRAIN

E. C. Drumm*
W. F. Kane*
R. H. Ketelle
J. Ben-Hassine*
J. A. Scarborough*

Date Published—June 1990

*The University of Tennessee, Knoxville

Prepared by the
OAK RIDGE NATIONAL LABORATORY
Oak Ridge, Tennessee 37831
operated by
MARTIN MARIETTA ENERGY SYSTEMS, INC.
for the
U.S. DEPARTMENT OF ENERGY
under Contract No. DE-AC05-84OR21400

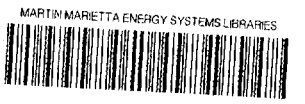

TABLE OF CONTENTS

Page

LIST OF FIGURES v

LIST OF TABLES vii

ACKNOWLEDGMENT ix

ABSTRACT xi

1. INTRODUCTION 1
   1.1 PROBLEM STATEMENT 1
   1.2 NOTE ON UNITS 1

2. REVIEW OF PREVIOUS INVESTIGATIONS 5
   2.1 PREVIOUS SOIL MECHANICS ANALYSES 5
   2.2 REGIONAL SINKHOLE OCCURRENCE 5
      2.2.1 Additional Interpretation of Regional Subsidence Data 5

3. SITE CHARACTERISTICS 11
   3.1 GEOLOGY 11
   3.2 SOIL PROPERTIES 11
      3.2.1 East Chestnut Ridge 11
      3.2.2 West Chestnut Ridge Site 14

4. SINKHOLE MEASUREMENTS AND PROFILE FUNCTION ANALYSIS FOR THE EAST CHESTNUT RIDGE SITE 17
   4.1 FIELD SINKHOLE MEASUREMENTS 17
      4.1.1 Description of Survey Methods 17
      4.1.2 Results 19
   4.2 PROFILE FUNCTIONS 19
      4.2.1 General Description of Profile Functions 19
      4.2.2 Profile Function Parameters for the East Chestnut Ridge 23
   4.3 SUMMARY OF PROFILE FUNCTION STUDY 23

5. NUMERICAL ANALYSIS OF STABILITY 27
   5.1 ANALYTICAL APPROACH 27
      5.1.1 Background and Idealization of a Soil Void 27
      5.1.2 Analytical Assumptions 27
   5.2 CONSTITUTIVE MODEL AND CHARACTERIZATION OF MATERIAL RESPONSE 30
      5.2.1 Linear Elastic Model 30
      5.2.2 Hyperbolic Elastic Model 32
      5.2.3 Elastic-Plastic Cap Model 33

TABLE OF CONTENTS (continued)

Page

5.3 CONSIDERATIONS IN NONLINEAR ANALYSIS 33
5.4 STABILITY ANALYSIS OF SOIL VOID/BEDROCK CAVITY SYSTEM .. 34
5.4.1 Range of Site Geometries 34
5.4.2 Results of Stability Analysis 35

6. SUBSIDENCE PREDICTION USING A HYBRID APPROACH 47
6.1 DEVELOPMENT OF THE HYBRID APPROACH USING A HYPERBOLIC MODEL 47
6.2 SUBSIDENCE PREDICTION USING THE CAP MODEL 50

7. CONCLUSIONS AND RECOMMENDATIONS 57
7.1 CONCLUSIONS 57
7.2 RECOMMENDATIONS FOR FURTHER STUDY 58
7.2.1 Effects of Factors Not Considered in Current Analysis 58
7.2.2 Application of Results and Verification by Field Studies 59

REFERENCES 61

APPENDIX A: CONTOUR MAPS OF SINKHOLES 63
APPENDIX B: DETERMINATION OF CAP MODEL PARAMETERS 75
APPENDIX C: SUMMARY OF ANALYSIS RESULTS—EMPIRICAL AND GEOMETRIC PARAMETERS 83

LIST OF FIGURES

FIGURE		Page
1.1	Location of East Chestnut Ridge study site.	3
2.1	Regional frequency histogram summarizing dates of sinkhole occurrences.	6
2.2	Regional frequency histogram summarizing sinkhole depth	7
2.3	Frequency histogram of regional overburden thickness	7
2.4	Regional histogram of water table depths and sinkhole frequency	8
2.5	The effect of rainfall on regional sinkhole occurrence	8
2.6	Regional water table elevation with respect to bedrock	9
3.1	Plasticity chart for East Chestnut Ridge soils.	12
3.2	Soil classifications at East Chestnut Ridge site.	12
3.3	Plasticity index as a function of depth for East Chestnut Ridge.	13
3.4	Liquidity index as a function of depth for East Chestnut Ridge.	13
3.5	Plasticity chart for West Chestnut Ridge soils.	14
3.6	U.S.C.S. soil classifications for West Chestnut Ridge.	15
3.7	Plasticity Index as a function of elevation above the bedrock surface for West Chestnut Ridge.	15
3.8	Variation in liquidity index with proximity to bedrock for West Chestnut Ridge.	16
4.1	Karst features used to determine profile functions.	18
4.2	Survey grid used in field mapping.	19
4.3	Generic hyperbolic tangent profile and definitions of terms.	21
4.4	Generic negative exponential profile and definition of terms.	22
4.5	Idealized orientation of profiles, plan view.	24
4.6	Typical profile and best fit of the negative exponential function.	24
4.7	Best fit of hyperbolic tangent function to actual field data.	25
5.1	Evolution of a sinkhole	28
5.2	Typical finite element (FE) idealization of residual soil/bedrock cavity system, H = 30 m, r_v = 4 m.	29
5.3	Idealized representation used in finite element (FE) analysis.	31
5.4	Deformed Finite Element Mesh, r_v = 2.0 m, H = 30 m	36
5.5	Displacement vectors, r_v = 2 m, H = 30 m	37
5.6	Magnitudes and orientations of principal stress vectors, r_v = 2 m, H = 30 m.	38
5.7	Zoom on principal stresses around soil void, r_v = 2 m, H = 30 m.	39
5.8	Effect of Increasing Void Radius, H = 30 m	41
5.9	Effect of Decreasing Overburden Thickness, r_v = 3.0 m.	42
5.10	Stress states: r_v = 3.0 m, H = 45 m	43
5.11	Stress states r_v = 3.0 m, H = 15 m.	44

LIST OF FIGURES (continued)

FIGURE		Page
6.1	Comparison of profile function with results of numerical analysis, H = 45 m.	49
6.2	Angle of draw obtained from numerical analysis.	49
6.3	Comparison of field measurement with hybrid method for various r_v.	51
6.4	Exponential relationship between cavity radius and maximum subsidence from the cap model analysis.	52
6.5	Angle of draw from the cap model analysis.	52
6.6.	Location of the inflection point relative to basin half-width from the numerical analysis	54
6.7	Comparison of profiles from the cap model, H = 45 m, with field profiles.	54
6.8	Comparison of profile function results from hybrid cap model with sinkhole 04 field profiles, H = 45 m.	55
B.1	Shear strength of undisturbed samples in stress invariant space.	76
B.2	Deviator stress-axial strain response, Sample ST-9.	79
B.3	Hydrostatic stress-volumetric strain response	80
B.4	Deviator stress-axial strain response for sample ST-16	80
B.5	Finite element simulation of triaxial response	81

LIST OF TABLES

TABLE		Page
4.1	Profile functions	21
5.1	Summary of cap model parameters	34
5.2	Summary of investigated overburden thicknesses and soil void radii	35
5.3	Stability summary on the basis of tensile stress	45
5.4	Stability summary in terms of r_v/H	45
5.5	Stability summary in terms of r_v/H^2	46
6.1	Material parameters for hyperbolic model	47
B.1	Summary of cap model parameters	77

ACKNOWLEDGMENT

The authors would like to acknowledge C. Kinton of The Department of Civil Engineering, The University of Tennessee, Knoxville for his assistance in field surveying and statistical analysis.

ABSTRACT

Previous work on the stability of karst sites in the Oak Ridge National Laboratory area is evaluated and analyzed. It was found that the depth to bedrock is significant in the formation of dropouts. In addition, little variation actually exists in the properties of the overburden residual soils.

The vertical displacement, slope, and curvature of a surface profile are major factors contributing to structural damage. Therefore, a site specific model to predict the lateral and vertical extent of sinkhole subsidence was developed. The deformation of the surface was studied using a hybrid approach of numerical and empirical analysis. This approach incorporated field measurements, laboratory test data on soil strength, and the numerical analysis of typical soil profiles and hypothetical cavity dimensions.

Empirical profile functions were used to describe completely a continuous profile for a sinkhole subsidence basin. Statistical and analytical procedures were used to predict the magnitude and shapes of surface subsidence profiles. Two-dimensional, nonlinear, finite element analysis was conducted to evaluate the stability of a soil void in a thick, residual clay above a discontinuity in rigid bedrock. This numerical analysis included a prototypical approach to quantifying relationships for the subsurface geometry that drives surface deformation.

The shape of karst features in the East Chestnut Ridge site could be described by the empirical function:

$$S(x) = S_0 \, e^{-\alpha\left(\frac{x}{0.56H}\right)^{\beta}} ,$$

where S_0 = maximum subsidence = $e^{-5.46 + 2.04 r_v}$, $\alpha = 2.50$ and $\beta = 3.30$ are site specific empirical parameters, and r_v, X, and H define geometry.

For the East Chestnut Ridge site, it was found that size of a soil void for a given soil thickness controls the magnitude of surface subsidence experienced. When the ratio of soil void radius to the square of soil thickness (r/H^2) remains below approximately 0.003, stability can be assumed.

1. INTRODUCTION

1.1 PROBLEM STATEMENT

Siting and operating landfills for solid waste disposal in eastern Tennessee that can operate with minimum impact on groundwater is problematic. The operational requirement of thick, excavational soils and the regulatory requirement of a buffer between disposal units and an aquifer result in siting most operating East Tennessee landfills in outcrop areas of the Knox Group. The Knox Group is dominated by dolostone bedrock, which commonly has thick residual soils and deep water tables, making this setting suitable for meeting both operational and regulatory requirements. However, the common occurrence of karst terrain and sinkholes in the Knox Group indicates the vulnerability of such sites to rapid groundwater recharge and flow and the potential for subsidence or collapse of soil into bedrock cavities. Subsidence or collapse of soils beneath disposal units poses the threat of allowing rapid migration of waste leachate into an aquifer.

To address the potential for subsidence or collapse of soils at the East Chestnut Ridge site (Fig. 1.1) on the Department of Energy's (DOE) Oak Ridge Reservation (ORR), the following activities and analyses were completed.

- The locations of karst features on the site were determined by field reconnaissance.
- Several sinkholes were selected for detailed examination.
- Soil boring, sampling, and physical testing were performed in soils located within, adjacent to, and outside of sinkholes to characterize soil strength at various depths.
- Detailed plane surveys were made for 11 sinkholes to measure accurately their dimension and shape for use in determining profile functions for subsidence basins at the site.
- Based on soil properties determined in the laboratory testing program, the stress-deformation response of a typical soil profile overlying a hypothetical bedrock cavity was analyzed numerically for a range of soil thicknesses and a range of cavity radii.
- Through a synthesis of the profile function analysis and the numerical analysis of soil behavior, a consistent estimate of the relationship between subsidence basin dimension, soil thickness, and cavity radius has been derived.

This study is limited to subsidence where the profile of the deformed surface, or *subsidence basin,* is continuous. Regional surveys of karst activity in eastern Tennessee suggest that collapse, resulting in a discontinuous profile, is a more likely type of failure (Newton and Tanner 1986). Subsidence, however, has been noted as a precursor to collapse (Newton 1976).

1.2 NOTE ON UNITS

As yet there is no agreed upon standard for units. Most professional journals with an international circulation require the use of Systeme International (SI) units. Most practicing engineers and the construction industry in the United States, however, use the English system of units. The surveying for this program was performed using instruments calibrated in the English system. For accuracy, all surveying data are furnished in English units. In addition,

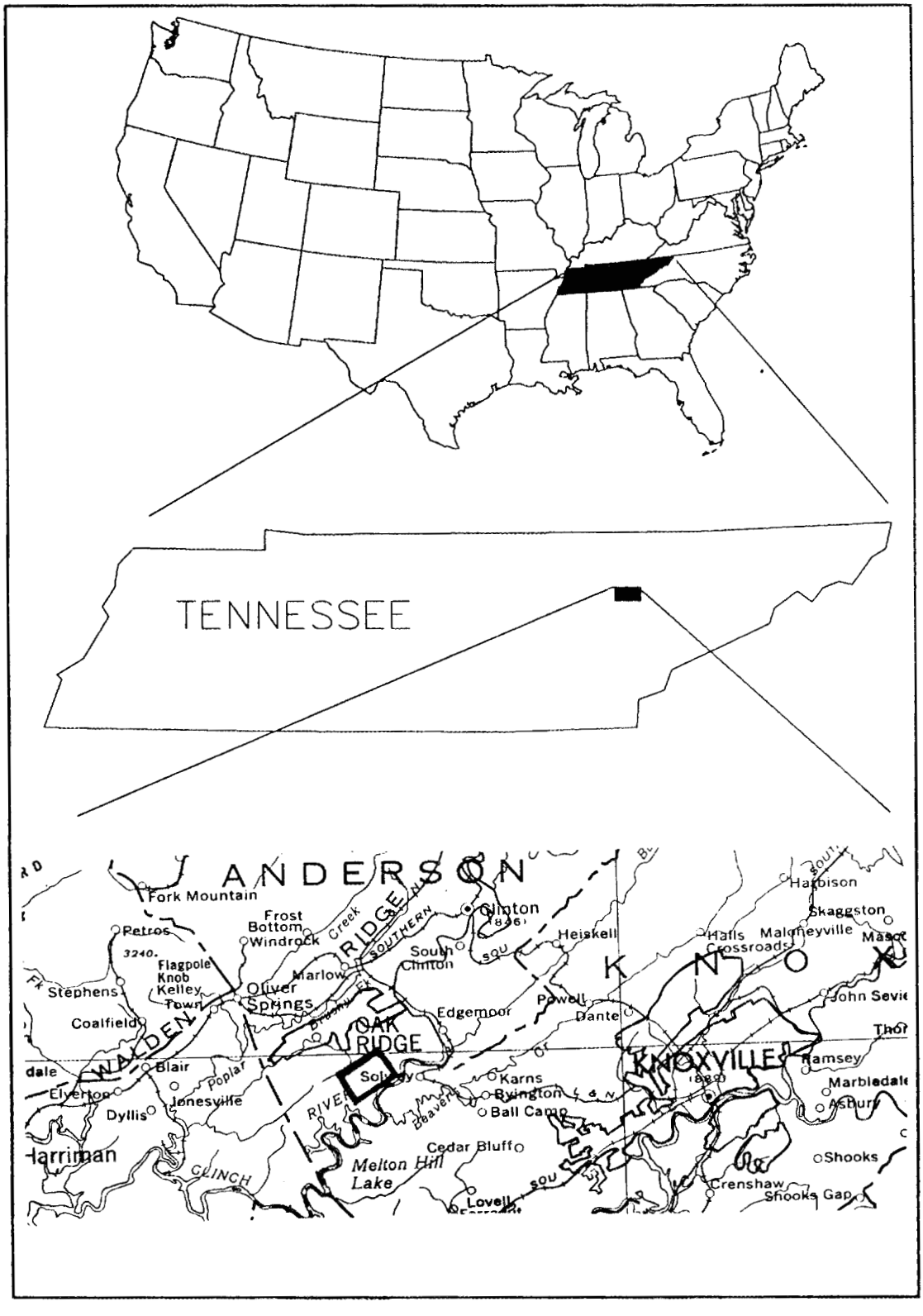

Fig. 1.1. Location of East Chestnut Ridge study site.

previous work performed for ORNL has been done using English units. Conventional laboratory test results are also reported in English units. The analyses conducted for this research were carried out using the SI system of units. To maintain accuracy and to be in line with today's international perspective, these results are reported in SI units.

2. REVIEW OF PREVIOUS INVESTIGATIONS

Previous investigations relevant to the study reported here include soil mechanics analyses performed at West Chestnut Ridge at Oak Ridge, Tennessee, and studies of karst subsidence in East Tennessee. Results of these previous studies were incorporated in this work.

2.1 PREVIOUS SOIL MECHANICS ANALYSES

The West Chestnut Ridge site was evaluated with respect to deformation and collapse of the residual soil into the bedrock cavities (Ben-Hassine 1987; Drumm et al. 1987; Ketelle et al. 1987). This site is similar to the East Chestnut Ridge site, with thick residual soils overlying weathered bedrock containing numerous solution cavities. Numerous karst features were identified on the West Chestnut Ridge site (Ketelle and Huff 1984).

A finite element analysis was conducted to investigate the effects of bedrock cavity radius, thickness of soil overburden, and surface surcharge upon the deformational and stability characteristics of the residual soil (Drumm et al. 1987). The soil was assumed to span a circular cavity in the rigid bedrock, with gravitational forces causing displacement of the soil into the bedrock cavity. Axisymmetric conditions were assumed in the analysis, and an elastic-plastic constitutive model was used to represent the residual soil. Because of limitations in the existing field and laboratory data, several major assumptions were made to determine the constitutive parameters. These assumptions will be discussed later in the report (see Sect. 5–6). Qualitative conclusions, however, regarding the stability of various combinations of overburden thickness and cavity radius could be drawn from the analysis results.

Results indicated that for small bedrock cavity radii, the thickness of the soil cover has little effect on the size of the yielded soil zone. For large cavity radii, a smaller zone of distressed soil occurs under thick soil cover than under thin soil cover. Dimensionless curves were presented to enable the prediction of the vertical extent of the zone of yielded soil for a range of site geometries. Although the thick soil deposits [30 m (98 ft) or greater] typically found on the ridges resulted in high stresses adjacent to the cavity, the area of the distressed or yielded soil was small and unlikely to extend to the surface. The magnitude of the surface deformation or subsidence was predicted to be minimal.

It was concluded that the siting of waste facilities on the ridges where the overburden is at a maximum would tend to reduce the effects of deformation into the cavities. Construction on the ridges would also minimize surface hydrological effects. While not included in the analysis, these effects are known to accelerate the development of sinkholes and may play an important role in the formation of the surface depressions.

2.2 REGIONAL SINKHOLE OCCURRENCE

2.2.1 Additional Interpretation of Regional Subsidence Data

Newton and Tanner (1986) conducted a survey of sites in eastern Tennessee to characterize geologic settings susceptible to collapse. Further statistical analysis and evaluation of their data reveal some interesting observations. Most sinkhole occurrences occurred relatively recently (Fig. 2.1). This finding is tenuous, however, because it may be an indication of improved data availability as opposed to increased karst activity. In a

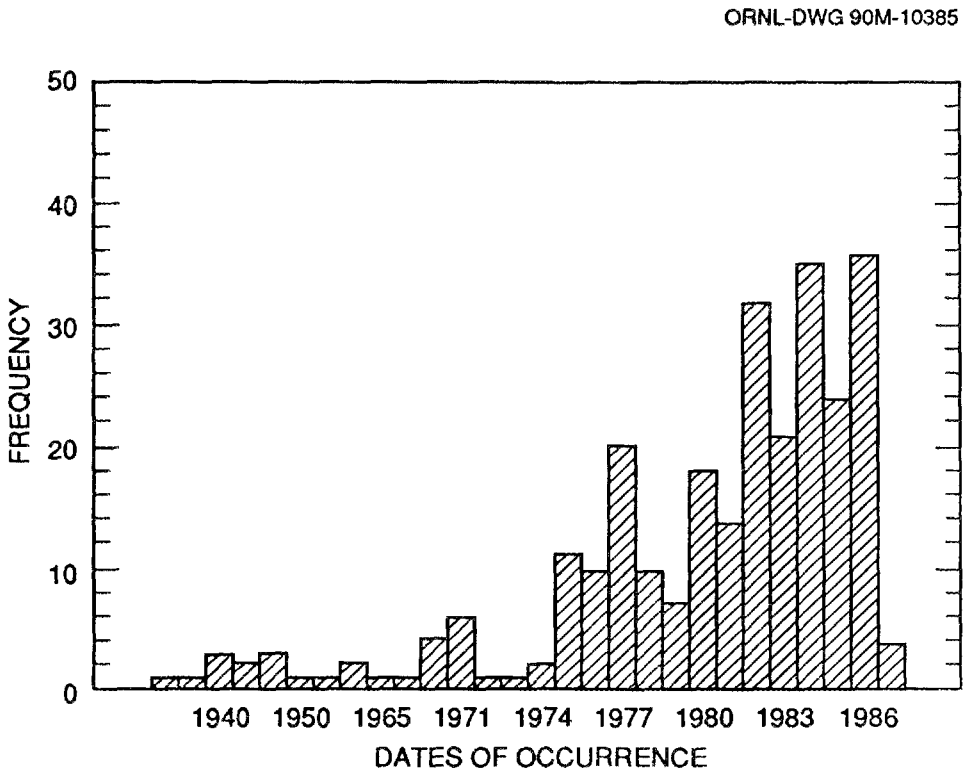

Fig. 2.1. Regional frequency histogram summarizing dates of sinkhole occurrences. (Data from Newton and Tanner 1986.)

summary of geometries, most dolines were relatively small and uniform in size. Of approximately 245 features measured, the majority were less than 9.1 m (30 ft) in diameter, with widths averaging 5.2 m (17 ft) and lengths averaging 5.9 m (19.5 ft). Figures 2.2 and 2.3 show that most eastern Tennessee sinkholes inventoried ranged between 0 m and 6.1 m (20 ft) in depth, averaging 4.6 m (15 ft) deep, while bedrock depth was relatively shallow, averaging 3.7 m (12 ft). The apparent disparity between the depth-of-sinkhole and depth-to-bedrock is because most of the Newton and Tanner (1986) data are composed of dropouts where the rock and karst pipe were visible at the bottom of the depression. Nevertheless, the data show that the soil arching that takes place increases the stability of the deeper karst pipes, as noted by Drumm et al. (1987).

The effect of water on sinkhole occurrence is a result of complicated interactions between rainfall, run-off, withdrawal, and permeability. However, a relationship between sinkhole occurrence and water table depth can be seen in Fig. 2.4. Sinkhole occurrences are correlated with shallow water tables, averaging 4.9 m (16 ft) deep. Whether this occurs because of a shallow water table or a rise and corresponding fall in groundwater level is unknown, but these latter fluctuations may easily be the causative factor. This latter hypothesis is supported by Fig. 2.5, which shows approximately twice the number of sinkholes are formed during periods of rainfall when groundwater levels are prone to fluctuate than when it was not raining. Linear regression also revealed that water table depth and sinkhole depth correlate with the square of the correlation coefficient (R^2) equal to 0.84, indicating a rather strong relationship between water table and sinkhole depths. Figure 2.6 shows that the top of bedrock correlates with the elevation of the water table.

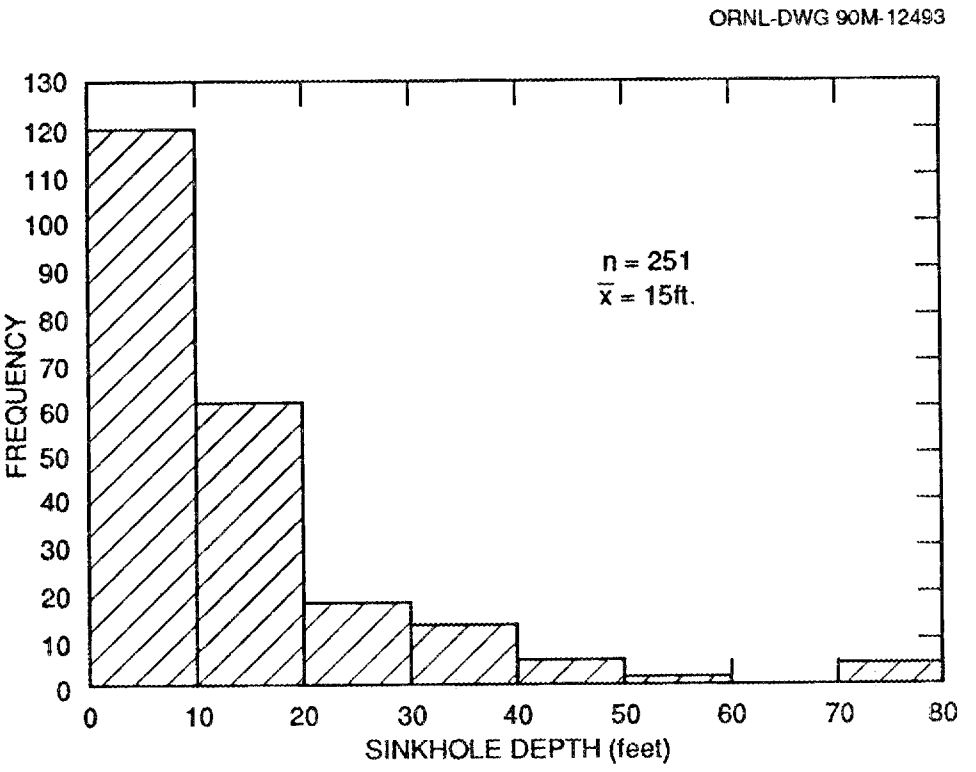

Fig. 2.2. Regional frequency histogram summarizing sinkhole depth. (Data from Newton and Tanner 1986.)

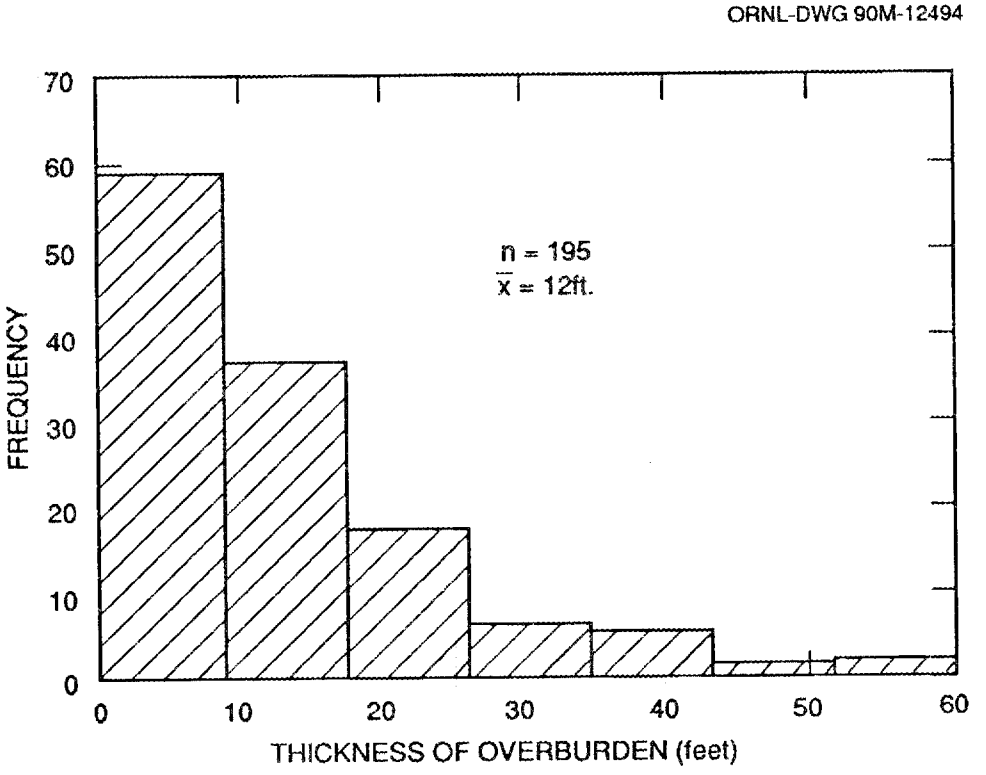

Fig. 2.3. Frequency histogram of regional overburden thickness. (Data from Newton and Tanner 1986.)

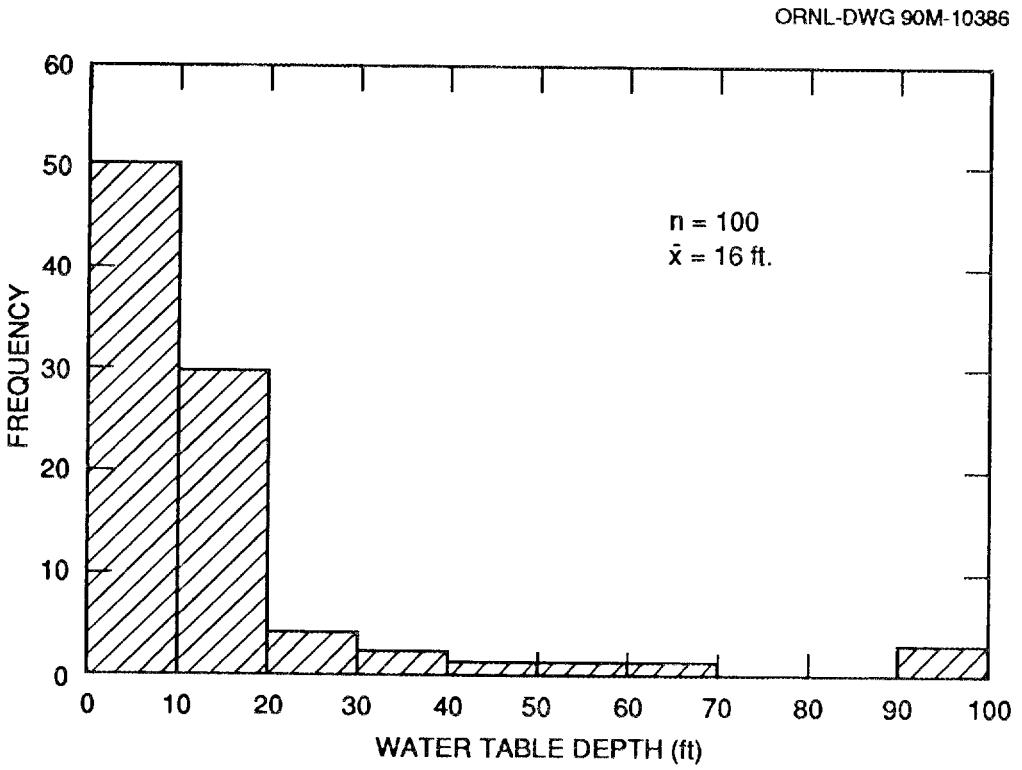

Fig. 2.4. Regional histogram of water table depths and sinkhole frequency. (Data from Newton and Tanner 1986.)

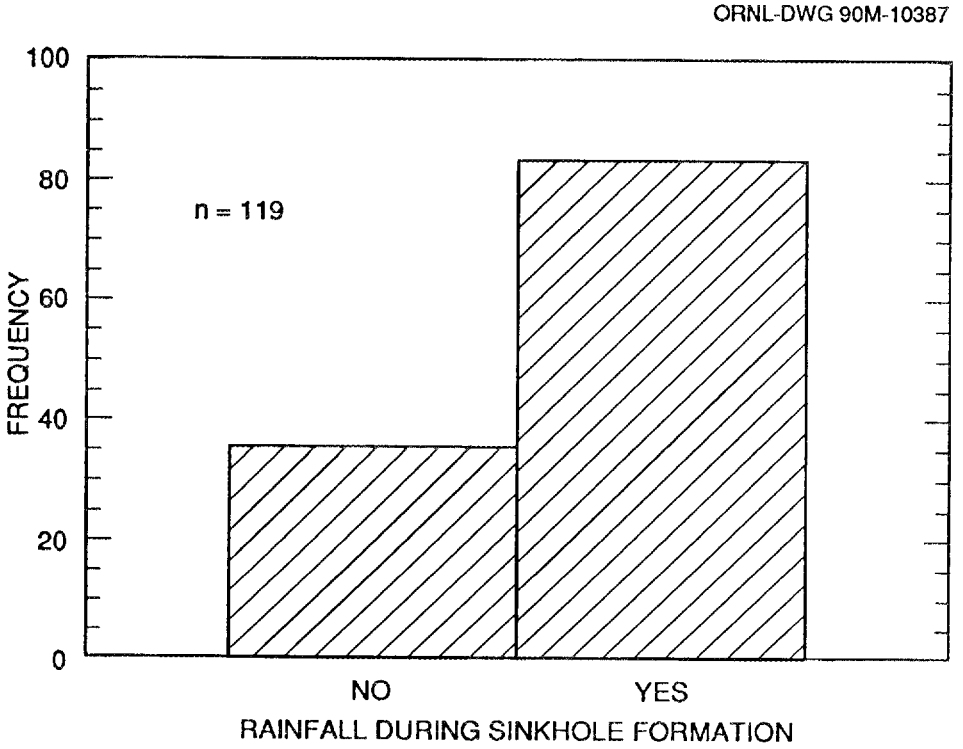

Fig. 2.5. The effect of rainfall on regional sinkhole occurrence. (Data from Newton and Tanner 1986.)

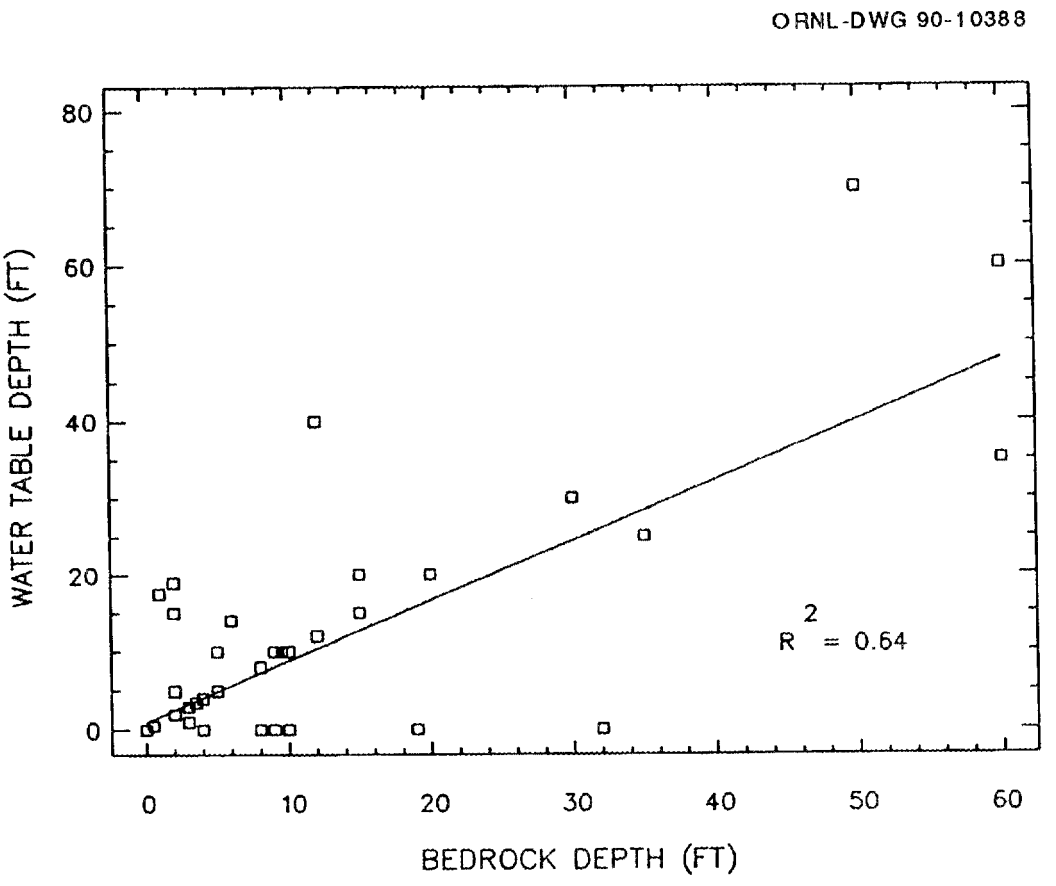

Fig. 2.6. Regional water table elevation with respect to bedrock. (Data from Newton and Tanner 1986.)

3. SITE CHARACTERISTICS

3.1 GEOLOGY

Chestnut Ridge is located on the DOE Oak Ridge Reservation, near the western edge of the Valley and Ridge Province. The ridge is underlain by silty clay soils and dolostone bedrock of the Knox Group. The topography is hilly with parallel ridges, valleys, and elongate knobs. Regional bedrock structure causes bedding at the site to dip at an attitude of 35° to 45° to the southeast. Variable weathering resistance and soil erodibility of the different stratigraphic zones have resulted in the parallel alignment of ridges and valleys. Effects of karst processes and erosion have combined in development of a rectangular surface drainage pattern. The karst system includes areas of doline karst on upland slopes, knobs, and ridge crests, with fluviokarst in the incised valleys. Soils include ancient alluvium, loess, colluvium, residuum and saprolite ranging in thickness from 2 m (6.6 ft) to more than 40 m (140 ft). Soils are predominantly residual silty clays with variable amounts of chert as boulders, nodules, and gravel. Because of their fine texture, site soils have a high moisture retention. High natural moisture content, variable chert content, and consolidation cause soils to range from very soft to very stiff.

Dolines occur in all five Knox Group stratigraphic formations, tending to align parallel to strike in some areas and along possible joint sets. Investigations at each of two sites (East Chestnut Ridge and West Chestnut Ridge) have included drilling, soil sampling, and testing within and outside visible karst features to obtain soil properties for use in subsidence analyses.

3.2 SOIL PROPERTIES

3.2.1 East Chestnut Ridge

Standard geotechnical site exploration was conducted on East Chestnut Ridge (Geologic Associates, Inc., 1989). Statistical analysis of the data revealed few significant trends in soil properties. Figure 3.1 displays the plasticity chart for the soils. The fact that the values plot almost entirely along the A-line indicates that relatively little difference exists between the soils, despite the fact that Fig. 3.2 indicates that there appear to be several major Unified Soil Classification System (USCS) soil types represented, predominantly clays of high (CH) and low (CL) plasticity and silts of high plasticity (MH).

The clustering of plasticity chart values indicates that the soils are actually very similar. It has been pointed out (Kulhawy et al. 1983) that moisture content values from standard Atterberg limits tests may vary as much as 20% because of laboratory procedures. When this is taken into consideration, there may be considerable homogeneity in the East Chestnut Ridge soils. This homogeneity is further indicated by plasticity index as a function of distance above the bedrock (Fig. 3.3). A high degree of scatter exists, which indicates that there are apparently no trends with respect to layering in the soil. However, a broad trend in increasing liquidity index with proximity to the bedrock is evident in Fig. 3.4. The soil is approaching the liquid state near the bedrock surface.

The overall conclusion that can be drawn from the statistical analysis of the East Chestnut Ridge soil data is that the soil is relatively uniform and homogeneous throughout and that an idealization of a homogenous soil, and not a stratified one, is justifiable. In addition, it is behaving more plastically in the vicinity of bedrock.

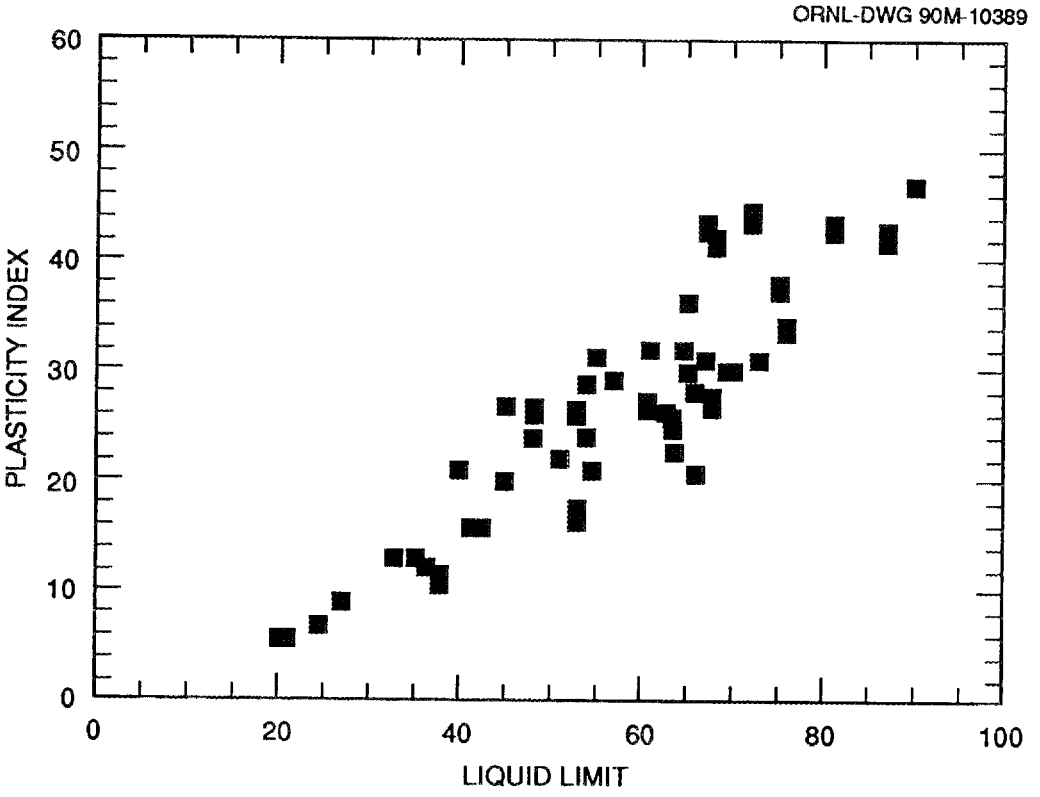

Fig. 3.1. Plasticity chart for East Chestnut Ridge soils.

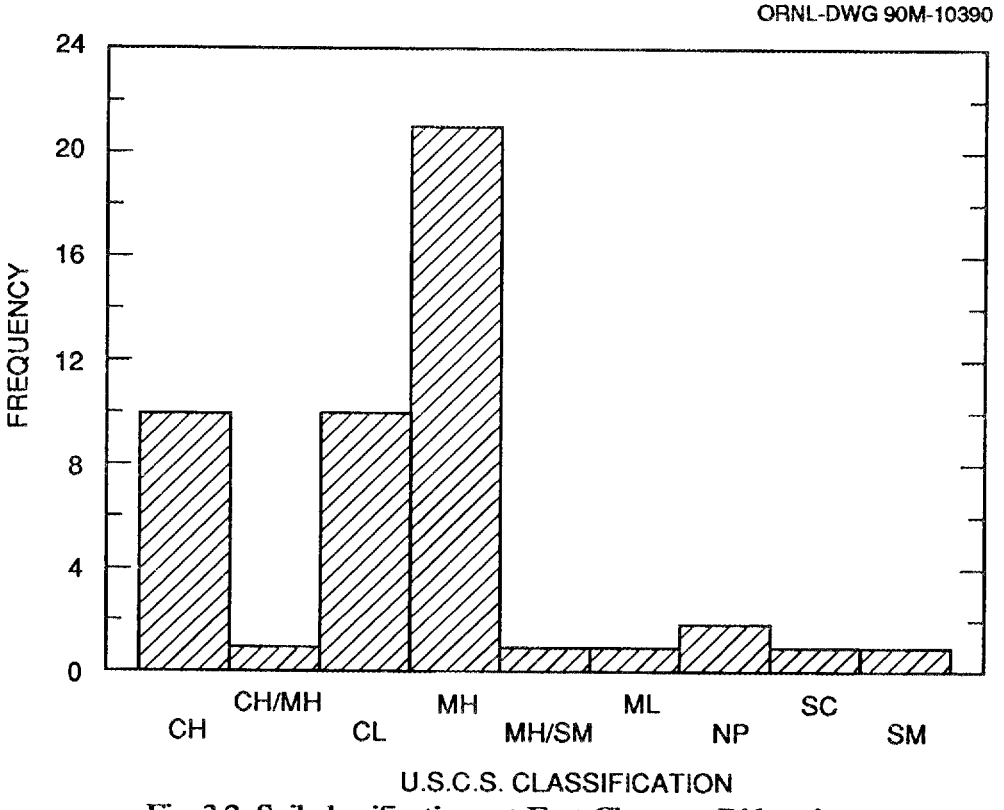

Fig. 3.2. Soil classifications at East Chestnut Ridge site.

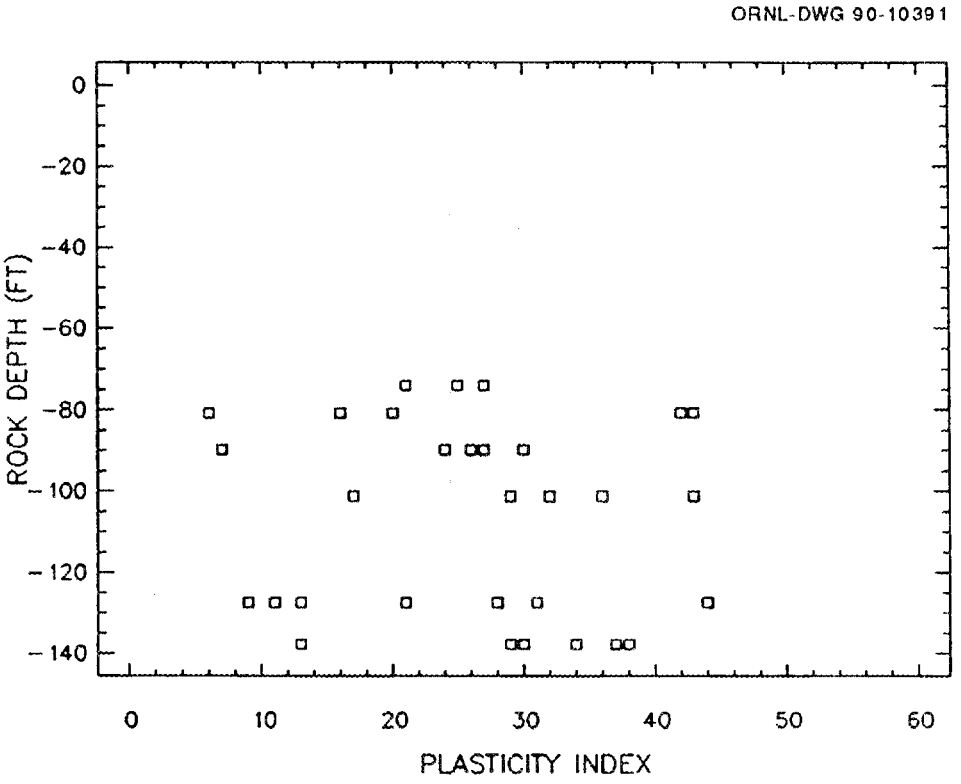

Fig. 3.3. Plasticity index as a function of depth for East Chestnut Ridge.

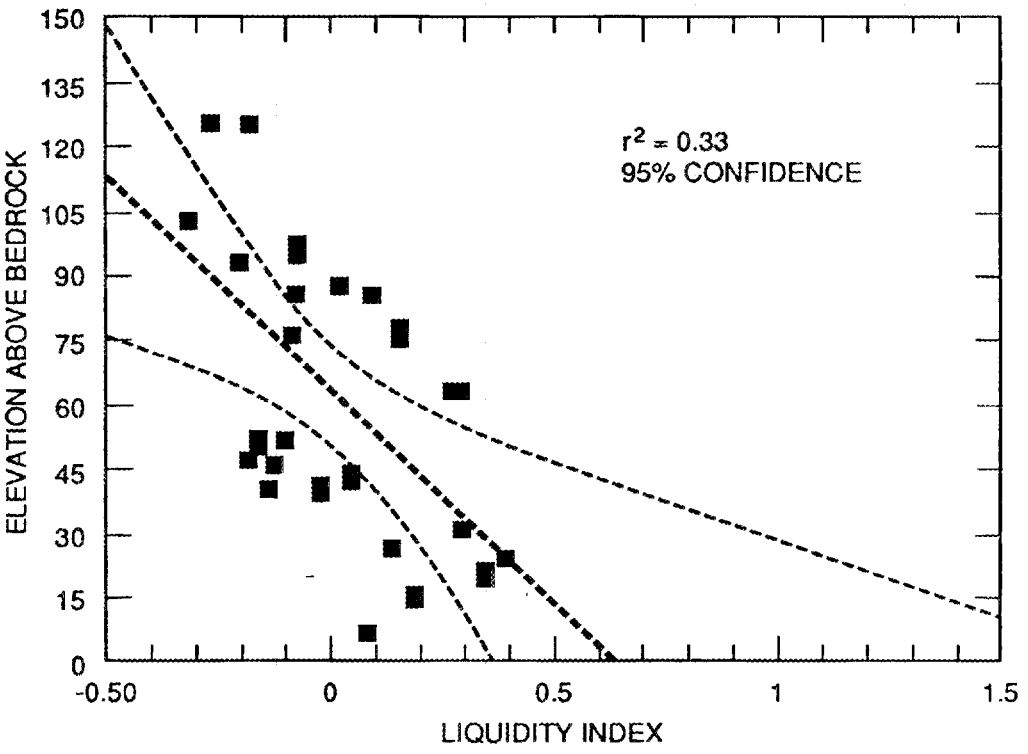

Fig. 3.4. Liquidity index as a function of depth for East Chestnut Ridge.

3.2.2 West Chestnut Ridge Site

Woodward-Clyde Consultants (1984) conducted an extensive survey of soil mechanics properties of West Chestnut Ridge. This site is along strike and practically identical geologically to the East Chestnut Ridge area in this investigation. A detailed summary is provided by Woodward-Clyde Consultants (1984) and Ketelle and Huff (1984), but some of the more pertinent details are reviewed here, as are some additional statistical data.

Figure 3.5 shows the plasticity chart for the West Chestnut Ridge soils. Once again, the values plot almost entirely along the A-line, which indicates that not only is there relatively little difference between the soils, but classifications and the plasticity chart (Fig. 3.6) reveal a similarity to East Chestnut Ridge soils.

A plot of plasticity index with distance above the bedrock for West Chestnut Ridge also indicates a high degree of scatter (Fig. 3.7). Once again, this could indicate that there are no layers of stratification in the soil. The liquidity index, as it did for East Chestnut Ridge, increases with proximity to bedrock, indicating that soils adjacent to rock surface are close to their liquid limit (Fig. 3.8).

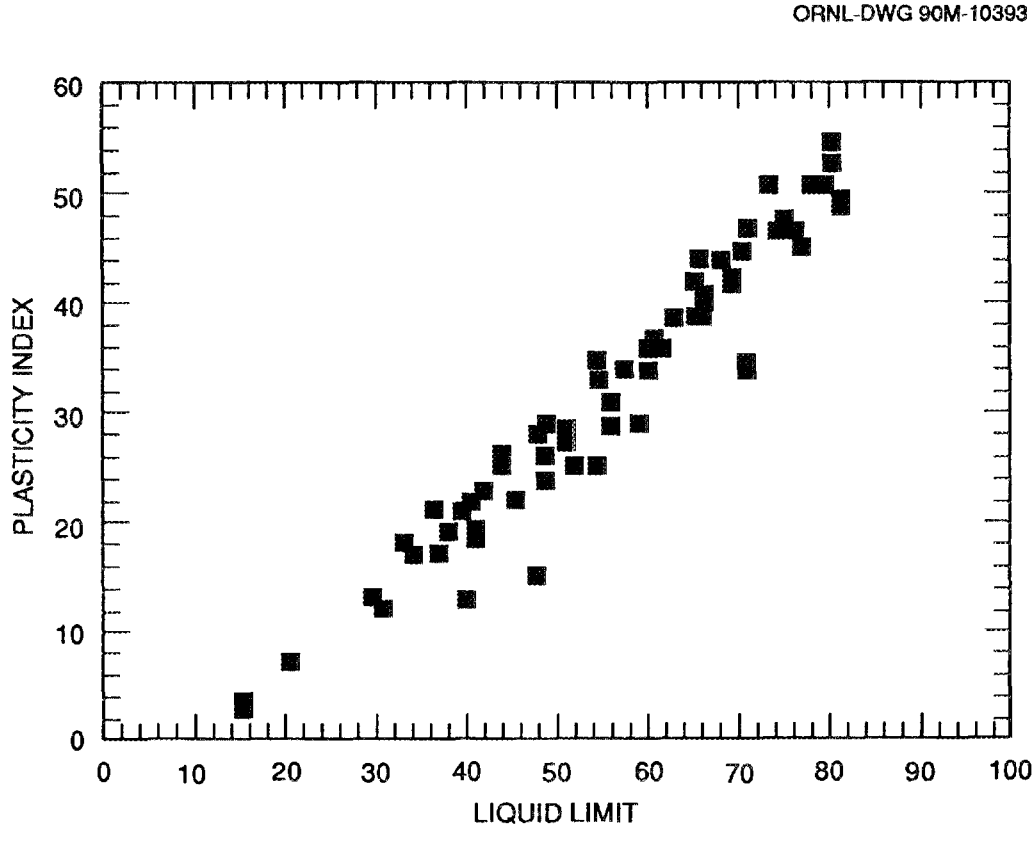

Fig. 3.5. Plasticity chart for West Chestnut Ridge soils.

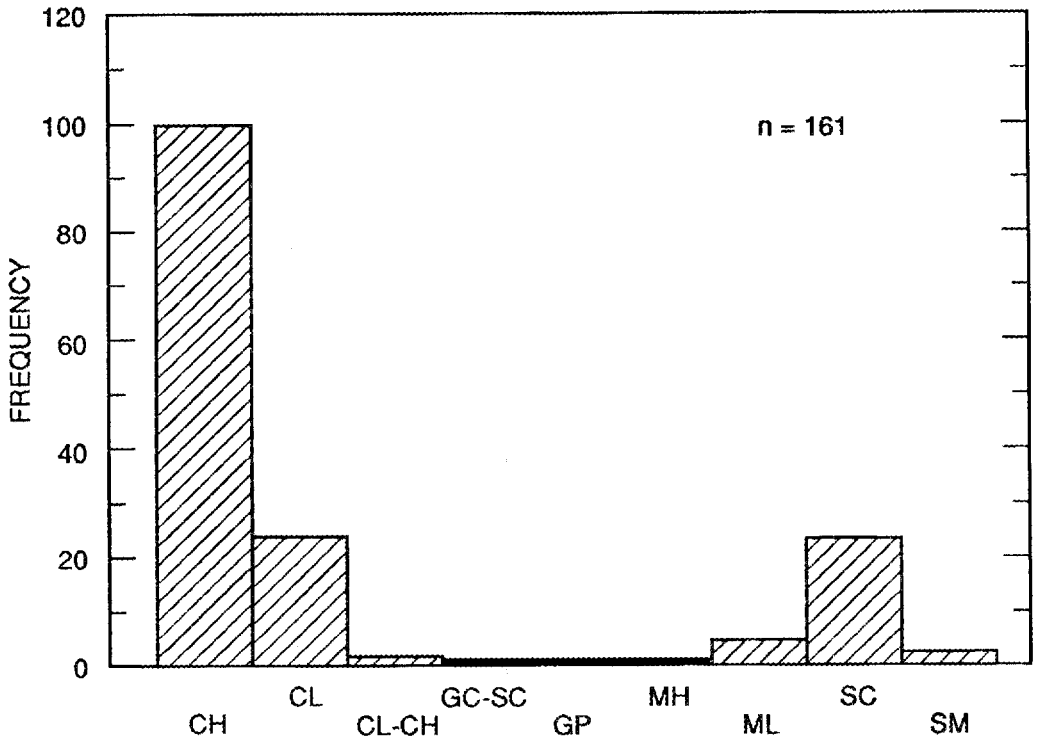

Fig. 3.6. Unified Soil Classification System (USCS) soil classifications for West Chestnut Ridge.

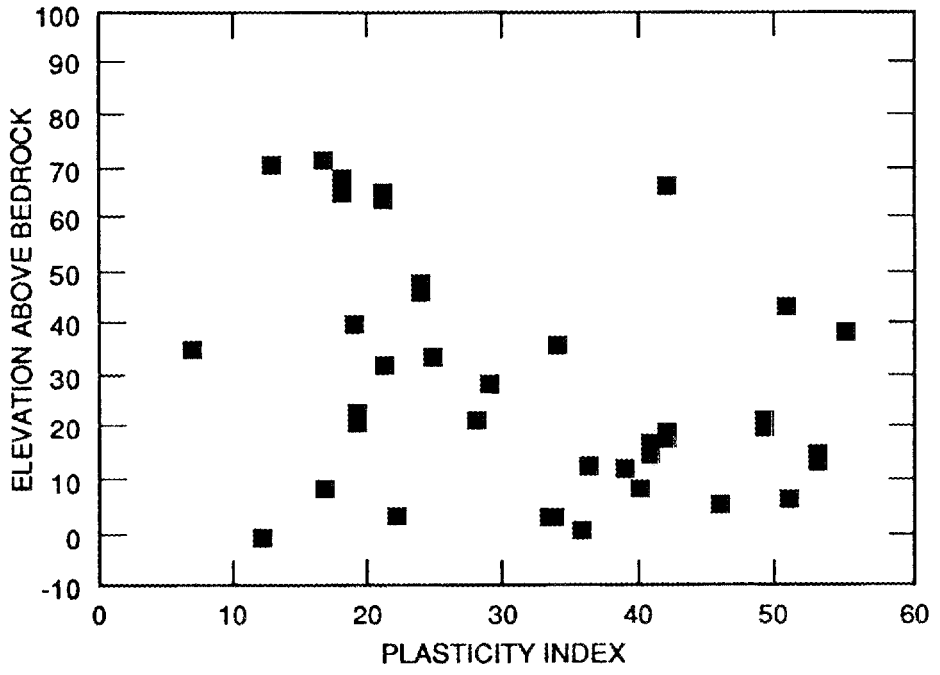

Fig. 3.7. Plasticity Index as a function of elevation above the bedrock surface for West Chestnut Ridge.

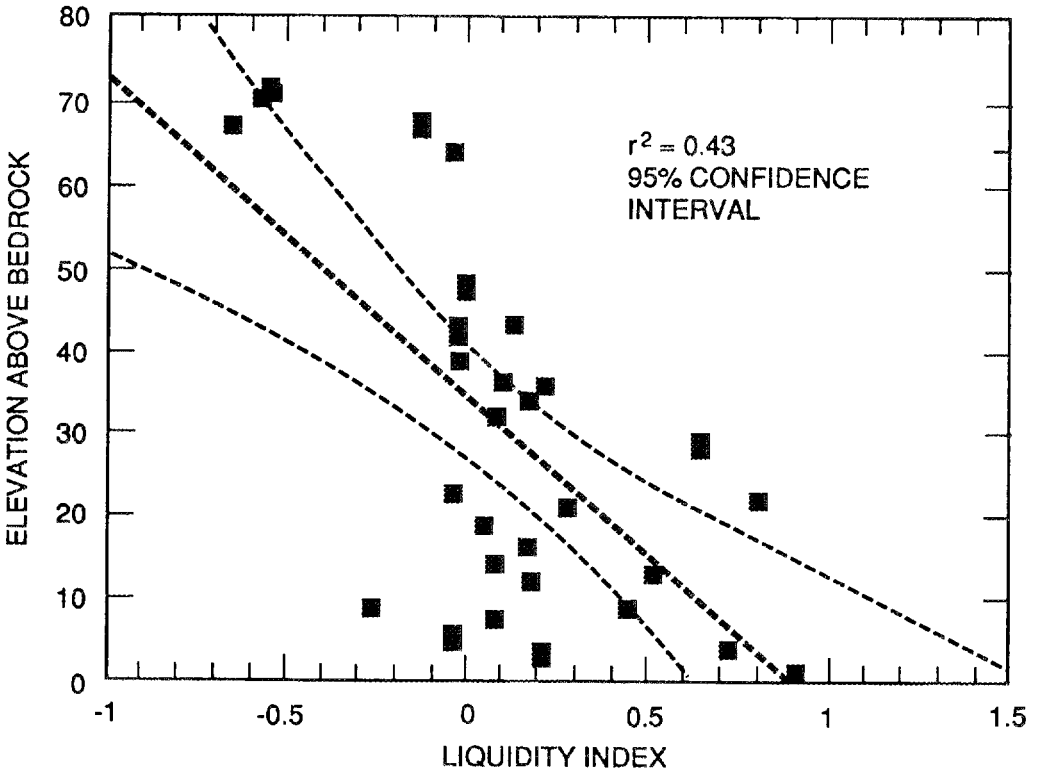

Fig. 3.8. Variation in liquidity index with proximity to bedrock for West Chestnut Ridge.

4. SINKHOLE MEASUREMENTS AND PROFILE FUNCTION ANALYSIS FOR THE EAST CHESTNUT RIDGE SITE

4.1 FIELD SINKHOLE MEASUREMENTS

4.1.1 Description of Survey Methods

Eleven karst features were measured to provide field data for profiling sinkhole shapes (Fig. 4.1). Differential leveling, a common technique of plane surveying, was used to determine the elevation of points within each feature. Differential, or direct, leveling is a method for determining an unknown elevation at a point relative to another point of known elevation within line of sight. For this research, surveying and mapping were done in the English system of measurement. Elevations were plotted, and contours were manually interpolated to produce 1:120 scale (1 in. = 10 ft), 1 ft contour interval topographic maps. Appendix A contains reductions of the original maps.

The equipment used in leveling was a dumpy level and a Philadelphia rod graduated in feet (tenths and hundredths of a foot). Horizontal distances were measured with a 150-ft add-type steel tape also graduated in feet (tenths and hundredths of a foot). A Brunton compass was used to measure the orientation of level lines. Angles can be measured to the nearest degree using a Brunton compass. No corrections to account for systematic errors in leveling, horizontal distances, or angular measurements were made to the field data.

A benchmark, the point of known elevation, was placed within or adjacent to a sinkhole. The benchmark was a 45-cm (17.5-in.) wooden stake driven into the ground to within 5 cm (2 in.) of its butt. The elevation of the benchmark was assumed known at 100 ft (30 m). Backsites were taken with the rod resting on the butt of the stake. Elevations in sinkholes 01, 02, 03, and 04 were taken relative to the same 100-ft datum adjacent to sinkhole 01. Sinkholes 08, 09, and 10 also share a common datum.

A baseline consisting of a row of wooden stakes equidistantly spaced at 10-ft (3-m) intervals was driven into the ground. The orientation of the baseline was measured relative to magnetic north. Elevations were measured at 10-ft intervals along a line normal to, and originating at, the baseline. The level line was laid out prior to measuring elevations. The tape was stretched along the level line and 10-ft intervals marked by kickout or with fluorescent marking tape. Intermediate spot elevations were typically made on slopes greater than 15% and in areas of rapid change in slope. The collected data resulted in a two-dimensional grid or net with known elevations at least every 10 ft (Fig. 4.2).

Linear interpolation between measured points of elevation in the grid allowed points of constant elevation to be determined. These points were connected to form a contour line. Smoothing to a curve was accomplished as the line was drawn. This process was repeated with contours representing integer foot elevations throughout the entire grid to produce the topographic map of the sinkhole.

More than 20 sinkhole-like features are located on the site. Eleven of these were selected for surveying. The criteria for selection were as follows: collapse, topographic closure, significant diameter, unmodified natural origin, and accessibility. Sinkholes were numbered in the order they were surveyed. Sinkholes 01 through 05 are adjacent and located on the northern ridge, and 06 and 07 are in the region between the northern and southern ridges. Sinkholes 08 through 11 are on the southern ridge.

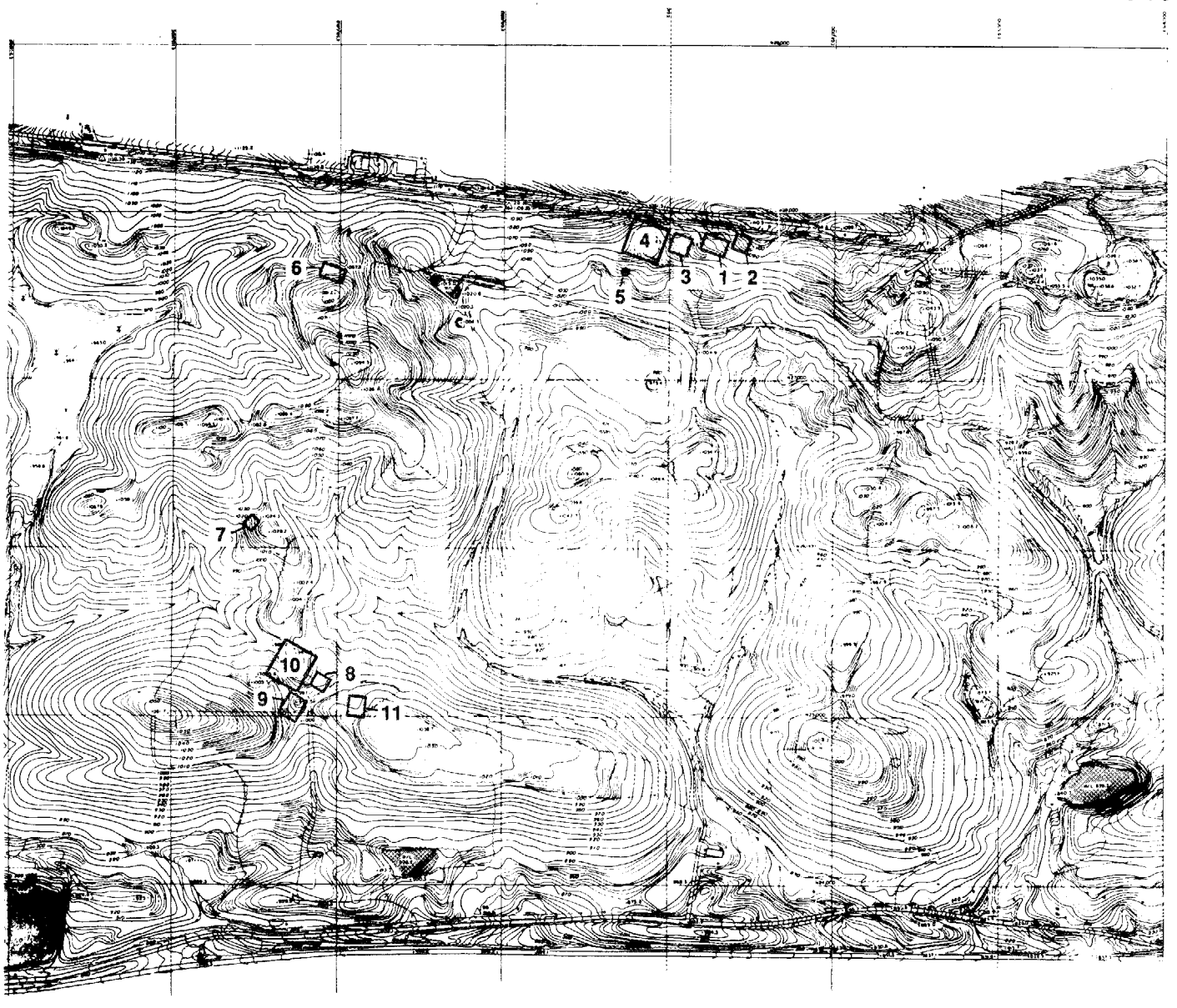

Fig. 4.1. Karst features used to determine profile functions.

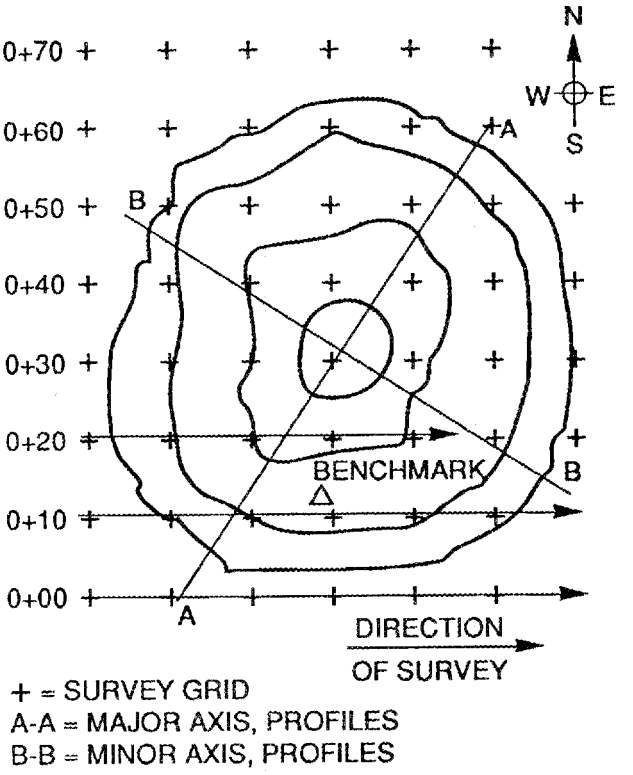

Fig. 4.2. Survey grid used in field mapping.

4.1.2 Results

Ten subsidence basins and one collapse feature were measured using conventional plane surveying techniques. The basins were generally circular and typically exhibited elongated or elliptical bottoms. Diameters ranged from 6 m (20 ft) to 87 m (285 ft). Measured vertical displacements ranged from 0.2 m (0.6 ft) to 5.5 m (18 ft). Slopes ranging from 5 to 10% and adjacent cut-and-fill complicated determination of the lateral extent of subsidence. Profiles were drawn from 1:120 scale, 0.3-m (1-ft) contour maps using two criteria: (1) the profiles were oriented along and perpendicular to the major (or long) axis, and (2) the profiles were orthogonal to contour lines. The location of the field profiles are provided in Appendix A.

4.2 PROFILE FUNCTIONS

4.2.1 General Description of Profile Functions

In establishing whether or not damage to a surface structure (such as a landfill and liner) might occur, it is necessary to predict the amount of differential settlement that may occur. To estimate the differential settlements in the study area, an investigation of methods used in mining engineering was performed.

Empirical methods have long been used in subsidence prediction above longwall coal mines. One method of empirical subsidence prediction, which may have application in karst terrain, is the use of *profile functions.* Originally developed in Europe, profile functions predict the shape of the induced subsidence basin by assuming that similar conditions, geometry, and material properties will induce a similar response at the surface. Application of this method involves fitting a mathematical function to a significant number of actual subsidence basin profiles. The curve fit determines constants that predict and describe the shape of a subsidence basin. The lateral and vertical extent of the surface deformation is determined by subsurface geometry and described below.

Table 4.1 is a listing of several profile functions that have found application in subsidence prediction. Two functions have found application in the Appalachian coalfields of the United States: (1) the hyperbolic tangent function, and (2) the negative exponential function.

The hyperbolic tangent function, suggested by Brauner (1973), is symmetric about the profile inflection point, which occurs at one-half the maximum subsidence. The function is as follows:

$$S(x) = \frac{1}{2} S_o \left[1 - \tanh\left(\frac{CX}{B}\right)\right] , \qquad (4.1)$$

where $S(x)$ = vertical displacement, S_0 = maximum vertical displacement, X = horizontal distance from the origin, B = horizontal distance from the centerline to the point of inflection, and C = an empirical parameter.

Figure 4.3 is a generic subsidence profile identifying the terms that define the hyperbolic tangent function. The origin is located at the inflection point. Positive values are upward and to the right. The centerline of the profile is located at the point of maximum vertical displacement.

The negative exponential function suggested by Chen and Peng (1981) differs from the hyperbolic tangent function in that it is not symmetric about its inflection point. The negative exponential function is expressed as:

$$S(x) = S_o \, e^{-\alpha\left(\frac{X}{L}\right)^{\beta}} , \qquad (4.2)$$

where L = half-width of the subsidence basin, and α and β are empirical parameters.

Figure 4.4 defines the terms of the negative exponential function. The origin is located on the centerline of the basin at the point of maximum vertical displacement. The half-width of the basin is taken as the horizontal distance from the origin to a point on the curve at 5% of the maximum vertical displacement.

It is common practice, with both functions, to normalize vertical displacement by its maximum value. In addition, horizontal distances are often normalized by the distance(s) to the origin. The slope at any point on the curve is the first derivative of the profile function, and the curvature is the second derivative.

Application of profile functions for subsidence prediction requires knowledge of the subsurface geometry. The extent and magnitude of surface displacements are related to the size of the extracted area and the width-to-depth ratio, a ratio of the size of the void to the

Table 4.1. Profile functions (Chen and Peng, 1981)

$$\frac{S(x)}{S_0} = \left[1 - Z + \frac{1}{2\pi}\sin(2\pi Z)\right] \qquad \textit{Kolbenkov (Russian)}$$

$$\frac{S(x)}{S_0} = (1 - Z)^{4.54}\, e^{4.54Z} \qquad \textit{Avershin (Russian)}$$

$$\frac{S(x)}{S_0} = e^{\frac{-x^2}{2B}} \qquad \textit{Moto (Hungarian)}$$

$$\frac{S(x)}{S_0} = -1\int_x^{\infty} e^{\frac{-\pi x^2}{r^2}}\, dx \qquad \textit{Knothes (Polish)}$$

$$\frac{S(x)}{S_0} = \frac{1}{2}\left[1 - \tanh\frac{6x}{H}\right] \qquad \textit{Wardell (British)}$$

$$\frac{S(x)}{S_0} = \frac{1}{2}\left[1 - \tanh\frac{2x}{H\cot B}\right] \qquad \textit{King and Whetton (British)},$$

$$\textit{where } Z = \frac{X}{L}, \textit{ and } r = H\cot B$$

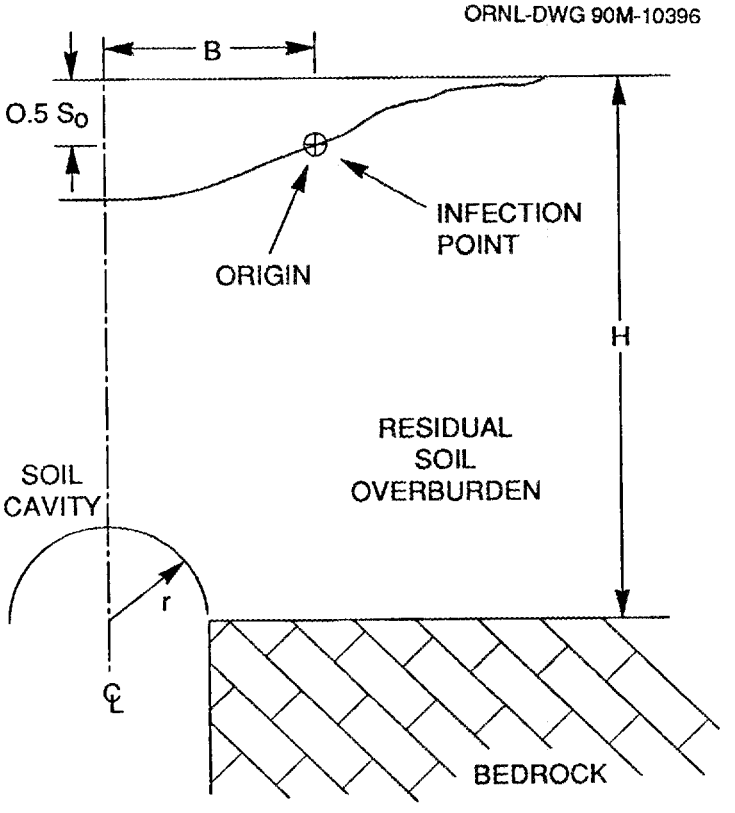

Fig. 4.3. Generic hyperbolic tangent profile and definitions of terms.

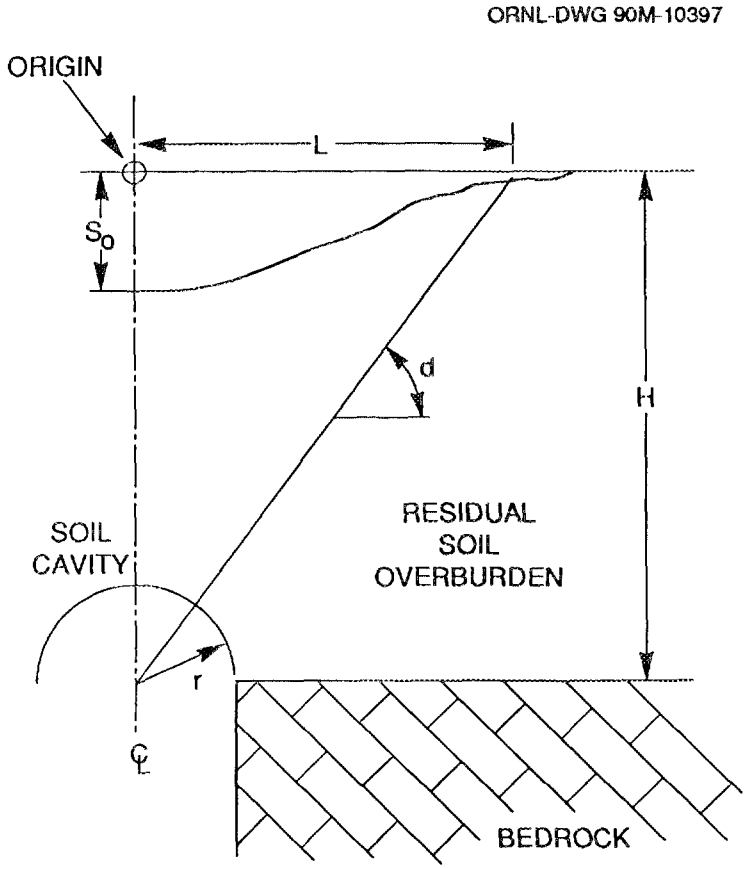

Fig. 4.4. Generic negative exponential profile and definition of terms.

depth to the void. The subsurface geometry of some mines often allows a width-to-depth ratio greater than one. Width-to-depth ratio has been identified as a critical parameter in defining maximum possible subsidence.

Subsidence profiles above a longwall panel are usually described as having the characteristic shapes of subcritical, critical, or supercritical (Peng and Chaing 1984). If the value of maximum subsidence for the basin occurs at a single point, usually at the center, the profile is subcritical. Critical profiles are similar in shape to subcritical profiles, but additionally the magnitude of subsidence has reached its maximum possible value. If the basin has a flat bottom, having uniformly reached this maximum displacement, the profile is described as supercritical.

Profile functions do not require a knowledge of the material mechanical behavior; the overburden material is assumed to be homogenous. To account for the inhomogeneity of actual subsurface materials, Karmis et al. (1987) apply a reduction factor to the estimated maximum subsidence based on the percentage of competent strata above the void.

Chen and Peng (1981) define four angle parameters: limit angle, angle of critical deformation, angle of break, and angle of complete mining; they are defined as follows:

1. The *limit angle* is the angle from the horizontal to the line connecting the edge of the subsurface void to the point of zero subsidence at the surface. This angle is used to calculate the radius of influence or the half-width of the profile.

2. The *angle of critical deformation* is the angle from the horizontal to a line connecting the edge of the subsurface void to the surface at the point to which certain structures will be subjected to damage.
3. The *angle of break* is the angle between the horizontal and a line connecting the edge of the subsurface void to the point on the surface where the first tension crack occurs.
4. The *angle of complete mining* is the angle between the horizontal to a line connecting the edge of the subsurface void to the outermost point of maximum subsidence at the surface.

Karmis et al. (1987) define two additional angle parameters:

1. The *angle of draw* is the angle between the vertical and a line connecting the edge of the subsurface void to the point of zero vertical displacement on the surface.
2. The *angle of influence* is the angle between the horizontal and a line connecting the edge of the subsurface void to the point on the surface where $S(x) = 0.0061\ S_0$.

The various angle parameters define the lateral extent of subsidence and relate it to the depth of overburden above the subsurface void.

4.2.2 Profile Function Parameters for the East Chestnut Ridge Site

Profiles were drawn using two criteria: (1) profiles were oriented along and perpendicular to the long, or major, axis of the sinkhole, and (2) profiles were orthogonal to contour lines. Figure 4.5 illustrates the application of these criteria. Rotation of the profile to eliminate the effect of adjacent slopes on the profiles was also performed. The maps in Appendix A show the location and orientation of the selected profiles for each sinkhole.

Figure 4.6 shows normalized field data from sixteen profiles and the associated best fit curve for the negative exponential function. The value of the empirical parameters, $\alpha = 2.50$ and $\beta = 3.30$, were determined using least squares estimates from nonlinear regression analysis (STSC 1988). Figure 4.7 displays the best fit for the hyperbolic tangent function to the field data. The empirical parameter, C, is equal to 2.63.

4.3 SUMMARY OF PROFILE FUNCTION STUDY

Profile functions provide a means to determine the general shape of typical dolines in the site area. By inputting the maximum subsidence possible for a given location and an estimate of width, the profile function can be used to predict the shape of a sinkhole depression. The derivatives of the profile function can provide the slope and curvature of the ground surface. Vertical displacement, slope, and curvature are associated with structural damage.

The difficulty in applying profile functions to karst situations is that, unlike mining, the maximum subsidence cannot be determined. In coal mining the maximum possible subsidence for a region is a function of the seam thickness. With no extracted seam present, it is necessary to develop an alternative means of maximum subsidence prediction, which can be done using numerical modeling techniques such as the finite element method.

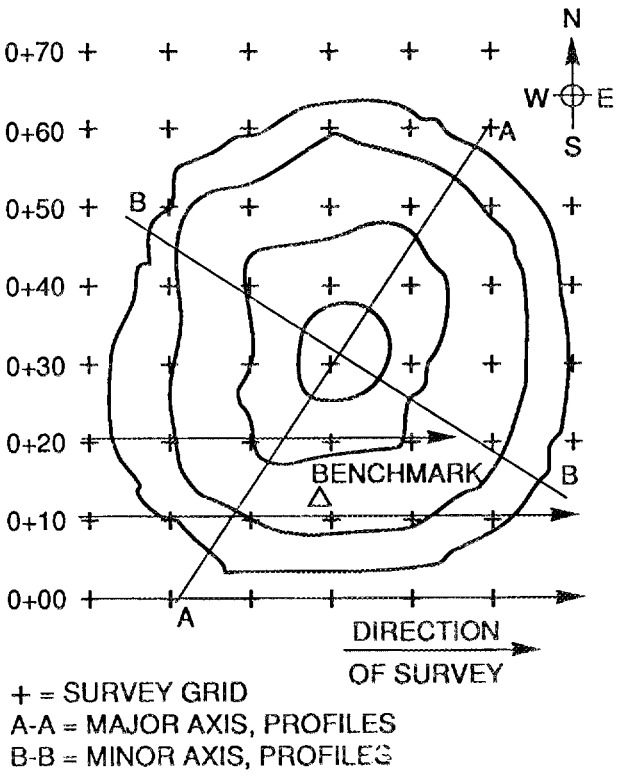

Fig. 4.5. Idealized orientation of profiles, plan view.

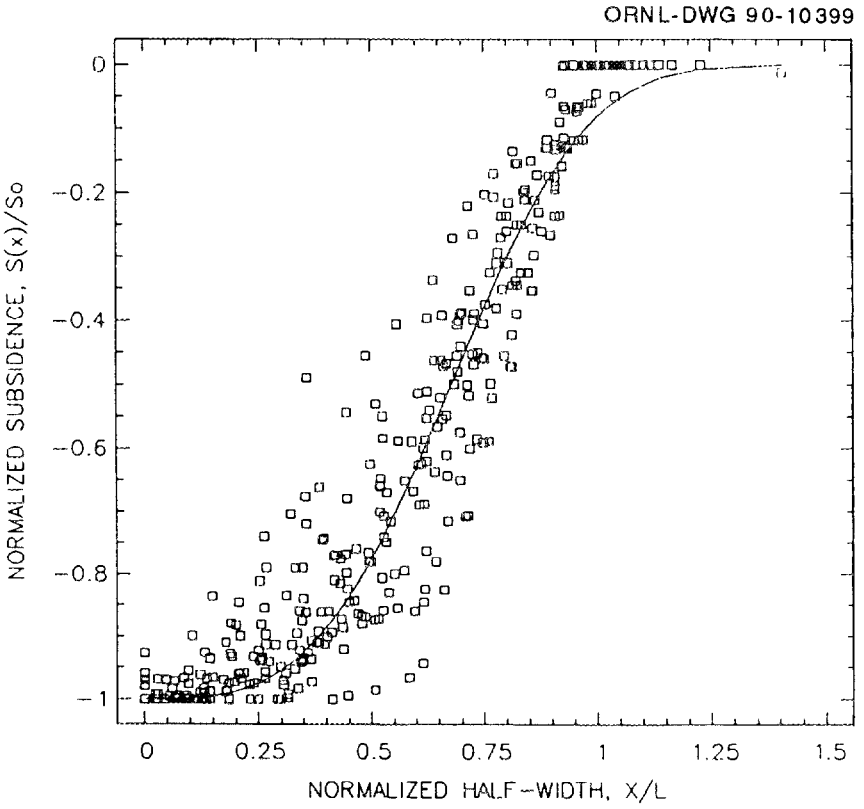

Fig. 4.6. Typical profile and best fit of the negative exponential function.

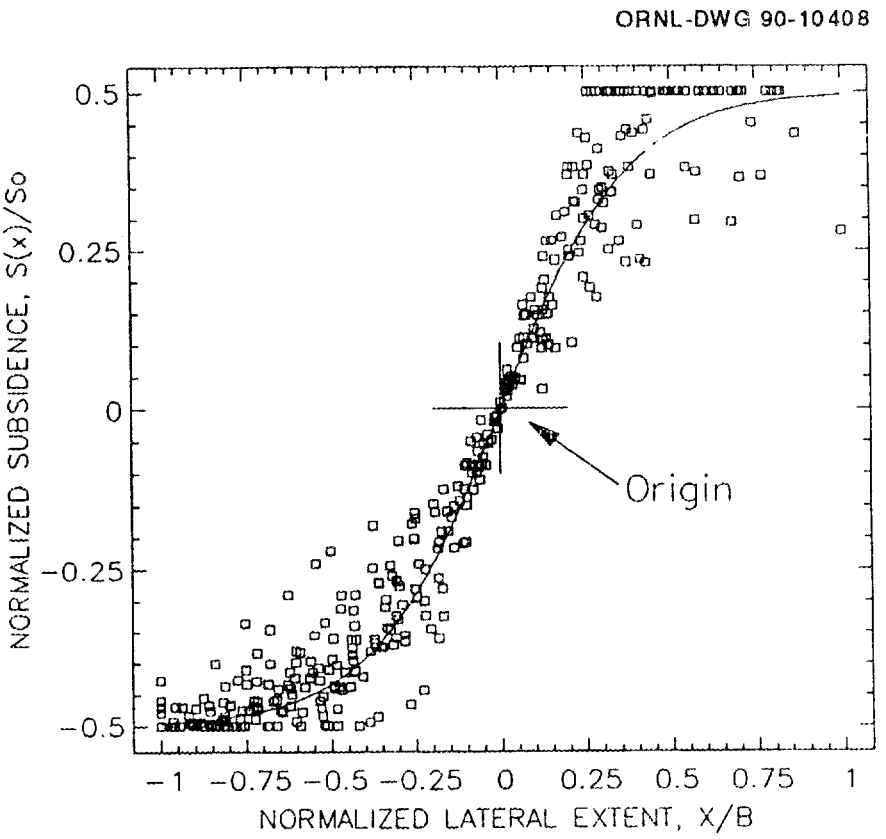

Fig. 4.7. Best fit of hyperbolic tangent function to actual field data.

5. NUMERICAL ANALYSIS OF STABILITY

5.1 ANALYTICAL APPROACH

The deformations, strains, and stresses in the soil adjacent to the bedrock cavity was calculated by the finite element (FE) method. The FE code UTGTECH (Ben-Hassine 1988) was used for the analysis. This code incorporates many features of the code SSTIN (Desai and Lightner 1985) used in the previous West Chestnut Ridge study (Drumm 1987), including the use of eight node isoparametric quadrilateral elements and several material behavior models. However, UTGTECH was restructured to allow for the efficient solution of various size problems on personal computers, to improve the convergence of the solution of elastic-plastic problems, and to provide post-processing graphics capability. These aspects will be described in more detail in subsequent sections of this report.

5.1.1 Background and Idealization of a Soil Void

In a typical numerical evaluation of stress-deformational response of a soil mass because of imposed structural loadings, the stresses from the in situ or gravitational forces are first determined. Frequently, these in situ stresses are assumed to be elastic. After determination of the in situ stresses, the deformations resulting from these body forces were set to a zero value such that the final deformations from the imposed structural loadings are calculated relative to the gravitational deformations. In this analysis, elastic and plastic deformations caused by in situ loadings are of interest. Consequently, the gravitational forces have been applied incrementally and the deformational response to gravity observed.

Because groundwater seepage tends to be drawn along the bedrock surface, washing of the residual soils tends to form elongated soil voids that are likely to be larger than discontinuities in the bedrock (Kemmerly 1980). Piping and collapse of the residual soil above the bedrock cavity often result in the formation, upward propagation, and eventual collapse of the soil void (Ogden 1984; Beck 1984). The evolution of a sinkhole is schematically depicted in Fig. 5.1 (Drumm et al. 1990). The state of stress and the resulting shear strength of the surrounding soil govern the stability of the sinkhole. In the numerical analysis described here, the soil void is assumed to be circular in cross section, in the stability investigated for a range of soil void radii, r_v, and in overburden thicknesses, H.

5.1.2 Analytical Assumptions

The soil above the bedrock solution cavity is assumed to have eroded because of fluctuations in the groundwater table, causing a void in the soil. A further assumption is that the void is circular in cross section and that plane strain conditions exist. These conditions are different from those of the previous investigation (Drumm 1987), which assumed that the soil was continuous over bedrock cavities of varying diameters and an axisymmetric idealization was most appropriate.

The following assumptions have been employed in the analysis:

1. The bedrock solution cavity is taken as a horizontal, linear feature following jointing in the rock, and the length of the feature is large with respect to the thickness of the residual soil overburden. The load applied to the system is caused by the gravitational forces acting on the overburden soil. This load is uniform

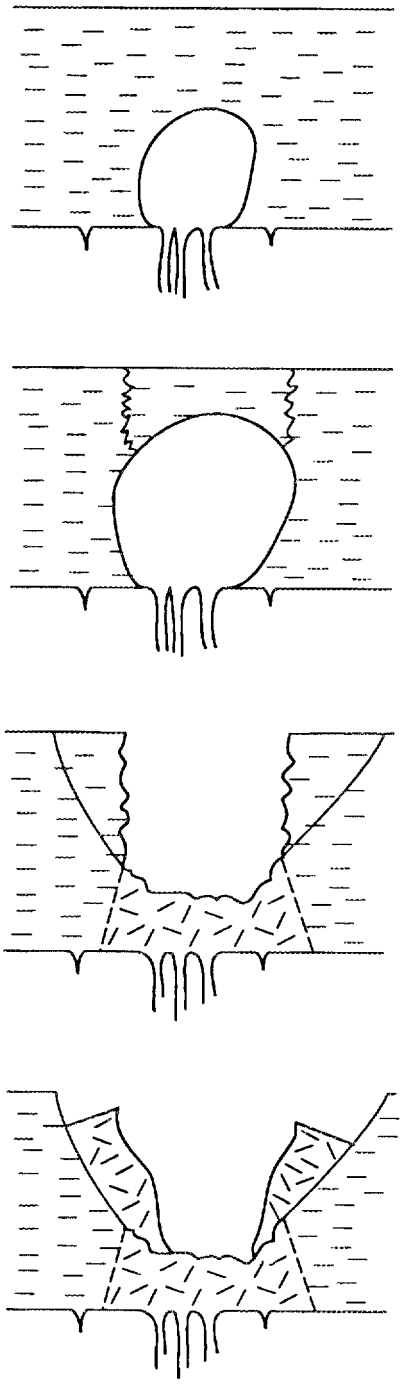

(a) Intitial stage. Void formation near dominant fracture inlet.

(b) Critical stage. Shear zone develops between the void and the surface.

(c) Sinkhole collapse. Collapse in which the soil plug falls, masking the bedrock inlets.

(d) Slope instability. Slip surfaces form in slope surrounding sinkhole.

Fig. 5.1. Evolution of a sinkhole (after Drumm et al. 1989).

across the soil section, based on the assumption of a horizontal ground surface, but varies with depth. Effects from the interaction between adjacent solution cavities are neglected. These assumptions permit the three-dimensional problem to be modeled using a two-dimensional plane strain idealization and require that only one half of the soil/void system be investigated since the problem is symmetrical about the centerline. A typical finite element idealization employed in the analysis is shown in Fig. 5.2.

2. The dolostone bedrock can be represented by rigid vertical supports under the residual soil. The assumption implies that the bedrock containing the cavity is strong and stiff with respect to the adjacent soil. The soil is free to move horizontally along the bedrock contact, consistent with the assumption of low frictional resistance between the plastic soil and bedrock.

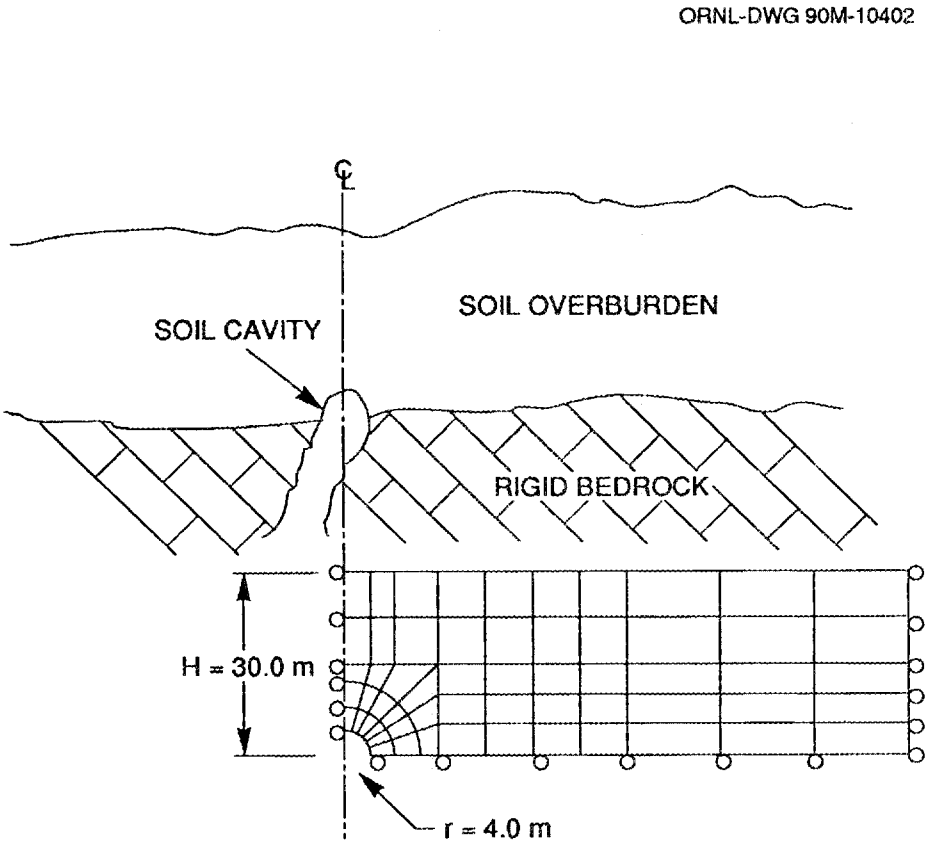

Fig. 5.2. Typical finite element (FE) idealization of residual soil/bedrock cavity system.

3. The stress-deformational response of the residual soil can be represented by an incremental elastic-plastic constitutive model. The strains are assumed to be composed of elastic and plastic components. Elastic strains are determined from elastic theory, while plastic strains are determined from a stress-hardening plasticity model.
4. The applied loads caused by soil overburden are applied over a period of time. The resulting long-term stability analysis permits the expression of the soil properties in terms of effective stress properties, obtained from consolidated, drained triaxial tests and consolidated, undrained triaxial tests with pore pressure measurements.
5. The water table is below the bedrock surface and remains constant throughout the analysis. A rising or falling water table can be expected to change the properties of the soil, as well as the imposed loadings. Seepage forces and soil transport/erosion effects are beyond the scope of the current investigation.

A typical finite element idealization of the residual soil/bedrock cavity system is illustrated in Fig. 5.3. The details and implementation of these basic assumptions are described in the following sections.

5.2 CONSTITUTIVE MODEL AND CHARACTERIZATION OF MATERIAL RESPONSE

The choice of an appropriate material constitutive model is one of the most important aspects of numerical analyses. The accuracy of the computed displacements, stresses, and strains is directly related to the ability of the constitutive model to represent actual material behavior. However, a balance must be achieved between the sophistication of the model and the complexity of the laboratory tests required to determine the material parameters. The more advanced constitutive models also may significantly increase the computational time.

5.2.1 Linear Elastic Model

The stress-strain behavior of soils is dependent on several factors such as density, moisture content, soil structure, drainage conditions, loading conditions, duration of loading, stress history, confining pressure, and shear stress. To minimize the effects of these factors, selection of materials and simulation of field conditions during testing become important.

A linear elastic model, in which stress is a linear function of strain, is often used in modeling the behavior of soils undergoing deformation. The linear elastic model assumes that during loading and unloading stress is directly proportional to strain. The constant of proportionality is Young's modulus, E. Additionally, Poisson's ratio, μ, relates the horizontal strains of the material to the vertical strains.

Although this behavior is generally true for metal and concrete below the elastic limit, soils exhibit a nonlinear, inelastic behavior that cannot be described by the linear elastic model. The result is a gross overprediction of soil stress and the inability to model the redistribution of stresses within the soil mass as the soil yields without failing.

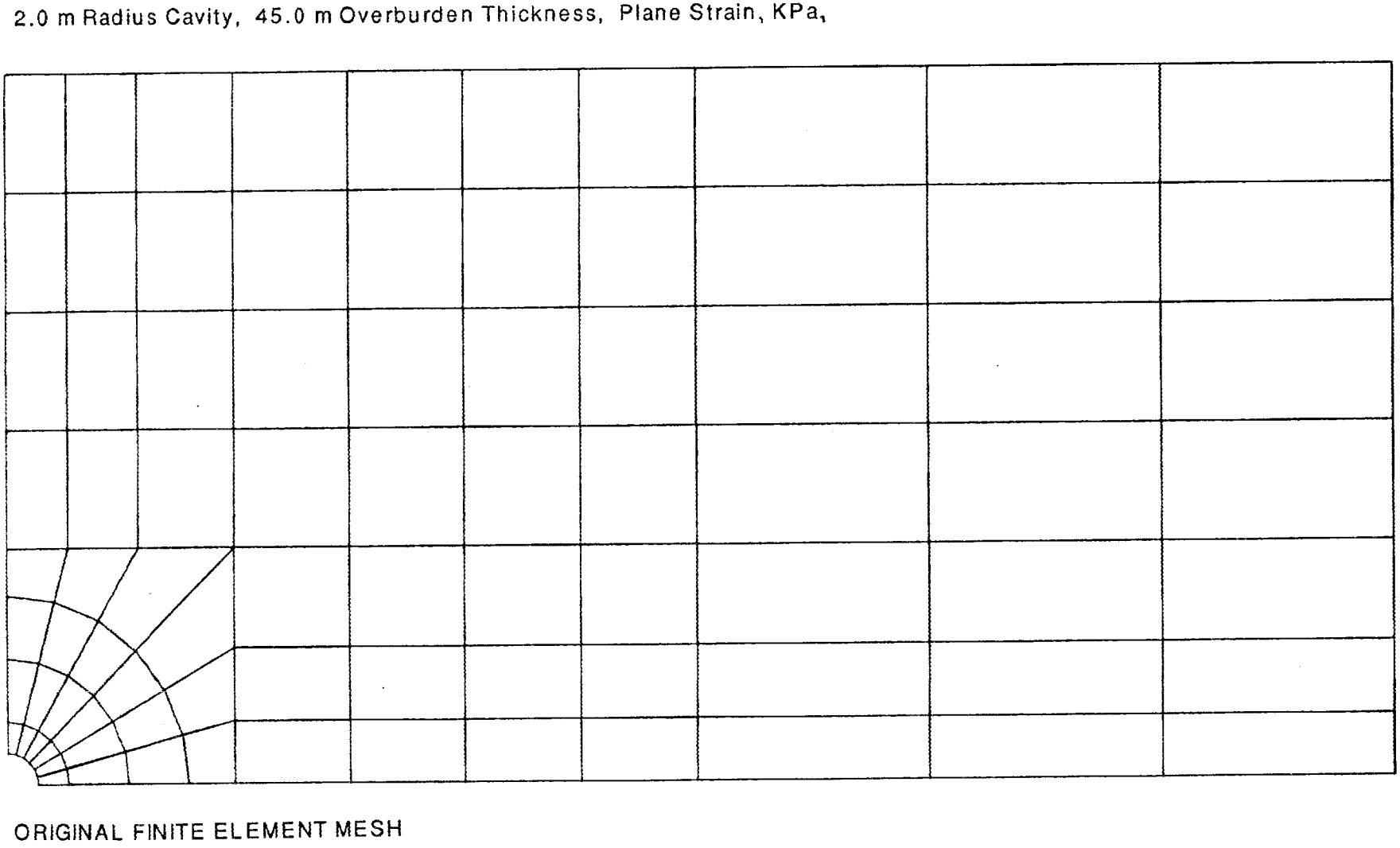

Fig. 5.3. Idealized representation used in finite element (FE) analysis.

A linear elastic analysis is not appropriate for this problem for three major reasons. First, the observed relationship between stress and strain in the soil is highly nonlinear. Second, a linear elastic characterization assumes that each soil element has an infinite strength in both compression and tension and does not allow for the yield of the highly stressed soil elements. Third, the elastic representation cannot provide for the stress path-dependent response exhibited by most soils.

Although some early analyses of the East Chestnut Ridge site were conducted using a linear elastic model to verify the finite element idealization, the results are not reported. Only results from the more realistic hyperbolic elastic and elastic-plastic cap models are included.

5.2.2 Hyperbolic Elastic Model

The hyperbolic elastic model reduces actual nonlinear behavior to a practical stress-strain relationship. The final form of the hyperbolic model used in this investigation was developed by Duncan and Chang (1970) based on previous work by Kondner (1963) and Janbu (1963). The hyperbolic model describes principal stress difference as a nonlinear function of strain. This model represents the observed frictional stress-strain response of the soil and limits the stress in the soil mass. The resulting hyperbolic model is as follows:

$$(\sigma_1 - \sigma_3) = \frac{\epsilon}{\frac{1}{E_i} + \frac{\epsilon R_f}{(\sigma_1 - \sigma_3)_f}} , \qquad (5.1)$$

where σ_1-σ_3 = principal stress difference; ϵ = axial strain; E_i = the initial modulus,

$$E_i = KP_a \left(\frac{\sigma_3^n}{P_a} \right) ,$$

where K = dimensionless stiffness number, n = stiffness exponent; σ_3 = minor principal stress and P_a = atmospheric pressure; and $(\sigma_1$-$\sigma_3)_f$ the principal stress difference at failure,

$$(\sigma_1 - \sigma_3)_f = \frac{2\sigma_3 \cdot \sin\phi + 2c \cdot \cos\phi}{1 - \sin\phi} ,$$

where ϕ = soil angle of friction and c = cohesion of soil, and R_f = failure ratio, defined as the ratio of the failure stress to the ultimate stress.

The modeling procedure involves determining a hyperbolic form from laboratory data. The stress-strain data are plotted on axes of strain/shear stress versus strain for each value of confining stress. A linear regression is then performed on each plot to obtain a best-fit relation. The inverse of the slope of the regression equation is the initial tangent modulus (E_i), whereas the inverse of the intercept is the ultimate value of principal stress difference $(\sigma_1$-$\sigma_3)_{ult}$. To determine the E_i and n parameters for the hyperbolic model, points representing E_i/P_a as a function of $(\sigma_1$-$\sigma_3)/P_a$ are plotted on a log-log scale. Linear regression yields E_i as the intercept and n as the slope of the line. The R_f values are obtained by

multiplying E_i by $(\sigma_1-\sigma_3)$ at failure and taking an average value. In its final form, the stress for a given soil is a function of the strain and normal stress. The original data points and the hyperbolic model can be superimposed to compare the model with the data.

The results obtained with the hyperbolic elastic model were used in the development of the hybrid approach to subsidence prediction described in Sect. 6.

5.2.3 Elastic-Plastic Cap Model

The residual soil has been represented by the Sandler cap elastic-plastic constitutive model (Dimaggio and Sandler, 1971). The cap model can describe the nonlinear, inelastic response observed in many soils and, unlike some plasticity models, can predict strain hardening and plastic volume change under stress paths that are primarily in the direction of increasing mean stress. This type of stress path is represented by tests such as the standard consolidation, or uniaxial strain test, and the hydrostatic test.

In an incremental elastic-plastic analysis, the total applied load is divided into a number of smaller increments, with the solution of the system of equations repeated for each increment of load. During each increment, displacements throughout the soil mass are determined, and the strains and stresses in each element are calculated. Depending on the state of stress in the element, both elastic and plastic strains may develop. An increment of total strain is assumed to consist of an elastic component and a plastic component,

$$d\varepsilon = d\varepsilon^e + d\varepsilon^p \quad , \tag{5.2}$$

where $d\varepsilon$ = total strain increment, $d\varepsilon^e$ = elastic incremental strain, and $d\varepsilon^p$ = plastic incremental strain.

The elastic component is calculated from elastic theory, while the plastic component is determined from a plastic flow or plastic potential function. For simplicity, an associative flow rule may be adopted, in which case the plastic potential function is assumed to be identical to the yield function. Thus, for an associative flow rule, the plastic strain increment vectors are normal to the yield surface.

Specific laboratory tests, such as those conducted under a hydrostatic stress path, are usually required for the determination of the elastic-plastic material parameters. After the determination of material parameters, verification is accomplished by predicting lab test data. Although the satisfactory prediction of a specific lab test may be a necessary condition for the model, it is not sufficient. In general, the constitutive model should also be capable of predicting the response over a range of stress paths.

Although a complete description of the Cap Model is not within the scope of this report, the parameters used in the analysis are provided in Table 5.1. The parameter determination process is described in Appendix B.

5.3 CONSIDERATIONS IN NONLINEAR ANALYSIS

Because the material models described in the previous sections result in a nonlinear relationship between stress and strain, the numerical solution of the governing equations must be conducted differently from customary linear elastic analysis. Rather than applying the total loads to the problem and solving directly for the displacements, a piece-wise linear approach

Table 5.1 Summary of cap model parameters

E = 1.532E+5 kPa	μ = 0.30	γ_{soil} = 18.81 kN/m^3
α = 103.4 kPa	β = 0.001279 kPa^{-1}	γ = 68.95 kPa
θ = 0.0997	T_{cut} = 50 kPa	W = 0.07
Z = 0.0 kPa	$XL_{initial}$ = 30 kPa	
R = 6.0	D = 0.001 kPa^{-1}	

is required. In a piece-wise linear analysis, the applied loads are divided into a number of load increments. A linear analysis is then conducted on each load increment in a manner similar to a linear elastic analysis, except that the material moduli change from one increment to the next as a function of the stress level. In the combined incremental-iterative solution process used with the hyperbolic material model, the load is divided into a number of increments. For each increment, several iterations of the solution are obtained until equilibrium is satisfied.

In the analyses using the elastic-plastic material model, a direct incremental solution has been used. Because no iterations of the solution are performed within any given load step, an adequate number of load steps or increments must be used. Dividing the gravitational forces into ten load increments yielded satisfactory results for the analysis of the void in the residual soil.

Two computational correction procedures were incorporated into the elastic-plastic analysis to improve the calculated stresses. At the end of each load step, the computed stresses at each stress-evaluation (integration) point were corrected back to the current yield surface, following a procedure similar to that of Potts and Gens (1985). Furthermore, because the direction of plastic flow is only correct at the beginning of a stress increment, a strain subincrementation scheme (Nyssen 1981) was adopted. The computed strain increments are divided into five subincrements, for which the incremental stress is determined. The stresses are then corrected back to the current yield surface prior to the evaluation of the next subincrement of plastic strain. The subincrementation improves the accuracy of the numerical integration and permits the use of large load steps.

5.4 STABILITY ANALYSIS OF SOIL VOID/BEDROCK CAVITY SYSTEM

5.4.1 Range of Site Geometries

The finite element analyses were conducted for a range of soil void radii r_v, from 0.3 to 4.0 m (1 to 13 ft), and overburden thicknesses, H, from 15 to 45 m (49 to 148 ft). Although no soil void data are available, r_v = 4.0 m (13 ft) is sufficiently large to exceed all probable soil voids. The range of overburden thicknesses was selected based on the variation of depth to bedrock at the East Chestnut Ridge site. In all analyses, the soil was extended 90 m (295 ft) in the horizontal direction. Table 5.2 summarizes the site geometries included in the analysis. For purposes of comparison and to determine the actual differential settlement, an analysis was also conducted with no soil void, corresponding to r_v = 0.0.

Table 5.2 Summary of investigated overburden thicknesses and soil void radii

Soil void radii, R_v[a]	Overburden thickness, H[a] 15.0	22.5	30.0	37.5	45.0
0.3	*	*	*	*	*
1.0	*	*	*	*	*
2.0	*	*	*	*	*
3.0	*	*	*	*	*
4.0	*	*	*	*	*

[a]In meters.

5.4.2 Results of Stability Analysis

Figures 5.4 and 5.5 illustrate typical results in terms of the deformed mesh and displacement vectors, respectively, for conditions of r_v = 2 m (6.5 ft) and H = 30 m (98 ft). An expansion or zoom of the left corner of the mesh is provided to highlight the deformations around the soil void. The deformed mesh indicates the final configuration of the residual soil from the gravitational load. The displacement vectors, which indicate the change in coordinates of the finite element nodal points, illustrate the displacement field. For clarity and to highlight the plastic deformation into the soil void, the displacements in both figures have been magnified by a factor of three. These figures show the formation of a subsidence basin on the surface and the plastic flow of the soil into the void. Such a deformation of the ground surface could be expected to cause tensile stresses in the upper zone of soil, similar to those in the extreme fiber of a beam in bending.

The state of stress in the residual soil can be depicted by perpendicular lines representing the magnitude and direction of the principal stresses throughout the soil domain. Typical results are shown for conditions of r_v = 2 m (6.5 ft) and H = 30 m (98 ft) in Figs. 5.6 and 5.7. Figure 5.7 is a zoom on the principal stress vectors in the region surrounding the soil void. Note that at large distances from the soil void, the major principal stress, as depicted by the larger of the two orthogonal vectors, is oriented vertically. In the region surrounding the soil void, the orientation of the principal stresses rotate. Directly above the void, the major principal stress is oriented in the horizontal direction. This rotation reflects the stress redistribution around the soil void, and the horizontal major principal stress indicates a phenomenon known as arching, which contributes to the overall stability of the

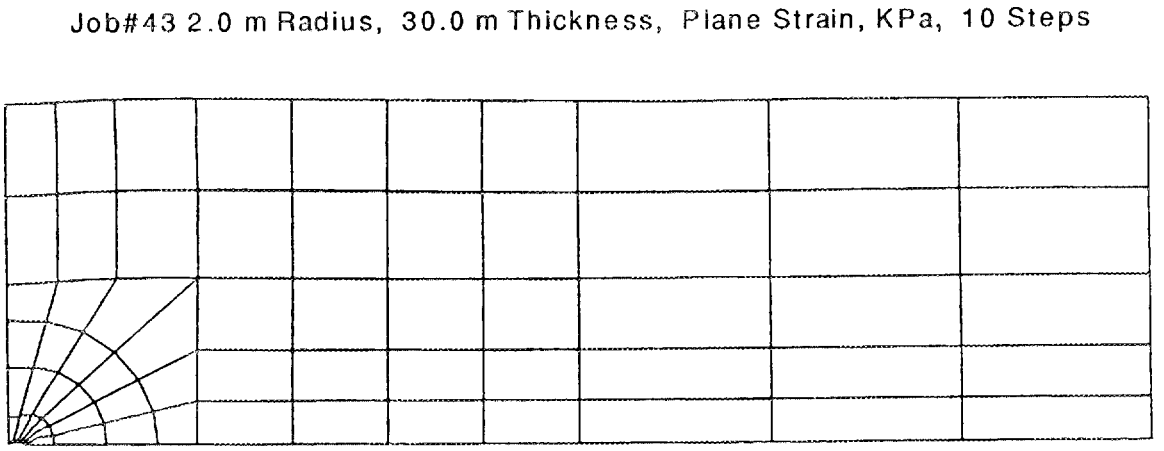

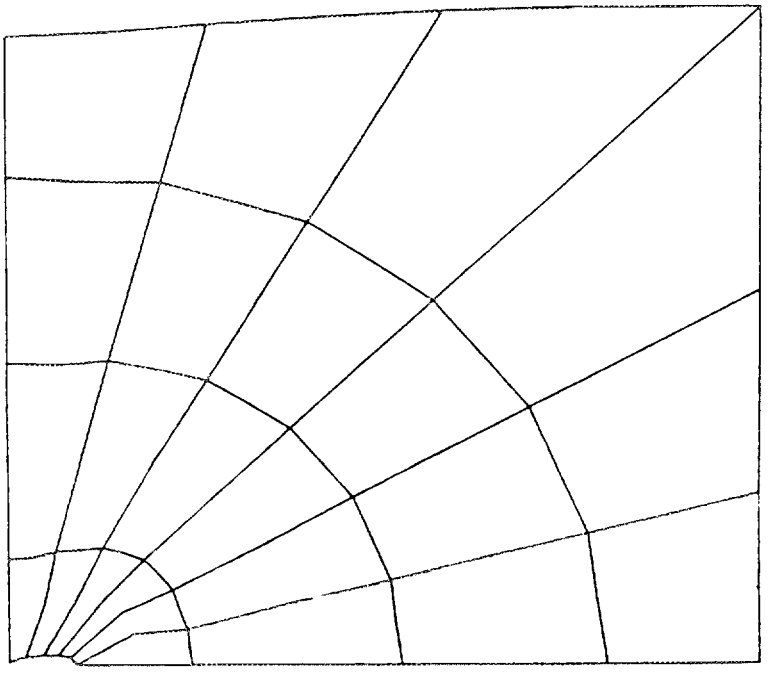

Fig. 5.4. Deformed finite element mesh, r_v = 2.0 m, H = 30 m.

ORNL-DWG 90-10405

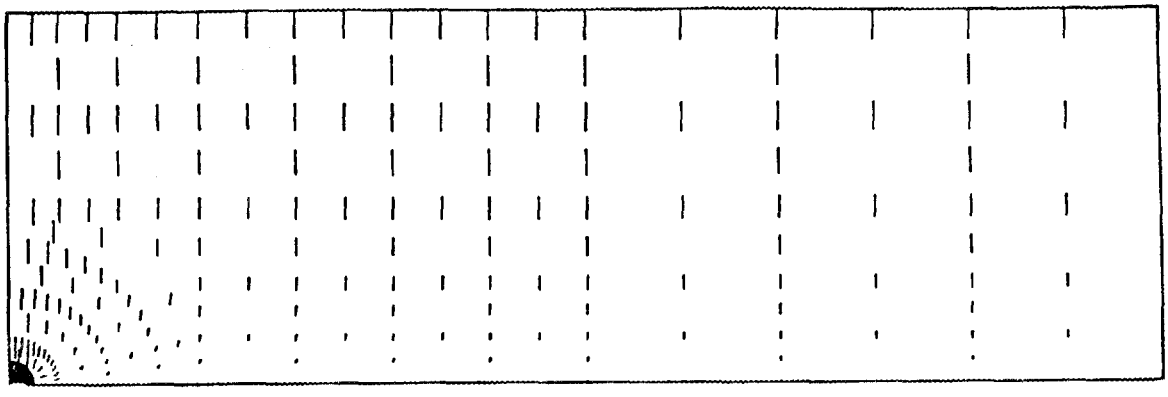

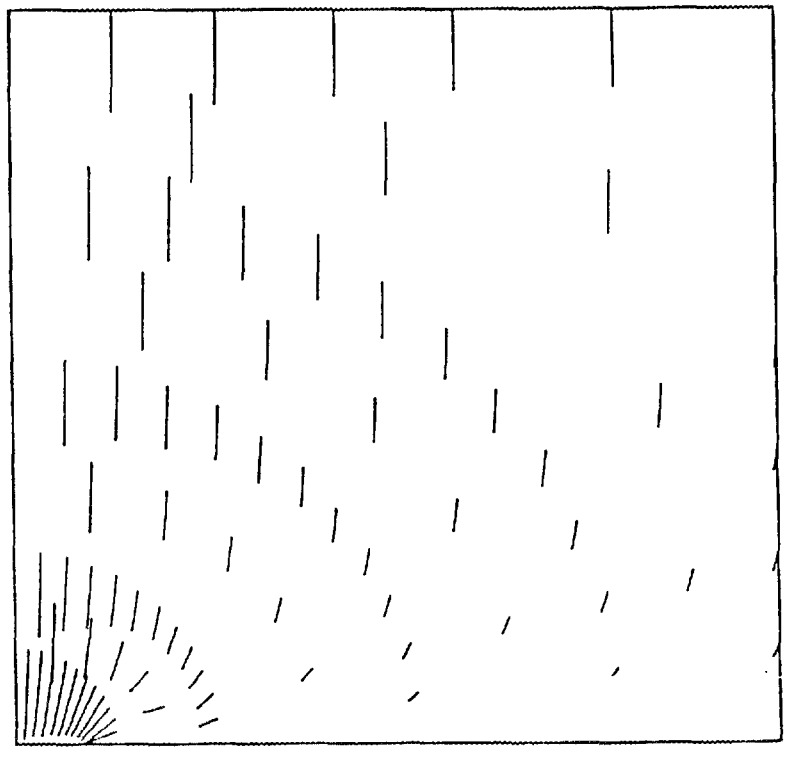

Fig. 5.5. Displacement vectors, $r_v = 2$ m, H = 30 m.

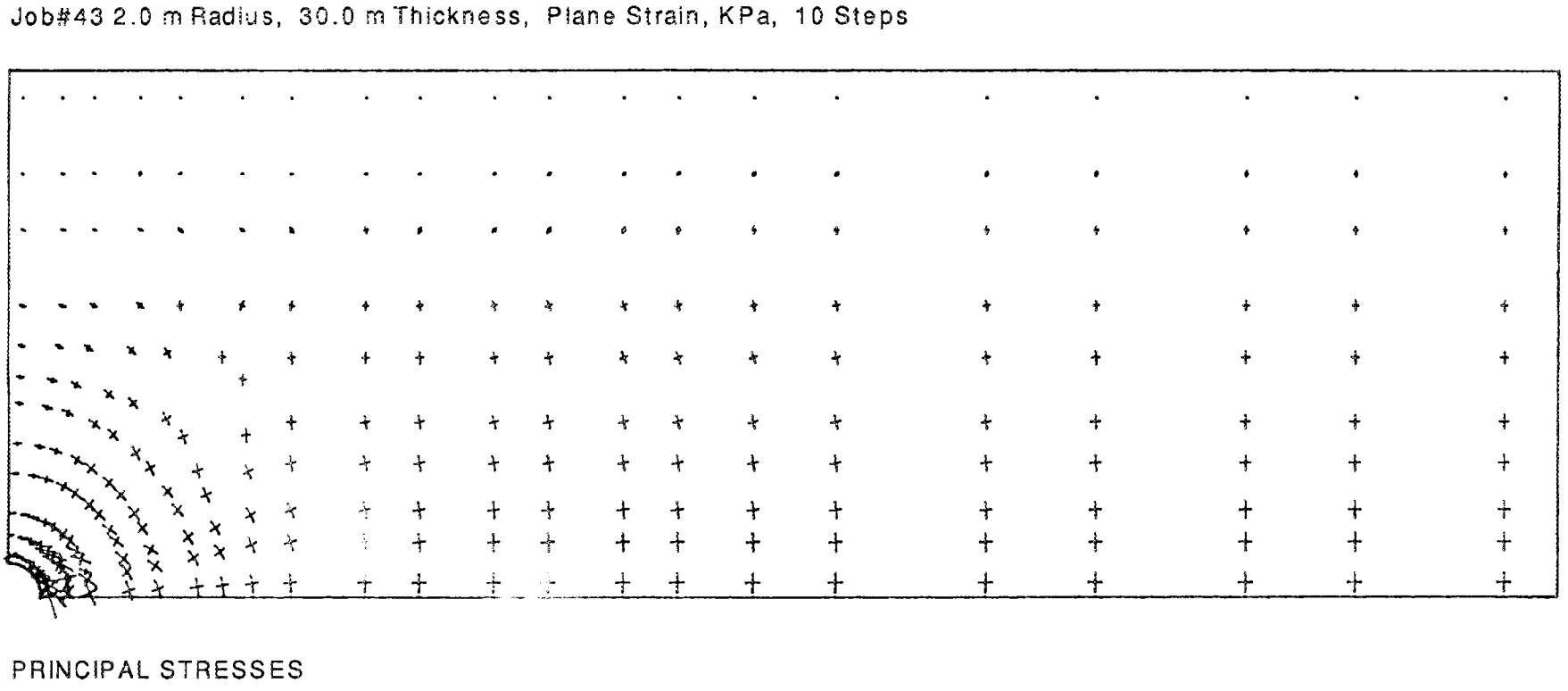

Fig. 3.6. Magnitudes and orientations of principal stress vectors, $r_v = 2$ m, H = 30 m.

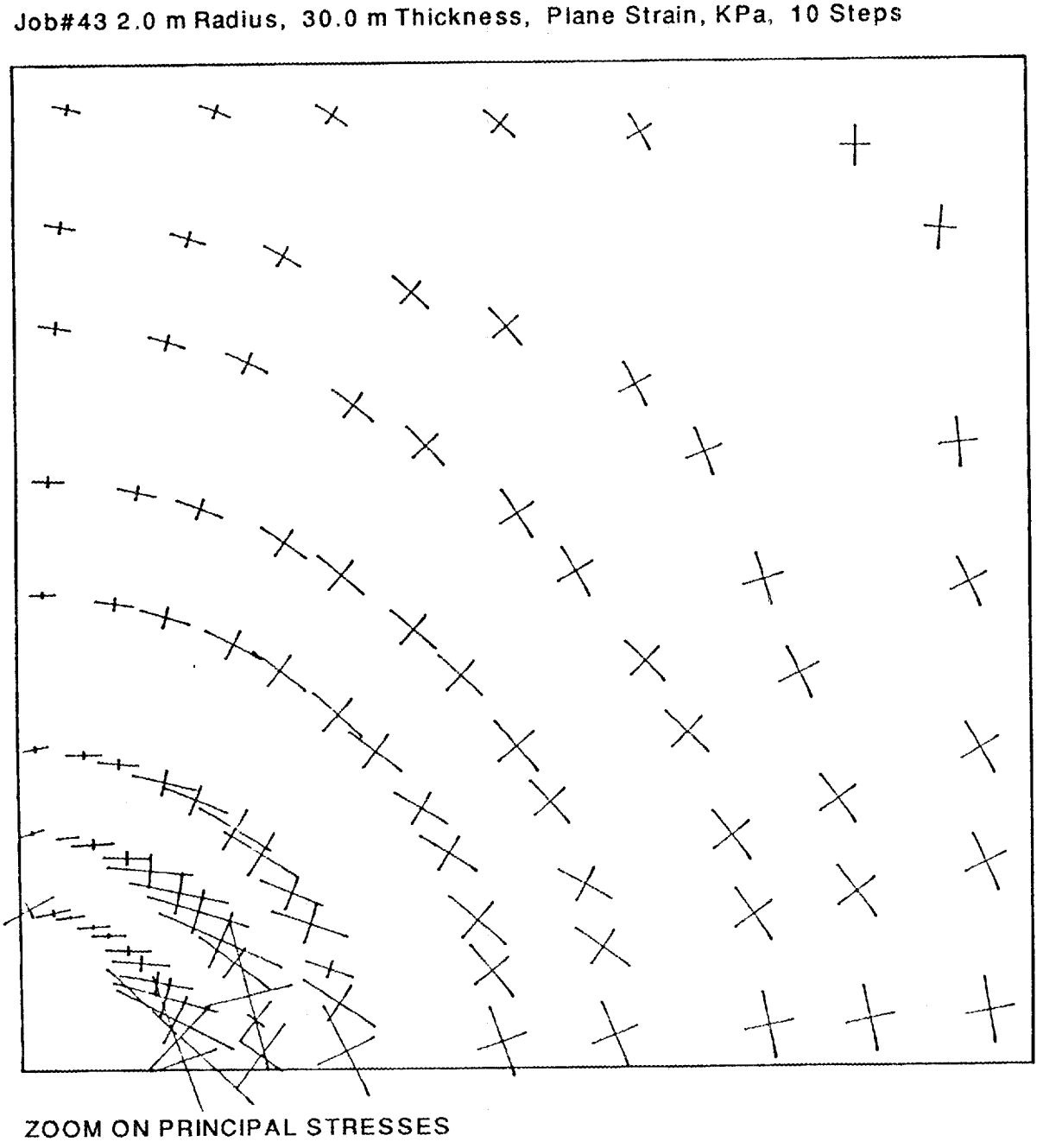

Fig. 5.7. Zoom on principal stresses around soil void, r_v = 2 m, H = 30 m.

system. This arching can not fully develop when the radius of the soil void, r_v, becomes large with respect the thickness of the overburden, H.

The effects of increasing void radius are demonstrated in Fig. 5.8 for a constant overburden thickness of 30 m (98 ft). The shaded zones indicate regions where the minor principal stress is negative, or tensile. Because the residual soil has a very low tensile strength, the shaded zones can be assumed to be near failure or susceptible to erosion. The shaded zones also correspond to regions in which the arching action is destroyed. Figure 5.8 indicates that for H = 30 m (98 ft), arching is well developed, and the tension zone remains near the surface for soil void radii less than about 2 m (6.5 ft). With r_v = 3 m (10 ft), the arching is destroyed, and the tension zone extends downward to the soil void. Under these conditions, a dropout or open sinkhole feature may be expected.

Figure 5.9 illustrates the effect of overburden thickness for a constant void radius r_v = 3.0 m (10 ft). The thick residual soil layers and corresponding large vertical stresses permit the formation of arching, and the tensile zones are restricted to the uppermost portion of the soil mass. The soil surrounding the void is stronger because of the larger confining stresses that results from the arching effects. As the thickness decreases, the arching is destroyed and the tensile zone extends through the soil to the void.

Figure 5.10 illustrates the computed stress states for conditions of r_v = 3.0 m (10 ft) and H = 45 m (148 ft). The elements are divided into quadrants corresponding to the four integration points at which the stresses are calculated. The shaded elements corresponding to tension or plastic indicate zones in which the computed state of stress is at, or above, failure. These zones contribute little to the stability of the soil mass, and if located on the surface or adjacent to the bedrock cavity, soil mass may be easily transported away.

The elastic zones indicate that the stress history of the point includes some unloading or stress reduction. These areas have experienced some yielding and plastic deformation and may be close to failure. However, these zones reflect a stable stress state.

The unshaded elements corresponding to the cap are zones in which the soil is at a state of stress hardening. Although plastic or permanent strains have developed in these areas, the stress state is stable.

Figure 5.10 indicates that a small area on the side of the soil void has failed, and much of the soil along the surface is near failure. The soil at the surface in subjected to very low confining stresses and therefore has low strength. The failure states along the ground surface correspond to the shaded tension zones for the case of r_v = 3 m (10 ft) and H = 45 m (148 ft) in Fig. 5.9. However, Fig. 5.9 illustrates the distribution of tensile stress, irrespective of failure state. Figure 5.10 depicts zones at failure, although the stress state may be compressive, such as in the area adjacent to the void. Figure 5.11 illustrates the computed stress states for conditions of r_v = 3 m (10 ft), H = 15 m (49 ft). With a decrease in overburden and the destruction of the arching effects, the failure zones have shifted to the area immediately above the void, and the system can be considered unstable. A similar conclusion can be drawn from the same case as in Fig. 5.9 [r_v = 3 m (10 ft), H = 15 m (49 ft)].

These results indicate that the stability of the soil/void system increases as void radius decreases and the overburden thickness increases. On the basis of the distribution of tensile stress as shown for typical results in Figs. 5.8 and 5.9, each geometry investigated can be categorized as stable (S), marginal (M), or unstable (U). Table 5.3 summarizes the results in terms of these categories, with the M and U categories shown in bold type. These results appear to be consistent with the conclusions of the previous study (Drumm, 1986), in which the stability was related to a decrease in the normalized cavity radius r/H. Table 5.4

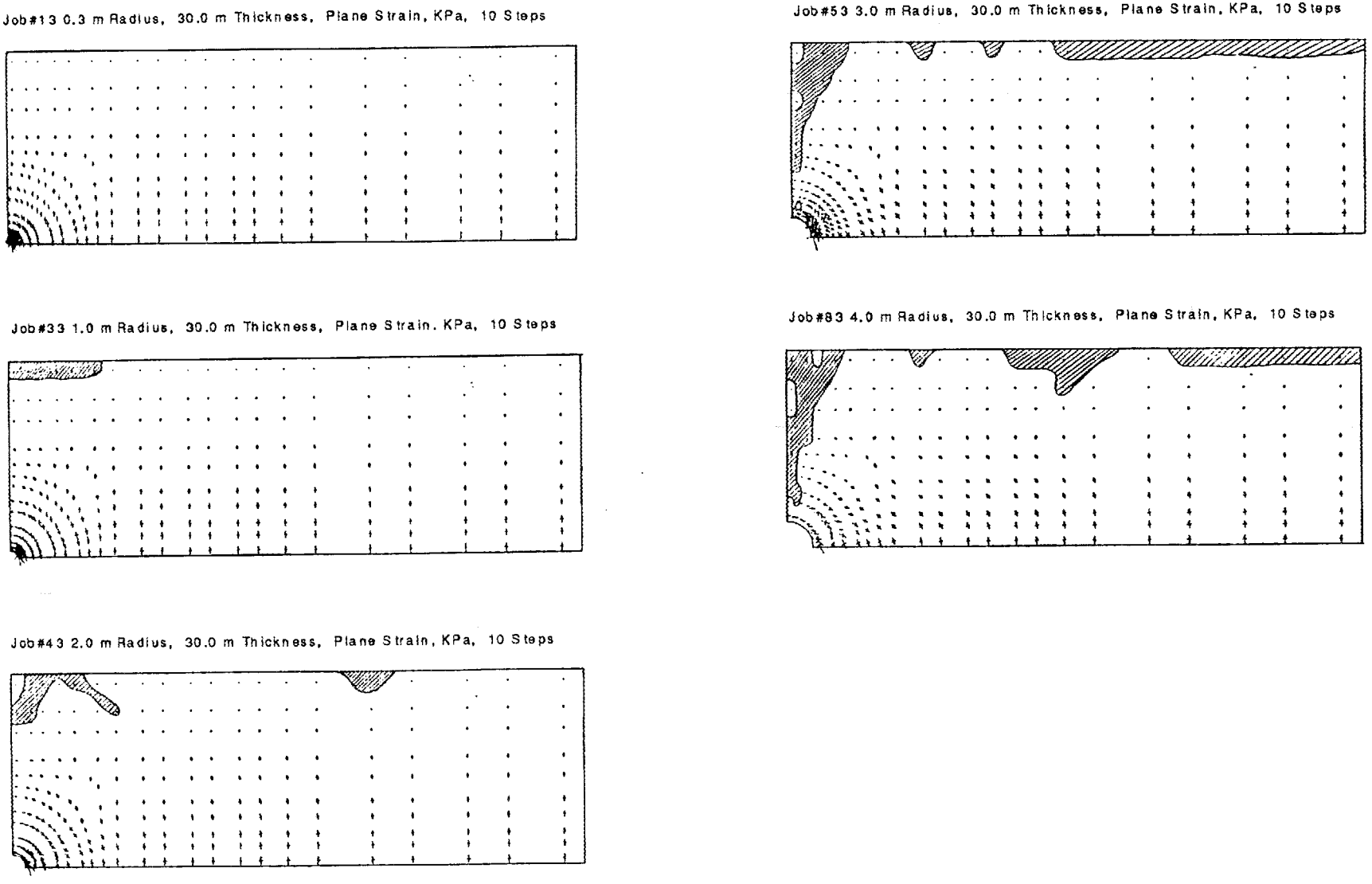

Fig. 5.8. Effect of increasing void radius, H = 30 m.

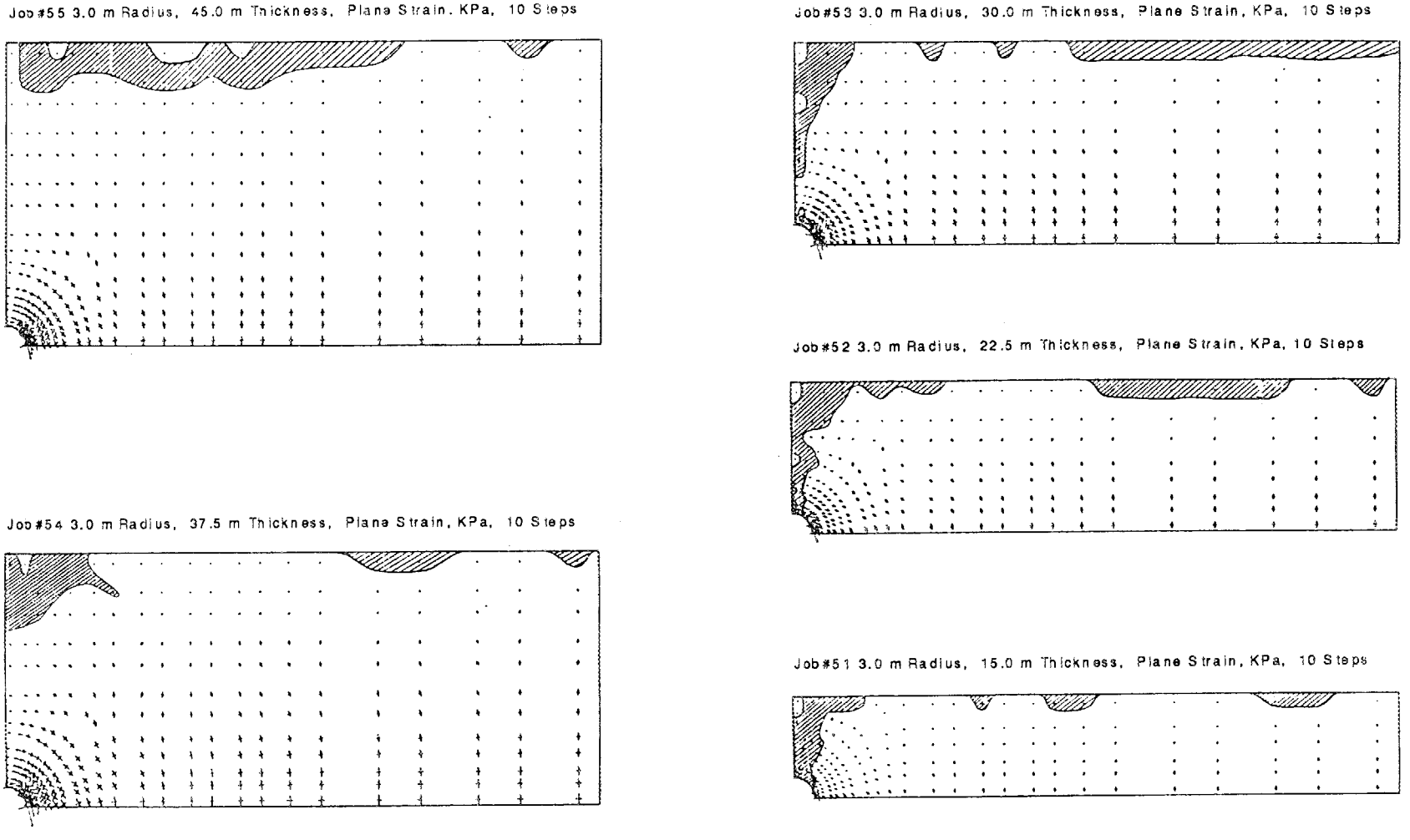

Fig. 5.9. Effect of decreasing overburden thickness, r_v = 3.0 m.

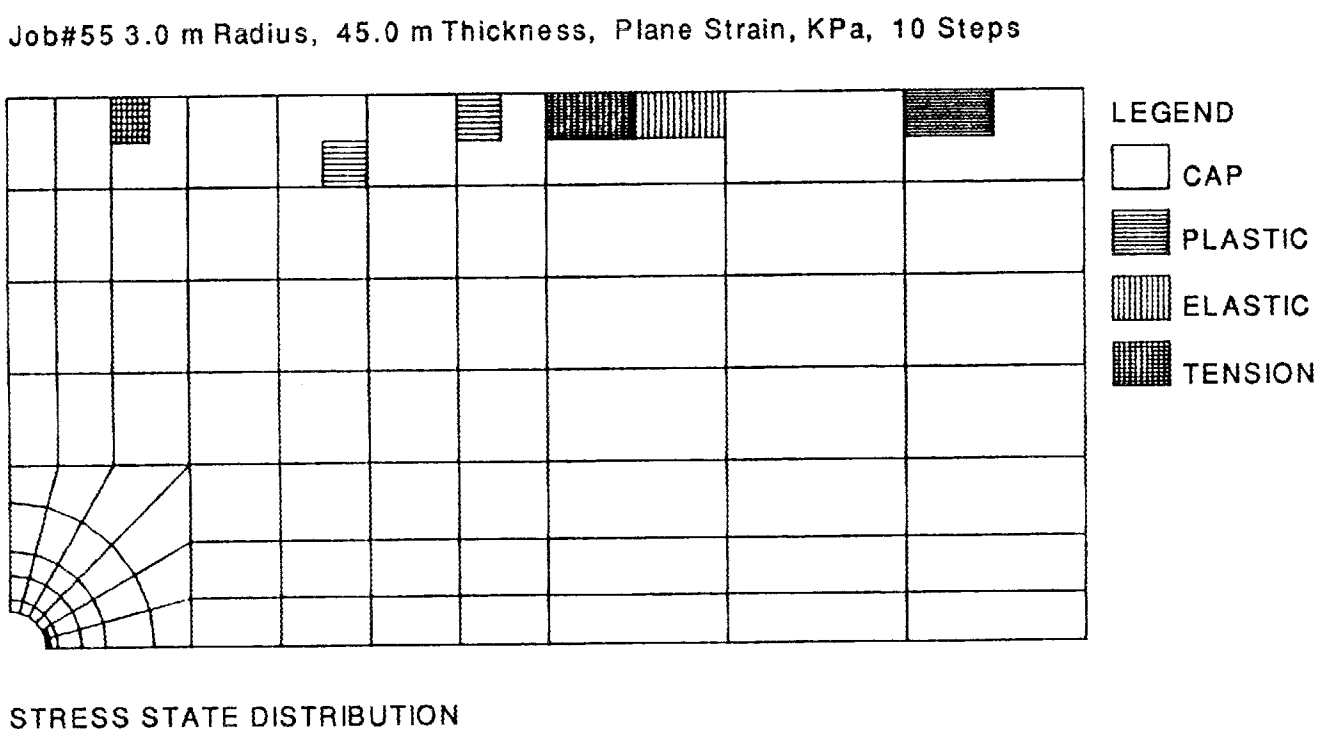

Fig. 5.10. Stress states: r_v = 3.0 m, H = 45 m.

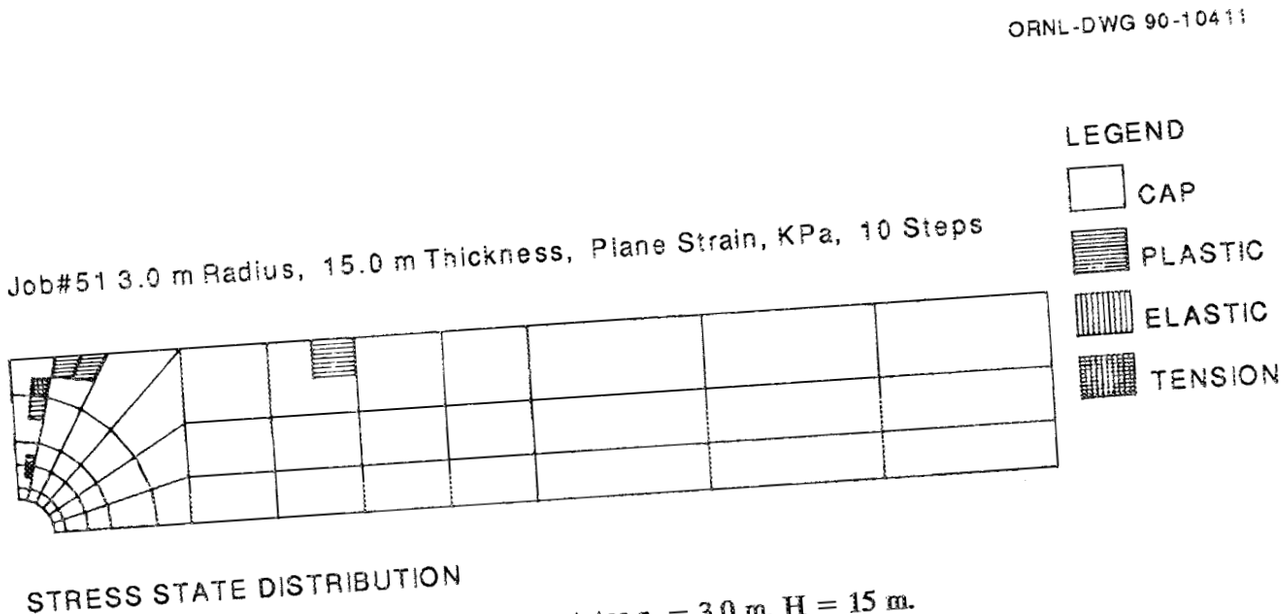

Fig. 5.11. Stress states $r_v = 3.0$ m, $H = 15$ m.

Table 5.3. Stability summary on the basis of tensile stress

Soil Void Radii, R_v (meters)	Overburden Thickness, H (m)				
	15.0	22.5	30.0	37.5	45.0
0.3	S	S	S	S	S
1.0	**M**	S	S	S	S
2.0	U	**U**	S	S	S
3.0	U	U	**M**	S	S
4.0	U	U	U	S	S
Note: S = Stable, M = Marginal, U = Unstable					

Table 5.4. Stability summary in terms of r_v/H

Soil Void Radii, R_v (meters)	Overburden Thickness, H (m)				
	15.0	22.5	30.0	37.5	45.0
0.3	0.2000	0.0133	0.1000	0.0080	0.0067
1.0	**0.0667**	0.0444	0.0333	0.0267	0.0222
2.0	**0.1333**	**0.0889**	0.0667	0.0533	0.0444
3.0	**0.2000**	**0.1333**	**0.1000**	0.0800	0.0667
4.0	**0.2667**	**0.1778**	**0.1333**	0.1067	0.0889
Bold print indicates unstable or marginal geometry					

Table 5.5. Stability summary in terms of r_v/H^2

Soil Void Radii, R_v (meters)	Overburden Thickness, H (m)				
	15.0	22.5	30.0	37.5	45.0
0.3	0.0013	0.0006	0.0003	0.0002	0.0001
1.0	**0.0044**	0.0019	0.0011	0.0007	0.0005
2.0	**0.0089**	**0.0039**	0.0022	0.0014	0.0010
3.0	**0.0133**	**0.0059**	**0.0033**	0.0021	0.0015
4.0	**0.0178**	**0.0079**	**0.0044**	0.0028	0.0020
Bold print indicates unstable or marginal geometry					

summarizes the results of this analysis in terms of the r_v/H ratio, with the marginal and unstable entries in bold print. A critical or limiting value of r_v/H ratio is not evident.

If the void radius is normalized by H^2, a summary of results as shown in Table 5.5 is obtained. Based on these results, if the normalized void radius r_v/H^2 is less than about 0.003, the soil/void system will be stable.

6. SUBSIDENCE PREDICTION USING A HYBRID APPROACH

6.1 Development of the Hybrid Approach Using a Hyperbolic Model

The subsidence of the surface due to karst activity was examined using both empirical curve fitting and numerical finite element analysis. The two-dimensional, numerical approach used a nonlinear hyperbolic elastic material model for the stress-deformation characteristics of the residual clay soil overlying cavitose bedrock. The empirical method develops the fit of a mathematical function to field profiles (Scarborough 1989). Resulting constants control the shape of predicted basins. Thirty-nine profiles from ten adjacent basins composed the field subsidence data for this study (Scarborough et al. 1989).

The pre-peak, drained behavior of the residual soil can be adequately represented by a hyperbolic stress-strain model (Duncan and Chang 1970). This model was chosen because it replicates the behavior of a soil more closely than a linear elastic model. In the hyperbolic model, Poisson's ratio is constant, while the tangent modulus is a function of the stress state and is given by Eq. 5.2. The values of the parameters used are given in Table 6.1.

Table 6.1. Material parameters for hyperbolic model

Parameter	Value
Unit weight, γ	18.8 kN/m^3
Initial tangent moduli, E_t	1.006E5 kPa
Poisson's ratio, ν	0.35
Angle of internal friction, ϕ	23°
Cohesion, C	28.7 kPa
Failure ratio, R_f	0.9
Modulus exponent, n	0.5
Modulus number, K_h	972.0
Atmospheric pressure, P_a	103.5 kPa

An incremental-iterative Newton-Raphson procedure is used in the solution of the nonlinear problem. A mid-point Runge-Kutta procedure is adopted in the sense that tangent moduli are based on the old total stresses plus half the incremental stresses to further accelerate convergence. Nodal loads equivalent to the weight of the residual soil are applied incrementally in five steps. At every load step, as many iterations as required to achieve convergence are performed. Convergence is monitored by comparing a norm based on the residual unbalanced forces in the system, with the norm based on the original applied nodal forces with a tolerance of 1%. This approach is similar to the previous analysis (Ketelle et al. 1987; Drumm et al. 1987). Convergence of the non-linear problem was consistently achieved.

A total of 25 finite element analyses were performed. The soil cavity radii considered were 0.3, 0.6, 1.0, 2.0, and 4.0 m. The thickness of overburden considered was 15.0, 22.5, 30.0, 37.5, and 45.0 m. These values of cavity radius and overburden thickness cover the

range of values anticipated at the site. The depth to bedrock (that is, the depth to refusal for borings) made in and adjacent to Sinkhole 04, is known to be 41 m (136 ft).

Figure 6.1 shows that for H = 45 m (148 ft), the observed magnitude of the vertical displacement is bracketed by numerical predictions with radii of 2 m and 4 m (6.5 ft and 13 ft), although the corresponding basin half-widths exceed observed values. The implications of this are discussed below.

The numerical analysis provides a means to examine an unknown cavity radius, a known depth of overburden, and given soil properties in terms directly related to the profile of the deformed surface.

Vertical displacement is controlled by the radius of the soil cavity. This relationship is quantified by regression on the results of the numerical analyses. An exponential relationship, with the square of the correlation coefficient, R, equal to 0.933, for maximum vertical displacement in terms of the cavity radius for the four features was determined:

$$S_o = e^{-5.46 + 2.04 r_v} , \tag{6.1}$$

where S_0 = the maximum vertical displacement, and r_v = the radius of the soil cavity. The units of both variables are in meters.

The angle of draw relates the lateral extent of subsidence at the surface to the depth of overburden. It is measured from the horizontal to a line connecting the centerline of the basin at bedrock to the half-width of the basin at the surface, as shown in Fig. 6.2. The depth of overburden is easily measured, and a known angle of draw allows estimation of the basin half-width.

Measuring the angle of draw from the centerline at bedrock, instead of from the outer edge of the cavity at bedrock as in mining, underestimates the lateral extent of the basin. For a given value of vertical displacement, an underestimated basin half-width will increase the slope and curvature of the profile. This definition of angle of draw was necessitated because the actual cavity radius in the field can rarely be determined.

The relationship defining the angle of draw can be expressed as:

$$\tan\delta = \frac{H}{L} \tag{6.2}$$

This relationship for the numerical analysis is virtually constant at $\delta = 31.9°$, with an $R^2 = 0.980$, as shown in Fig. 6.2. Considering only the single case of $r_v = 4$ m (13 ft) and H = 45 m (148 ft), the magnitude of δ increases to 47.3°, reducing the half-width. However, when a larger cavity radius, $r_v = 8$ m (26 ft), and a depth of overburden of 45 m (148 ft) were considered, convergent results were obtained up to 40% of the loading. In subsequent load increments, convergence was not achieved for any number of iterations, suggesting total collapse of the domain.

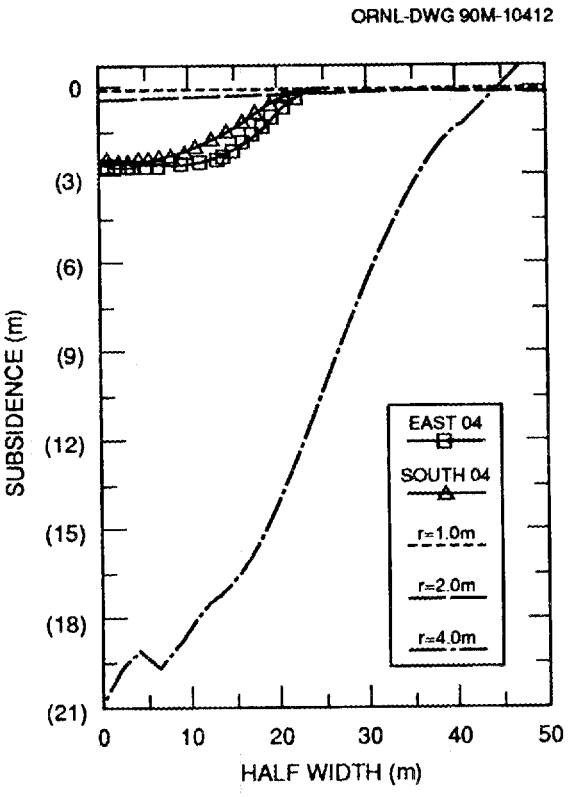

Fig. 6.1. Comparison of profile function with results of numerical analysis, H = 45 m.

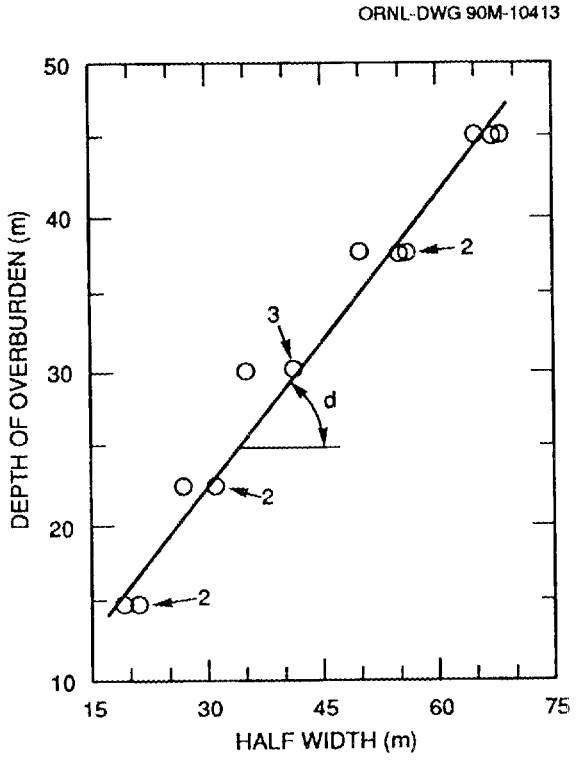

Fig. 6.2. Angle of draw obtained from numerical analysis.

In an axisymmetric analysis of slip surfaces about an open karst pipe, Yoon (1987) and Drumm et al. (1989) showed that

$$\delta = 45° + \frac{\phi}{2} \quad , \tag{6.3}$$

where ϕ = the angle of internal friction for the clay soil. Incorporating this angle for ϕ = 23° and H = 41 m (133 ft) yields δ = 57° and a predicted half-width of 27.1 m (88 ft). This value compares favorably with observed values for Sinkhole 04.

Direct substitution, of Eqs. (6.2), (6.3), and (6.4) with ϕ = 23°, into the profile function, Eq. (4.2), yields an expression for the vertical displacement at any point, X:

$$S(x) = e^{-5.46 + 2.04 r_v} e^{\alpha\left(\frac{X}{0.65H}\right)^{\beta}} \quad , \tag{6.4}$$

where: α = 2.50 and β = 3.30 are site specific empirical parameters, and r_v and h define geometry.

Figure 6.3 is a comparison of the results from Eq. (6.4) for r_v = 3.0 m, r_v = 3.14 m and r_v = 3.5 m for constant H = 41 m (135 ft) with the field profile of a typical feature, Sinkhole 04. The field and predicted curves compare favorably.

No distinct relationship was discerned in the numerical data for varying ratios of cavity radius to the depth of overburden (r_v/H) with L, the half-width of the basin, or S_0, the maximum subsidence. This ratio is significant in mining-induced subsidence (Karmis et al. 1987; Karmis 1984; Peng and Chaing 1984; and Chen and Peng 1981). The absence of a significant r_v/H relationship prevents determination of an expression only in terms of the easily determined depth of overburden. Improved methods of geophysical exploration may allow routine determination of cavity sizes for use in the model. At present, estimates based on experience or probabilistic values can be used.

6.2 SUBSIDENCE PREDICTION USING THE CAP MODEL

Profile functions can only predict subsidence where there is knowledge of subsurface geometry. Profile measurements do not, in themselves, convey information about the subsurface; correlation with actual conditions is required. Exploratory borings provide knowledge of the depth to bedrock and samples to determine soil properties. They do not provide measurements of a void in the soil overlying an enlarged solution channel.

A series of 30 analyses were conducted to characterize the deformation of the soil and soil cavity into a subadjacent bedrock void. The behavior of the soil overburden was idealized by a Sandler cap representation of the soil.

For each finite element analysis, the cavity/residual soil system was idealized in two dimensions as plane strain. The finite element formulation used eight-node, isoparametric, quadrilateral elements (Ben-Hassine 1987). The symmetric idealization of the soil-bedrock system is shown in Fig. 5.2. All applied loading occurred because of in situ gravitational forces, while hydraulic forces were neglected. The soil cavity radii considered were 0.3, 0.6, 1.0, 2.0, 3.0 and 4.0 meters. The thickness of overburden considered was 15.0, 22.5, 30.0,

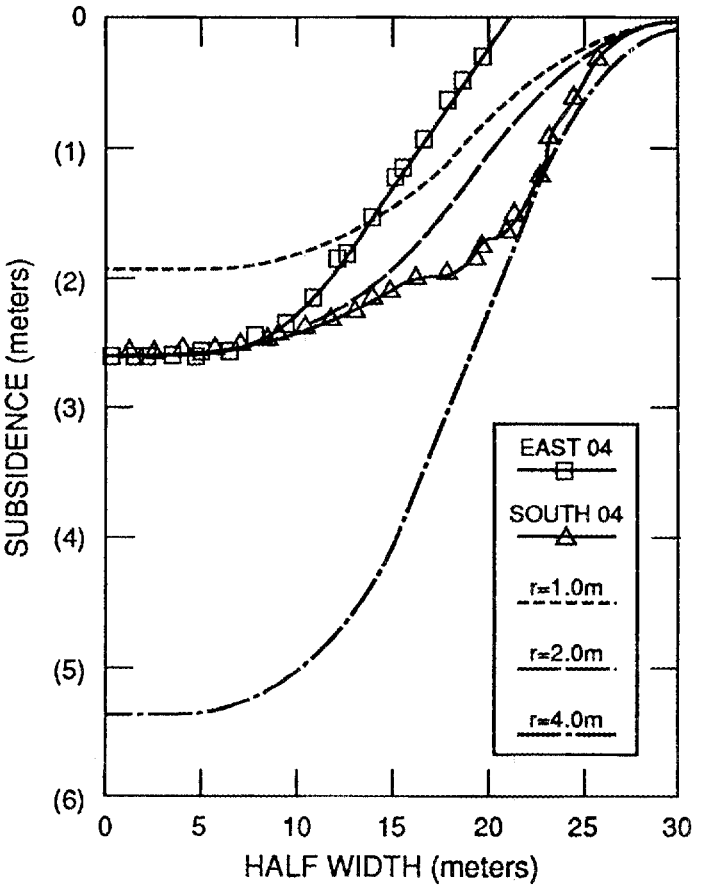

Fig. 6.3. Comparison of field measurement with hybrid method for various r_v

37.5, and 45.0 meters. These values of cavity radius and depth of overburden cover the range found at East Chestnut Ridge.

Analysis of the results from the cap model finite element series identified two significant relationships: (1) the maximum vertical displacement is partially controlled by the radius of the soil cavity as shown in Fig. 6.4, and (2) there is a linear relationship between basin half-width and the depth of overburden (Fig. 6.5).

An expression for the relationship between cavity radius and subsidence was found from regression, with $R^2 = 0.929$. Maximum vertical displacement expressed in terms of cavity radius is:

$$S_0 = 0.74r^{1.11} \quad , \tag{6.5}$$

where S_0 = the maximum vertical displacement, and r_v = the radius of the soil cavity, both in meters.

The angle of draw was constant, $\delta = 60.8°$, as determined by linear regression. This compares favorably with the value of $\delta = 56.3°$ from field observations.

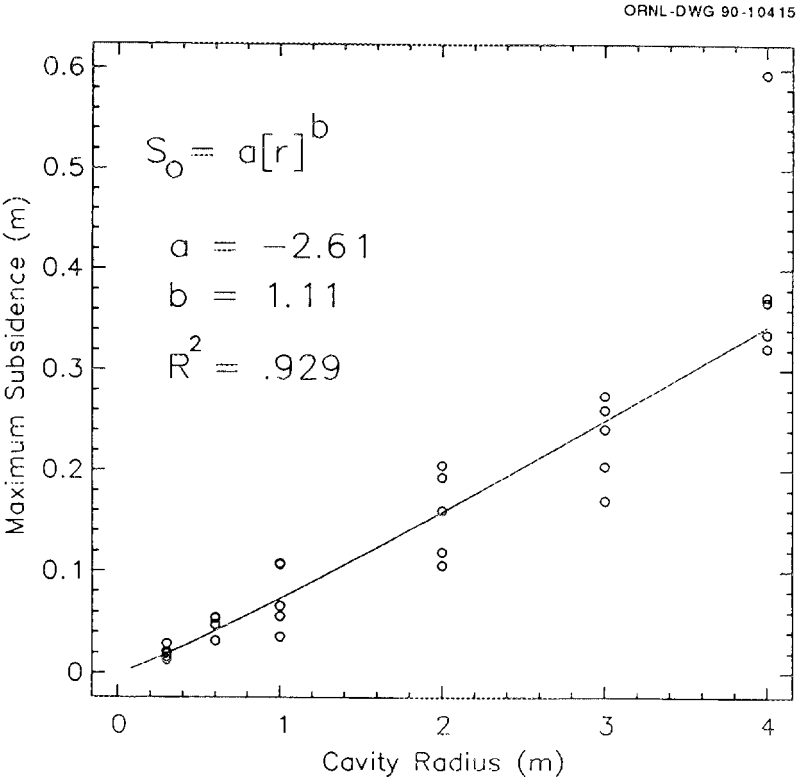

Fig. 6.4. Exponential relationship between cavity radius and maximum subsidence from the cap model analysis.

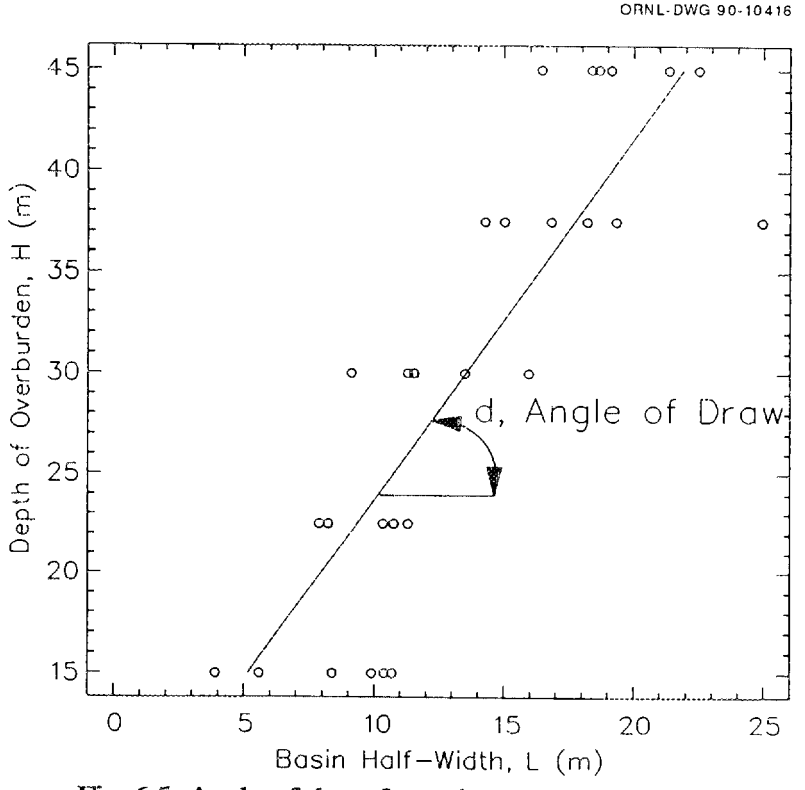

Fig. 6.5. Angle of draw from the cap model analysis.

A relationship between the distance to the inflection point and the half-width was determined from the finite element analysis, as shown in Fig. 6.6. This relationship, with R^2 = 0.656, is linear and can be represented by the expression:

$$B = 1.24 + 0.42L \quad , \tag{6.6}$$

where B = the distance to the inflection point and L = the half-width of the subsidence basin, both in meters. Again, the intercept is small relative to the variable and can be neglected. The value of 0.49 suggests that the profiles can be generally described as not having a flat bottom, with the maximum subsidence occurring only at a single point. This relationship between L and B provides the means for locating the inflection point in a predictive model. Geometric parameters defining the fit of both profile functions to the numerical subsidence basins is presented in Appendix B.

The basins resulting from the series of numerical analysis using the cap model are compared with field values in Fig. 6.7 and show the following:

1. small values of S_0 for large cavity radii [smaller than the field average of 2.0 m (6.5 ft)]
2. angles of draw that more closely match field observations than does the angles obtained with the hyperbolic model, and
3. profiles that are not smooth, reflected in a relatively low value of R^2.

The first finding suggests that hydraulic forces must play a significant role in determining maximum subsidence as suggested by Chen and Beck (1989). Raveling and flow of overburden material into the subsurface rock cavities provides more surface subsidence than predicted by a model neglecting these forces.

Direct substitution of Eq. 6.5, maximum subsidence, S_0, as a function of soil cavity radius, into the predictive exponential function (Eq. 4.2) yields the following expression for the vertical displacement at any point:

$$S(x) = S_0 e^{\alpha\left(\frac{x}{0.56H}\right)^{\beta}} \quad , \tag{6.7}$$

$$\textit{where} \quad S_0 = 0.074r^{1.11}$$

All distance variables are experessed in meters. A comparison of the profile function predictions with the actual values is shown in Fig. 6.8. Once again, the underprediction of maximum subsidence indicates that agents other than material properties serve to affect displacements.

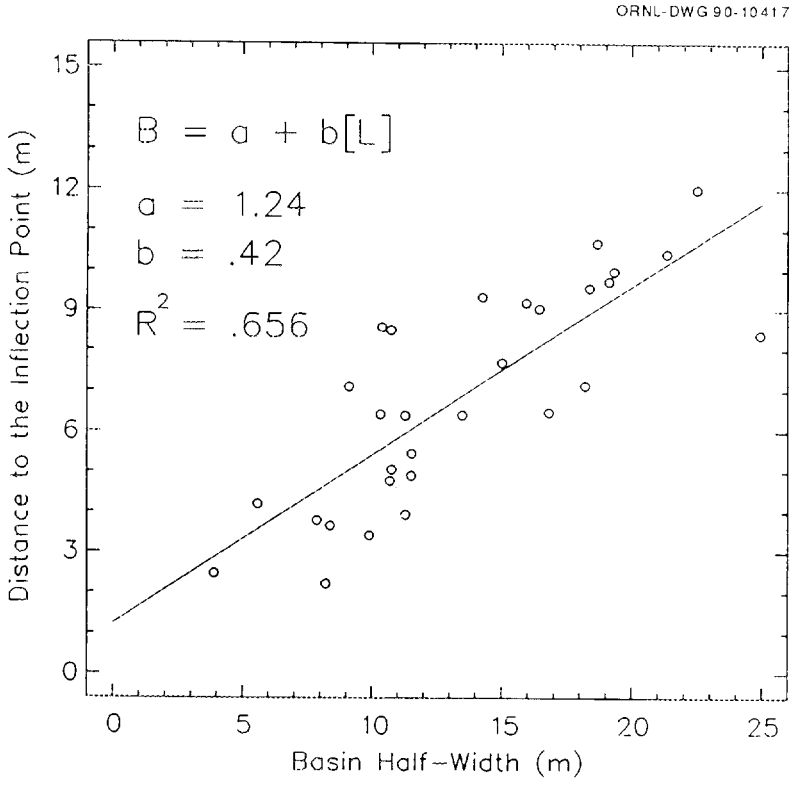

Fig. 6.6. Location of the inflection point relative to basin half-width from the numerical analysis.

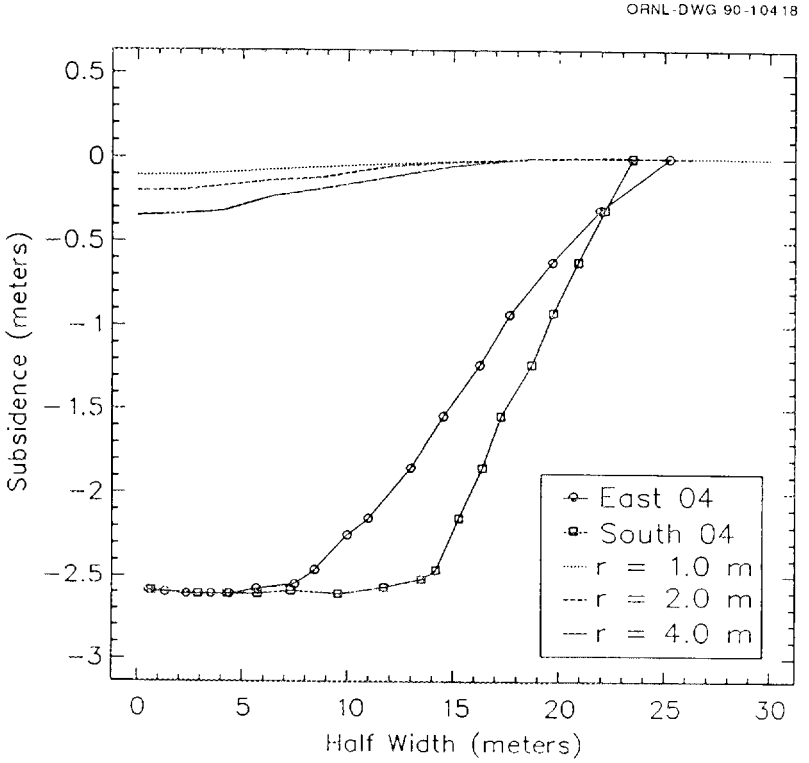

Fig. 6.7. Comparison of profiles from the cap model, H = 45 m, with field profiles.

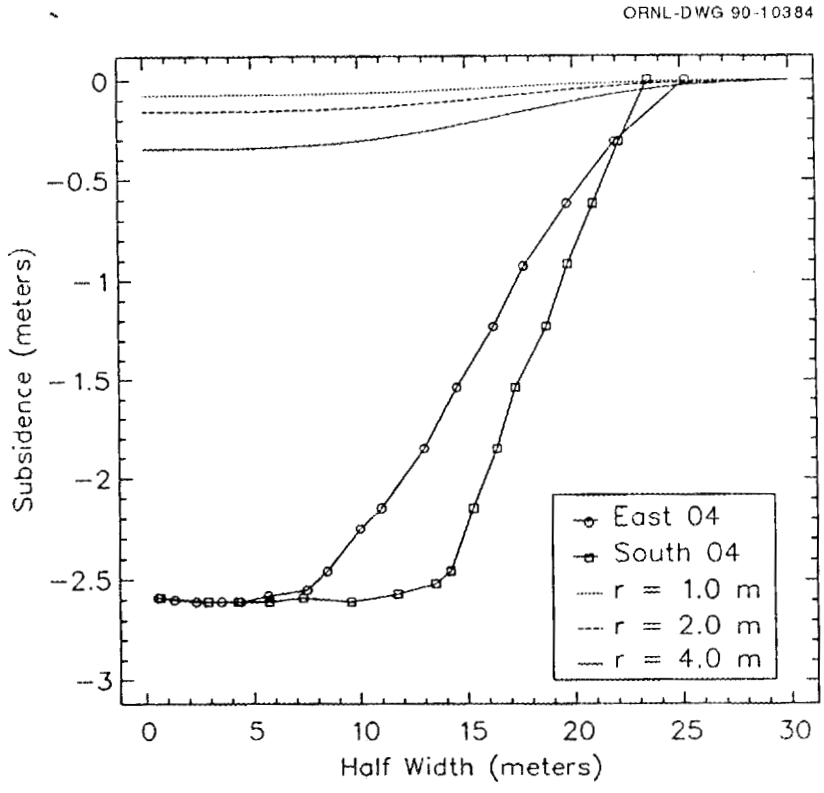

Fig. 6.8. Comparison of profile function results from hybrid cap model with sinkhole 04 field profiles, H = 45 m.

7. CONCLUSIONS AND RECOMMENDATIONS

7.1 CONCLUSIONS

The siting of waste storage facilities in karst terrain requires consideration of the impact of existing and future karst activity on the containment integrity. The East Chestnut Ridge site, Oak Ridge, Tennessee, which is currently under consideration for disposal of sanitary and industrial wastes, contains numerous karst features.

Subsidence of the ground surface in karst areas can lead to excessive deformation and damage to soil and/or membrane liner systems placed below waste storage facilities. Subsidence prediction requires knowledge of a relationship between the lateral and vertical extent of deformation and its driving force(s). The irregular and inaccessible nature of the bedrock surface in karst terrain necessitates the use of an idealized analysis to quantify relationships between unknowns.

As part of the evaluation of the East Chestnut Ride Ridge site, an analysis has been conducted to investigate the stability of the existing karst features and to develop a method to predict the magnitude and lateral extent of the karst-induced surface subsidence.

The analysis consists of four major aspects:

1. Field reconnaissance, level surveying, and mapping of the numerous karst features identified on the site. Contour maps of eight significant features were produced.
2. The development of profile functions to mathematically predict the surface subsidence. Profile functions, similar to those employed in the mining industry, were developed based on the observed subsidence profiles.
3. A series of finite element (FE) analyses covering the anticipated range of soil overburden thicknesses and soil cavity radii were conducted. These analyses were conducted to evaluate the stability of possible soil voids that may exist above bedrock cavities, and to predict the surface subsidence. Laboratory test data reported from samples taken from the site were used to characterize the material behavior in the FE analyses.
4. Development of hybrid FE/profile functions to estimate the magnitude and lateral extent of surface subsidence at the East Chestnut Ridge site.

The results of the stability analysis indicate that although substantial surface subsidence can occur, the soil void system is essentially stable, provided the soil void radius is small with respect to the overburden thickness. A normalized void radius r_v/H^2 of approximately 0.003 is the limit of stability. Based on the results of the numerical analysis, a profile function has been developed to predict the vertical displacement of a point on the surface as a function of the void radius and overburden thickness. For the East Chestnut Ridge site, this function is expressed as:

$$S(x) = 0.074 r^{1.11} e^{-\alpha\left(\frac{x}{0.56H}\right)^{\beta}} , \qquad (7.1)$$

where: $\alpha = 2.50$ and $\beta = 3.30$ are site specific parameters, and r and H define geometry.

The conclusions of this investigation can be summarized as follows:

1. The size of the soil void controls the magnitude of subsidence for a given overburden depth.
2. The numerical results indicate a *constant angle of draw*, controlled by soil properties, notably the effective friction angle of the soil. *Thus, the lateral extent of subsidence will be governed by the thickness of the residual soil above bedrock.*
3. A numerical expression can be obtained to describe the shape of the subsidence profile as a function of the void and overburden dimensions.
4. The East Chestnut Ridge site is stable provided the normalized void radius, r_v/H^2, is less than about 0.003.
5. The magnitude of predicted subsidence obtained from the finite element analysis is much less than observed. This indicates that other mechanisms (for example, seepage forces and erosion) are also involved.

Use of the finite element method can, with an adequate material model, provide reasonable estimates of the distribution of stress and stress states. Empirically derived profile functions can provide an estimation of the lateral extent of subsidence consistent with observed field conditions. Integration of the two in a hybrid approach provides a prediction tool for the complete subsidence basin profile. This is critical in the determination of the slope and curvature of the profile necessary for the damage assessment of structural components such as clay or geotextile landfill liner systems.

7.2 RECOMMENDATIONS FOR FURTHER STUDY

The analysis described in this report contributes significantly to our understanding of the mechanisms governing the stability and deformation of the ground surface in karst terrain. Several simplifying assumptions were employed in this analysis. At least two areas warrant additional study: (1) effects of factors not considered in current analysis and (2) field verification and application of results.

7.2.1 Effects of Factors Not Considered in Current Analysis

Because this tudy was a first approximation, the following effects were not considered in the analysis. These effects should be considered in subsequent evaluations:

- **Cyclic water table.** A constant water table within the cavernous bedrock was assumed in the present analysis. Fluctuations in the water table result in the cycling of the effective stresses within the soil and load reversal in the region surrounding the soil void. This causes caving within the void, thereby increasing instability. The cyclic loading effects from water table variations can be evaluated by repeating the analysis for numerous cycles of water table variations. However, an appropriate material model must be used for the soil.
- **Seepage forces.** Seepage forces resulting from the downward flow of water from the surface increase the body forces applied to the soil cavity system. The effects of the seepage forces will most likely increase the computed stresses, deformations, and magnitudes of subsidence. Seepage forces were neglected in the present analysis.

- **Mass transport.** Mass transport was also not considered in the current analysis. The effects of erosion and mass transport, both at the ground surface and within the soil void, can be expected to affect the surface profile and the stress state around the soil void.

Figure 2.5 supports the premise that hydraulic effects are important. The majority of the sinkholes were formed during periods of rainfall. Rain-induced groundwater fluctuations affect sinkhole stability, particularly in cavernous underground systems where the groundwater table responds quickly to precipitation. The cavern system provides an efficient means of groundwater recharge, resulting in rapid surges in the water table elevation. The water table variations are accompanied by the cyclic loading of the system and mass transport or erosion effects. The effects of these hydraulic variables on sinkhole behavior should be investigated. This investigation may include an analysis of the East Chestnut watershed and an evaluation of the subsurface hydrologic system.

- **Additional geometric effects.** The current analysis employed a plane strain idealization to investigate the stability around circular soil voids of large linear extent, such as those that would occur along a fracture in the bedrock. The analysis could be extended to include multiple or adjacent voids, sloping ground surfaces, or three-dimensional effects.

7.2.2 Application of Results and Verification by Field Studies

Future investigations should include some field verification of the results of this analysis and the practical application of the results to engineering problems.

- **Field Verification.** The analysis resulted in threshold values for the soil void and overburden thickness, such that the system is stable. Geophysical methods can be used to detect voids in the residual soil and estimate the void size. These investigations should be conducted in areas where a range of overburden thicknesses occurs. These field data can be used to verify the results of the numerical analysis or provide assurance that voids larger than a given size do not exist. Quality field data can also be used to tune the numerical model to better approximate the conditions on East Chestnut Ridge.
- **Practical Application of Analysis Results.** This investigation was conducted to evaluate the stability of the residual soils for the possible construction of waste facilities. The results should now be applied to determine the effects of the predicted surface deformations and curvatures on containment structures, clay liners, and geotextiles. An investigation of this type should include both laboratory/field testing of liner materials and should be supported by additional numerical analysis. Through such an investigation of the effects of surface deformations on constructed facilities, the logical application of this research can be achieved.
- **Data requirements for additional investigation.** Existing water table records (piezometer data) could be used in the numerical analysis to investigate effects of water table variation on stresses and deformations of the residual soils. A study of the surface and subsurface hydrologic system could be helpful in relating this to actual rainfall activity.

Because the Knox Group soil properties are well-defined, additional soil testing is probably not warranted, and such an analysis could be conducted with the existing data. However, if additional analysis were to be conducted to include hydraulic effects, some additional, limited specialized testing is necessary.

REFERENCES

Beck, B.F. 1984. "Sinkhole Terminology," pp. ix–x in *Proceedings of the First Multidisciplinary Conference on Sinkholes, Orlando, Florida.*

Ben-Hassine, J. 1988. "Finite Element Applications in the Analysis of Nonlinear Problems in Geomechanics," M.E. thesis, University of Tennessee, Knoxville.

Brauner, G. 1973. "Subsidence Due to Underground Mining (in two parts)," Information Circular 8571, U.S. Bureau of Mines.

Chen, D. and Peng, S.S. 1981. "Analysis of Surface Subsidence Parameters due to Underground Longwall Mining in the Northern Appalachian Coalfield," Technical Report 81-1, Department of Mining Engineering, West Virginia University.

Desai, C.S., and Lightner, J.G. 1985. "Mixed Finite Element Procedure for Soil Structure Interaction and Construction Sequences," *International Journal for Numerical Methods in Engineering*, 21(5), 801–24.

DiMaggio, F.L., and Sandler, I.S. 1971. "Material Model for Granular Soils," *Journal of the Engineering Mechanics Division, ASCE*, 97(EM3), 935–50.

Drumm, E.C. 1986. "Soil Mechanics and Analysis of Soils Overlying Cavitose Bedrock," ORNL/SUB/86-41B-07685C, Oak Ridge, Tenn.

Drumm, E.C., Kane, W.F. and Yoon, C.J. 1990. "Application of Limit Plasticity to the Stability of Sinkholes," *Engineering Geology*, in press.

Drumm, E. C., Ketelle, R.H., Manrod, W.E., and Ben-Hassine, J. 1987. "Analysis of Plastic Soil in Contact with Cavitose Bedrock," pp. 418–31 in *Proceedings of the ASCE Specialty Conference on Geotechnical Practice for Waste Disposal, Ann Arbor Michigan.*

Duncan, J.M. and Chang, C.Y. 1970. "Nonlinear Analysis of Stress and Strain in Soils," *Journal of Soil Mechanics, Foundation Division, ASCE* 96(SM5), 1629–653.

Geologic Associates 1989. *East Chestnut Ridge Soil Investigation, Oak Ridge, Tennessee,* ERC/EDge File No. B435, report to Martin Marietta Energy Systems, Inc., Oak Ridge, Tennessee.

Janbu, N. 1963. "Soil Compressibility as Determined by Oedometer and Triaxial Tests," pp. 19–25 in *European Conference on Soil Mechanics and Foundation Engineering, Wiesbaden, Germany,* Vol. 1.

Karmis, M., Goodman, G. and Hasenfus G. 1984. "Subsidence Prediction Techniques for Longwall and Room and Pillar Panels in Appalachia," pp. 541–53 in *Proceedings of the 2nd Conference on Stability in Underground Mining.*

Karmis, M., ed. 1987. *Prediction of Ground Movements due to Underground Mining in the Eastern United States Coalfields, Vol 1: Development of Prediction Techniques,* published by Dept. of Mining and Minerals Engineering, Virginia Polytechnic Institute and State University.

Kemmerly, P.R. 1980. *Sinkhole Collapse in Montgomery County Tennessee,* Tennessee Division of Geology, Environmental Geology Series No. 6.

Ketelle, R. H. and Huff, D. D. 1984. *Site Characterization of the West Chestnut Ridge Site,* ORNL/TM-9229, Oak Ridge National Laboratory, Oak Ridge, Tenn.

Ketelle, R.H., Drumm E.C., Ben-Hassine, J. and Manrod, W.E. 1987. "Soil Mechanics Analysis of Plastic Soil Deformation over a Bedrock Cavity," pp. 383–87 in *Proceedings of the 2nd Multidisciplinary Conference on Sinkholes and the Environmental Impacts of Karst.*

Kondner, R.L. 1963. "Hyperbolic Stress-Strain Response: Cohesive Soils" *Journal of the Soil Mechanics and Foundation Division ASCE* 89(SM1), 115–43.

Kulhawy, F.H., Trautmann, C.H., Beech, J.F., O'Rourke, T.D., and McGuire, W. 1983. *Transmission Line Structure Foundations for Uplift-Compression Loading,* EPRI EL-2870, report prepared for Electric Power Research Institute, Palo Alto, Calif.

Newton, J.G. 1976. "Early Detection and Correction of Sinkhole Problems in Alabama, with a Preliminary Evaluation of Remote Sensing Applications," Alabama Highway Department.

Newton, J.G. and Tanner J.M. 1986. *Regional Inventory of Karst Activity in the Valley and Ridge Province, Eastern Tennessee, Phase I,* ORNL/Sub/11-78911/1, Oak Ridge National Laboratory, Oak Ridge, Tenn.

Nyssen, C. 1981. "An Efficient and Accurate Iterative Method, Allowing Large Incremental Steps, To Solve Elasto-Plastic Problems," *Journal of Computers & Structures* **13**, pp. 63–71.

Ogden, A.E. 1984. "Methods for describing and Predicting the Occurence of Sinkholes," pp. 177–82 in *Proceedings of the First Multidisciplinary Conference on Sinkholes, Orlando, Florida*.

Peng, S.S. and Chaing, H.S. 1984. *Longwall Mining,* John Wiley and Sons, New York.

Scarborough, J.A. 1989. "Estimation and Impact of Surface Subsidence in a Karst Terrain," M.S. thesis, University of Tennessee, Knoxville.

Potts, D. M. and Gens, A. 1985. "A Critical Assessment of Methods of Correcting for Drift from the Yield Surface in Elasto-Plastic Finite Element Analysis," *International Journal for Numerical and Analytical Methods in Geomechanics* **9**, 149–59.

STSC 1988. *STATGRAPHICS, Statistical Graphics System User's Guide, University Edition,* Statistical Graphics Corporation, Rockville, Md.

Woodward-Clyde Consultants 1984. *Subsurface Characterization and Geohydrologic Evaluation, West Chestnut Ridge Site,* ORNL/Sub/83-647/641/Vol. 1-2, Oak Ridge National Laboratory, Oak Ridge, Tenn.

Yoon, C.J. 1987. "Slip Surfaces in Sinkholes: An Analysis of the Slip Line of an Axisymmetric Open Karst Pipe," M.S. thesis, University of Tennessee, Knoxville.

APPENDIX A: CONTOUR MAPS OF SINKHOLES

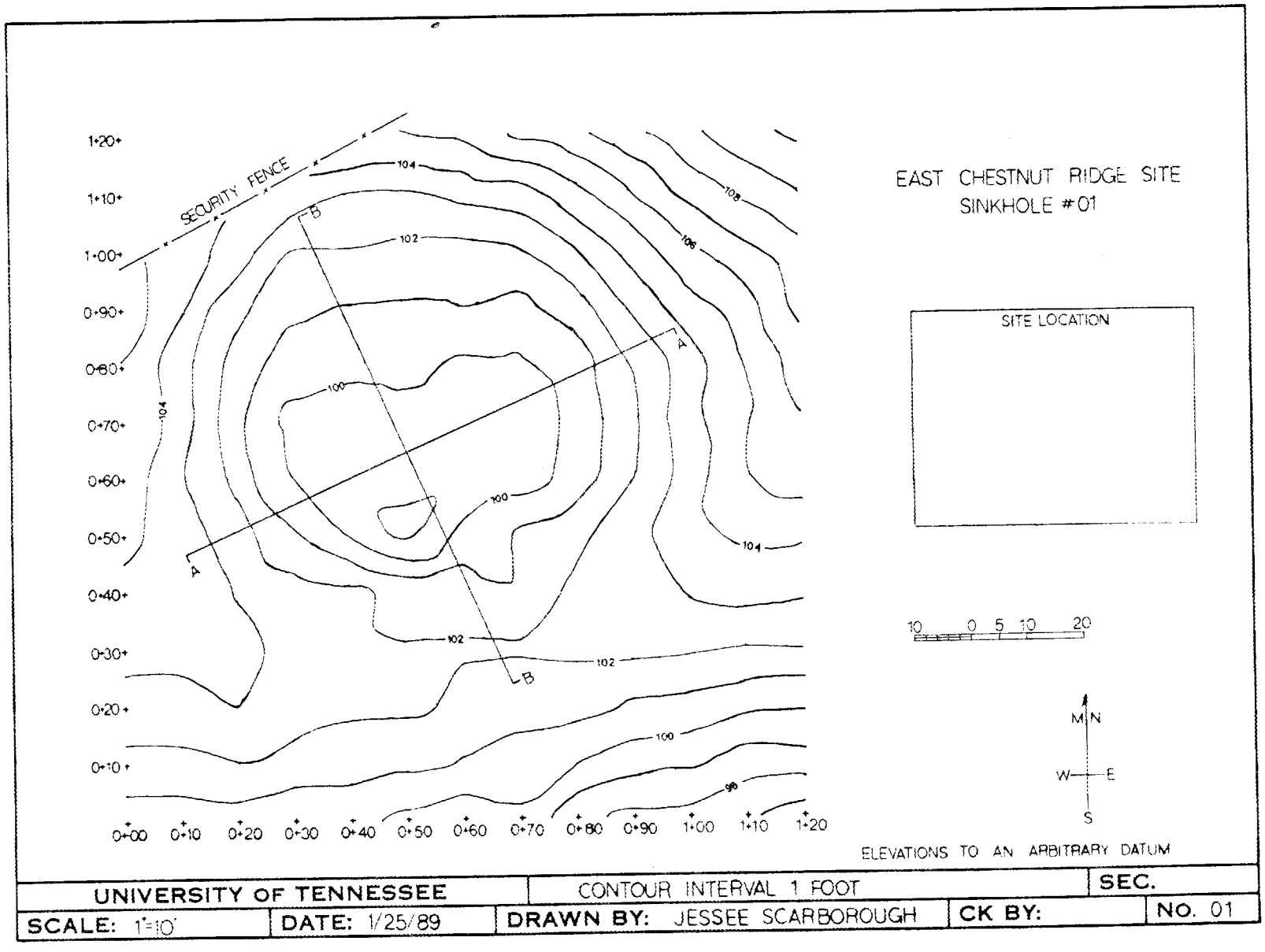
EAST CHESTNUT RIDGE SITE
SINKHOLE #01
SITE LOCATION
SECURITY FENCE
A
B
104
102
100
98
106
108
1+20+
1+10+
1+00+
0+90+
0+80+
0+70+
0+60+
0+50+
0+40+
0+30+
0+20+
0+10+
0+00
0+10
0+20
0+30
0+40
0+50
0+60
0+70
0+80
0+90
1+00
1+10
1+20
10 0 5 10 20
N
W
E
S
ELEVATIONS TO AN ARBITRARY DATUM
UNIVERSITY OF TENNESSEE
CONTOUR INTERVAL 1 FOOT
SEC.
SCALE: 1"=10'
DATE: 1/25/89
DRAWN BY: JESSEE SCARBOROUGH
CK BY:
NO. 01

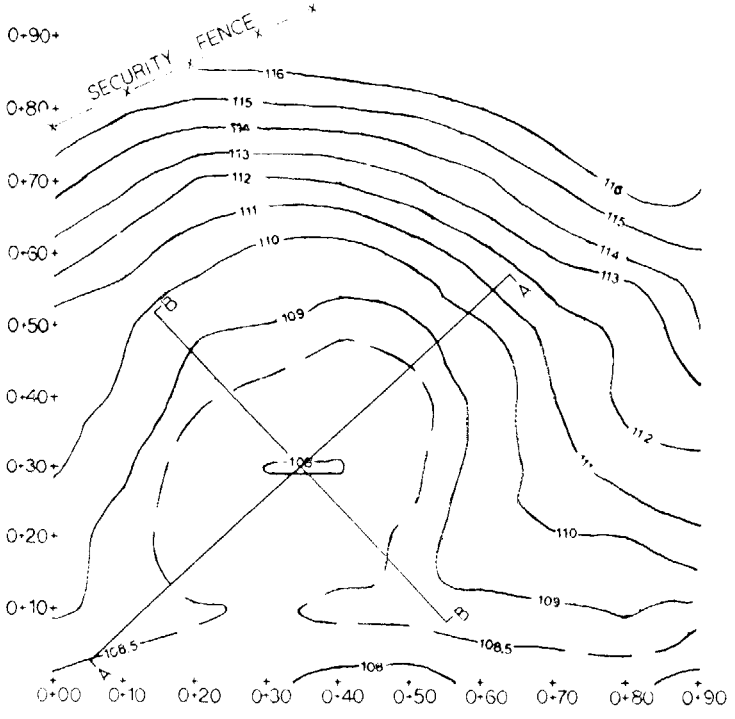

EAST CHESTNUT RIDGE SITE
SINKHOLE #02

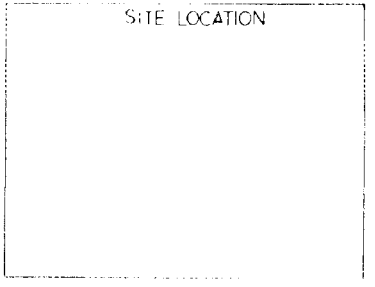

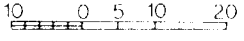

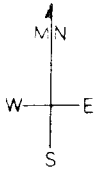

ELEVATIONS TO AN ARBITRARY DATUM

UNIVERSITY OF TENNESSEE	CONTOUR INTERVAL 1 FOOT		SEC.
SCALE: 1"=10'	DATE: 2/02/89	DRAWN BY: JESSEE SCARBOROUGH	CK BY:	NO. 02

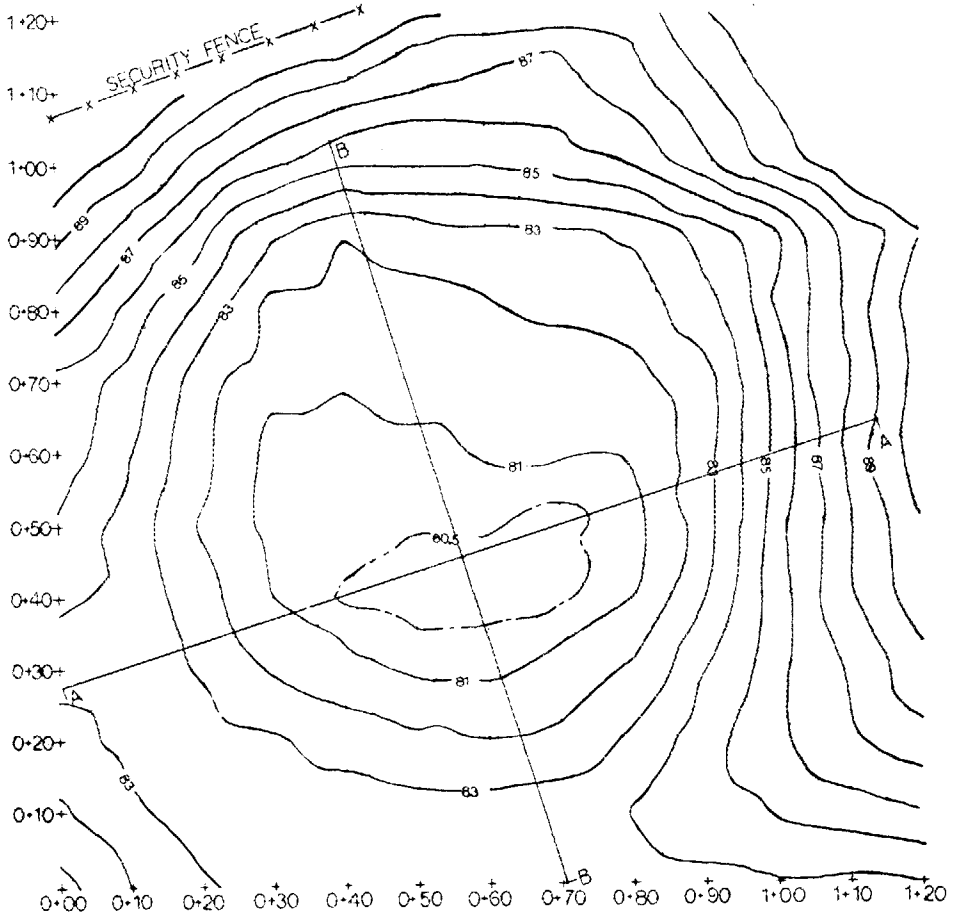

EAST CHESTNUT RIDGE SITE
SINKHOLE #03

SITE LOCATION

10 0 5 10 20

N
W E
S

ELEVATIONS TO AN ARBITRARY DATUM

UNIVERSITY OF TENNESSEE	CONTOUR INTERVAL 1 FOOT			SEC.
SCALE: 1"=10'	DATE: 3/15/89	DRAWN BY: JESSEE SCARBOROUGH	CK BY:	NO. 03

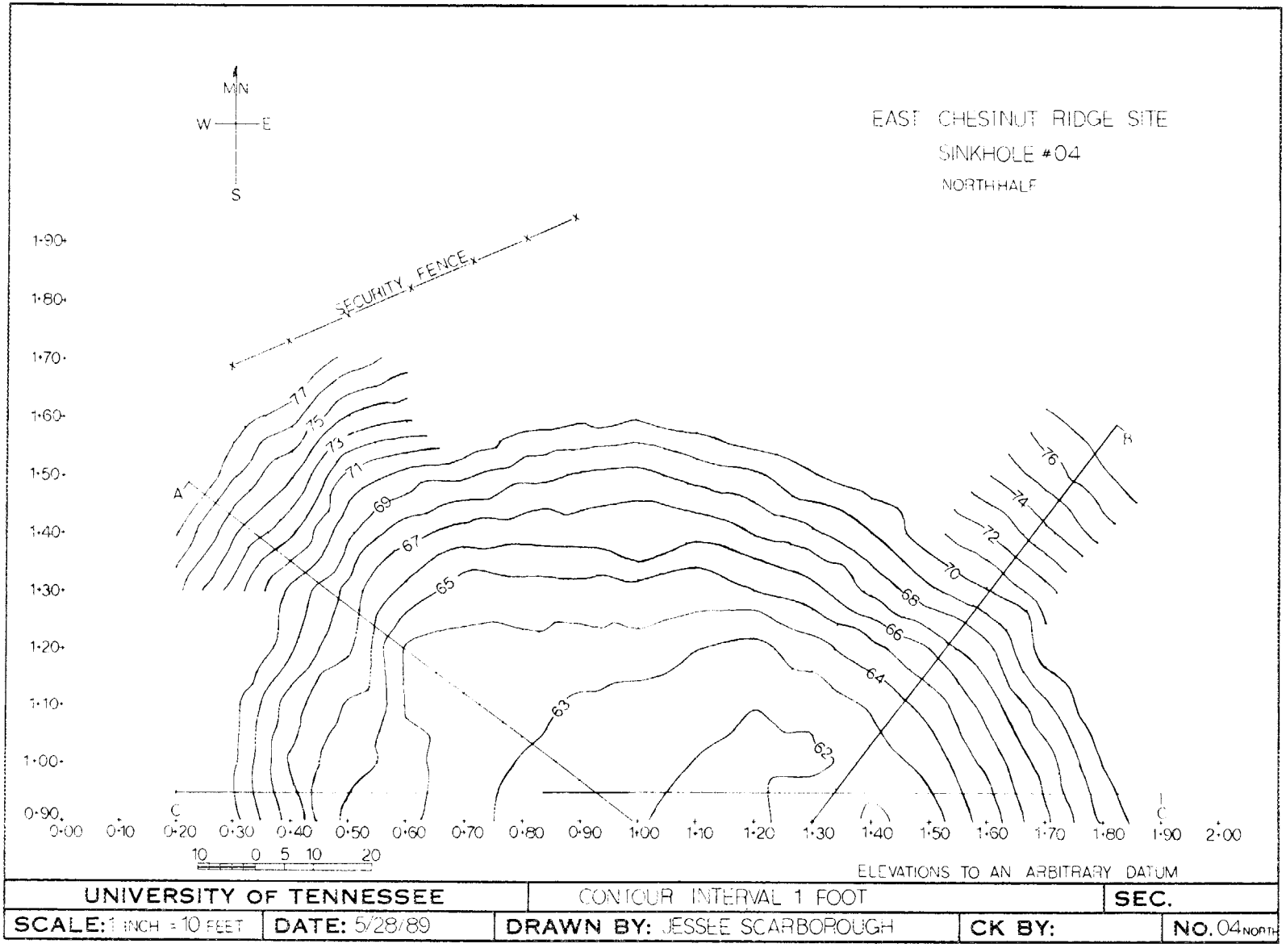
N
W
E
S
EAST CHESTNUT RIDGE SITE
SINKHOLE #04
NORTH HALF
SECURITY FENCE
A
B
C
C
77
75
73
71
69
67
65
63
62
70
68
66
64
76
74
72
1·90
1·80
1·70
1·60
1·50
1·40
1·30
1·20
1·10
1·00
0·90
0·00
0·10
0·20
0·30
0·40
0·50
0·60
0·70
0·80
0·90
1·00
1·10
1·20
1·30
1·40
1·50
1·60
1·70
1·80
1·90
2·00
10 0 5 10 20
ELEVATIONS TO AN ARBITRARY DATUM
UNIVERSITY OF TENNESSEE
CONTOUR INTERVAL 1 FOOT
SEC.
SCALE: 1 INCH = 10 FEET
DATE: 5/28/89
DRAWN BY: JESSEE SCARBOROUGH
CK BY:
NO. 04 NORTH

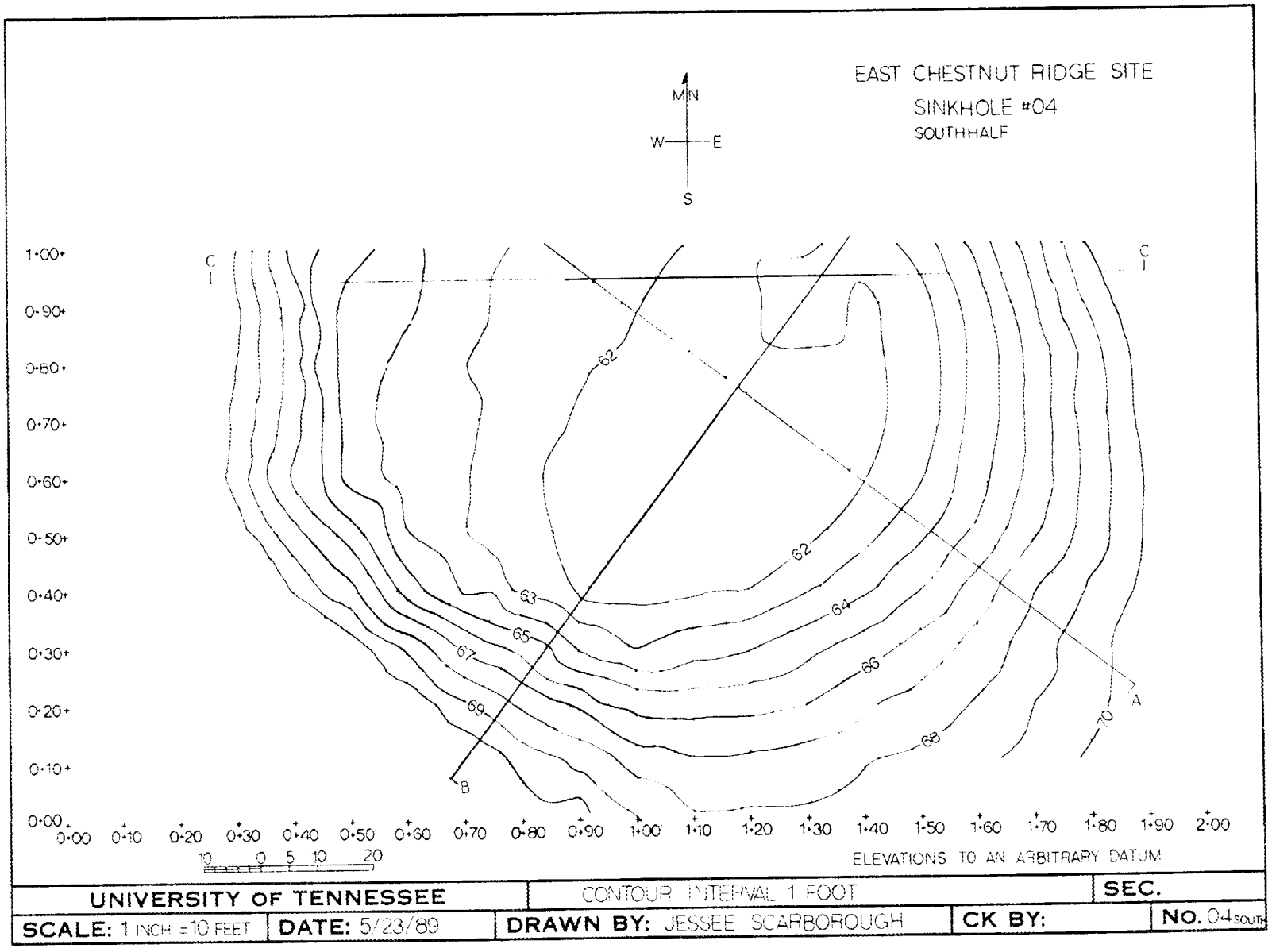

UNIVERSITY OF TENNESSEE	CONTOUR INTERVAL 1 FOOT		SEC.
SCALE: 1 INCH = 10 FEET	DATE: 5/23/89	DRAWN BY: JESSEE SCARBOROUGH	CK BY:	NO. 04 SOUTH

EAST CHESTNUT RIDGE SITE
SINKHOLE #06

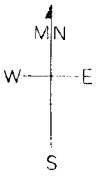

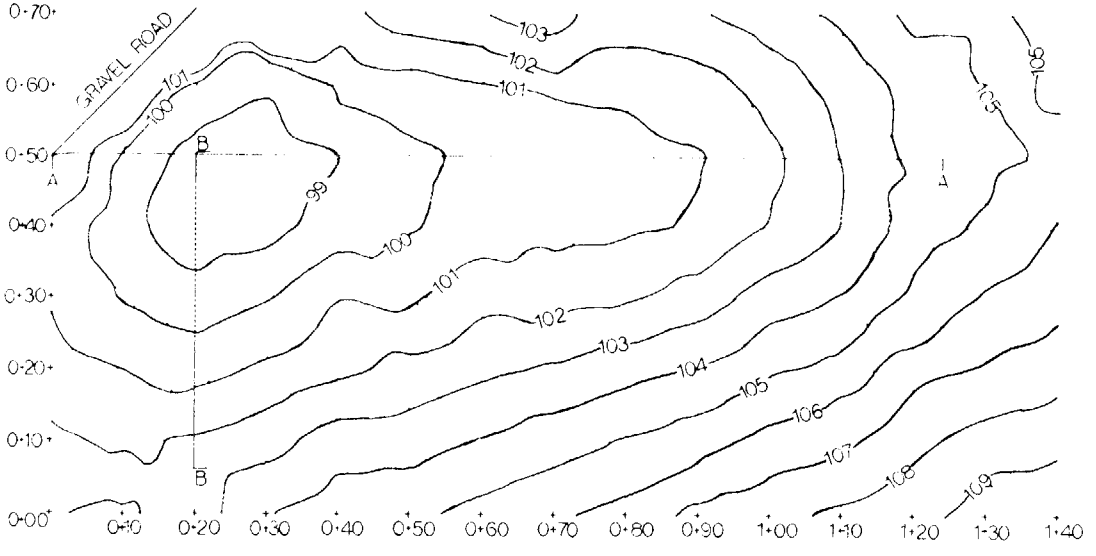

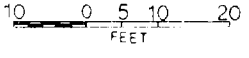

ELEVATIONS TO AN ARBITRARY DATUM

UNIVERSITY OF TENNESSEE	CONTOUR INTERVAL 1 FOOT		SEC.
SCALE: 1 INCH = 10 FEET	DATE: 6/1/89	DRAWN BY: JESSEE SCARBOROUGH	CK BY:	NO. 06

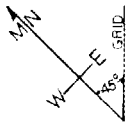

EAST CHESTNUT RIDGE SITE
SINKHOLE #07
"SADDLE"

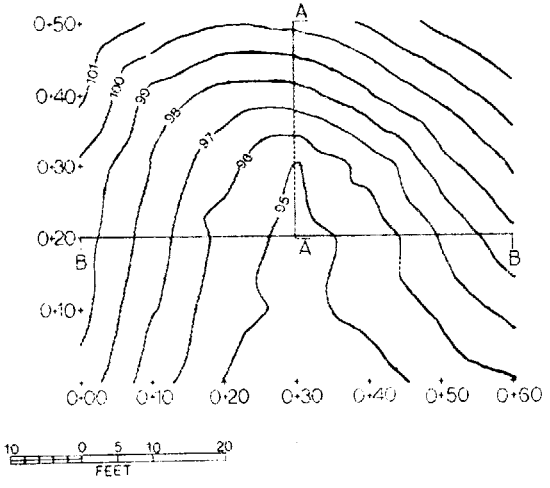

ELEVATIONS TO AN ARBITRARY DATUM

UNIVERSITY OF TENNESSEE		CONTOUR INTERVAL 1 FOOT		SEC.
SCALE: 1 INCH =10 FEET	DATE: 7/13/89	DRAWN BY: JESSEE SCARBOROUGH	CK BY:	NO. 07

EAST CHESTNUT RIDGE SITE

SINKHOLE # 08

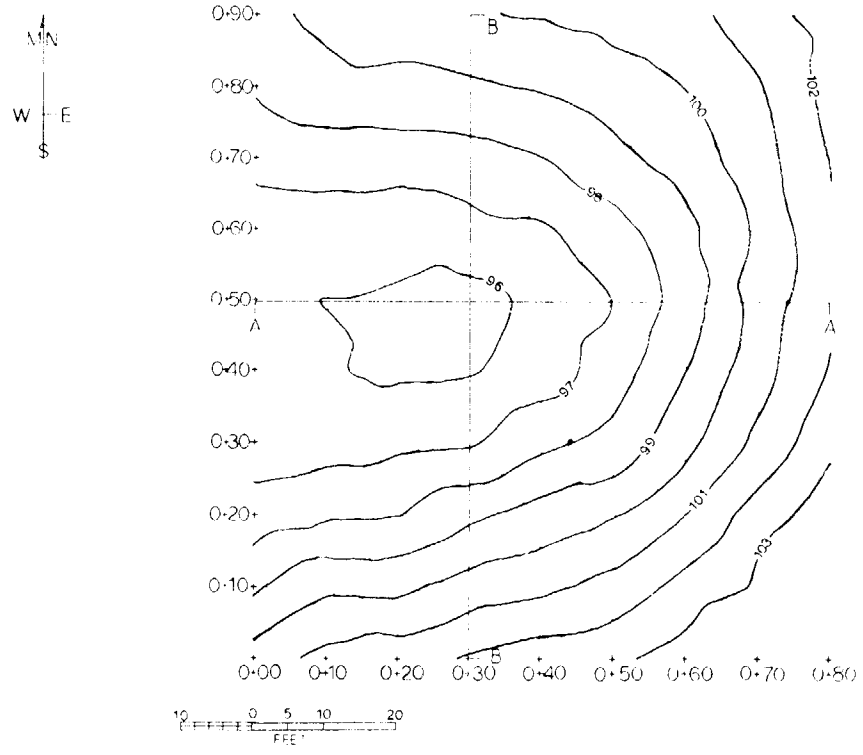

ELEVATIONS TO AN ARBITRARY DATUM

UNIVERSITY OF TENNESSEE	CONTOUR INTERVAL 1 FOOT		SEC.
SCALE: 1 INCH = 10 FEET	DATE: 7/17/89	DRAWN BY: JESSEE SCARBOROUGH	CK BY:	NO. 08

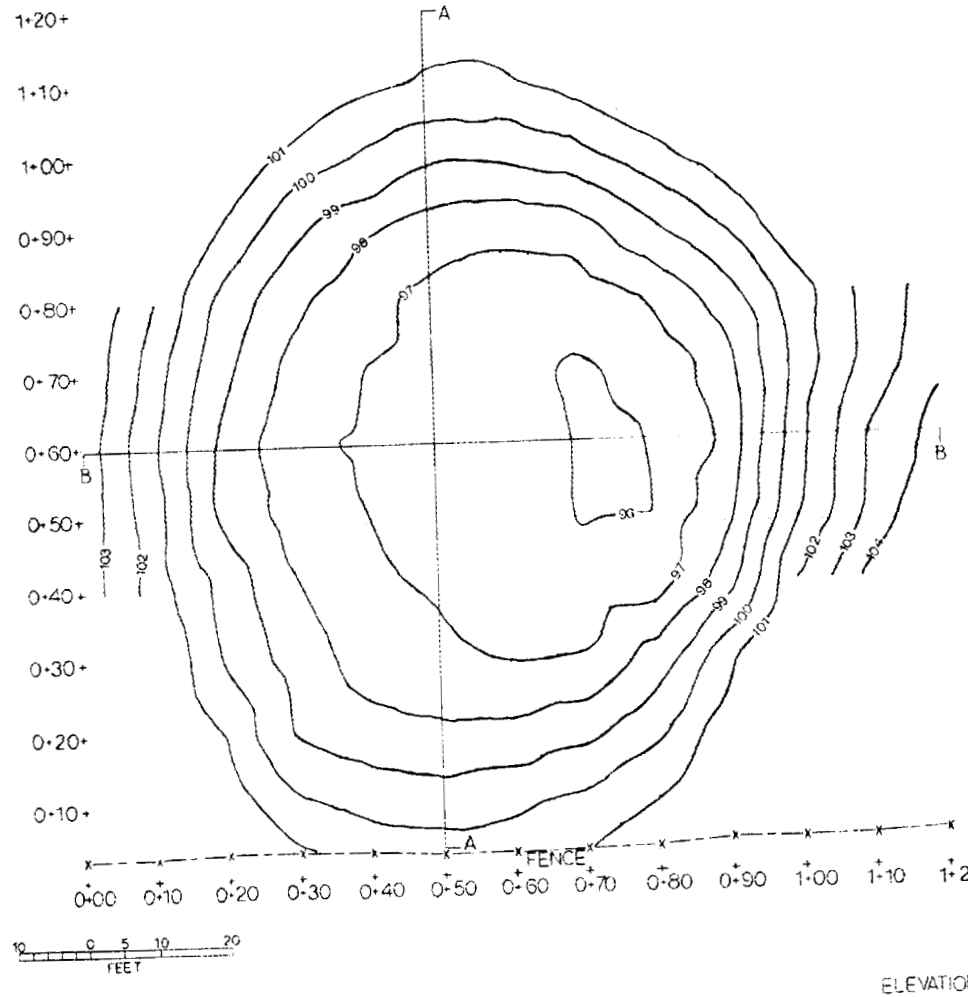

UNIVERSITY OF TENNESSEE	CONTOUR INTERVAL 1 FOOT			SEC.
SCALE: 1 INCH = 10 FEET	DATE: 7/23/89	DRAWN BY: JESSEE SCARBOROUGH	CK BY:	NO. 09

EAST CHESTNUT RIDGE SITE

SINKHOLE #11

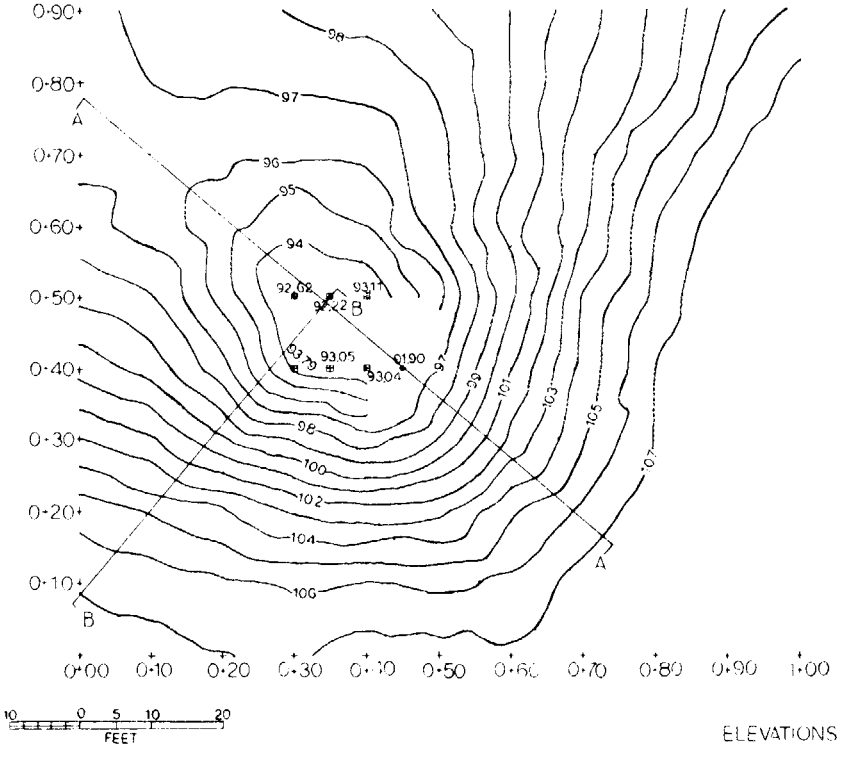

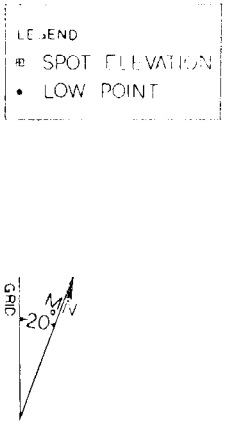

ELEVATIONS TO AN ARBITRARY DATUM

UNIVERSITY OF TENNESSEE	CONTOUR INTERVAL 1 FOOT		SEC.
SCALE: 1 INCH = 10 FEET	DATE: 7/26/89	DRAWN BY: JESSEE SCARBOROUGH	CK BY:	NO. 11

APPENDIX B: DETERMINATION OF CAP MODEL PARAMETERS

In numerical analysis techniques, such as the finite element method, the stresses within the system are related to the calculated strains through a material, or constitutive, model. Constitutive models vary widely in terms of their ability to represent observed material behavior. Generally, improved representations of material response are accompanied by increased complexity in both the model and the numerical solution. However, the choice of material model and the values chosen for the material parameters can significantly affect the results of a numerical analysis.

Depending on the location within a soil mass, an element of soil may undergo a wide range of stress paths or loading histories. Because the behavior of most geologic materials is stress-path dependent, the use of a constitutive model capable of representing stress-path dependency is important.

Unlike piecewise linear elastic models that are essentially curve-fitting models, an incremental elastic-plastic model can represent different types of response when loaded or unloaded under different stress paths. In addition, the nonlinear, inelastic, strain hardening response observed in most geologic materials may be represented. The Sandler cap model (DiMaggio and Sandler, 1971) used in this analysis has these important attributes. The cap model and the parameter determination process are briefly described in this Appendix.

The cap model can represent a range of different materials, depending on the values of the material parameters chosen. Typically, the parameters are determined from a series of laboratory tests conducted over several stress paths. This ensures that the material model can represent the behavior over a range of loading histories. The parameters are then used in the model to verify the laboratory test response. The parameters may be adjusted or calibrated to improve the predictive capability of the model. However, at some point, improvement in the response over one stress path is usually obtained at the expense of the behavior over another stress path.

Determination of Material Constants

As a minimum, a series of triaxial compression tests and one hydrostatic stress test are required to properly determine the material parameters. Drained tests with volumetric measurements are required, and triaxial extension tests are often desirable. In this investigation, a series of drained triaxial tests with volume change measurements and undrained tests with pore pressure measurements (Geologic Associates, 1989) were used for the determination of the material parameters. A total of four drained tests and three undrained tests were conducted. The shear stresses at failure are summarized in Fig. B.1. The stresses plotted in terms of the stress invariants J_1 and $\sqrt{J_{2d}}$ were as follows:

$$J_1 = \sigma_1 + \sigma_2 + \sigma_3 \quad , \tag{B.1}$$

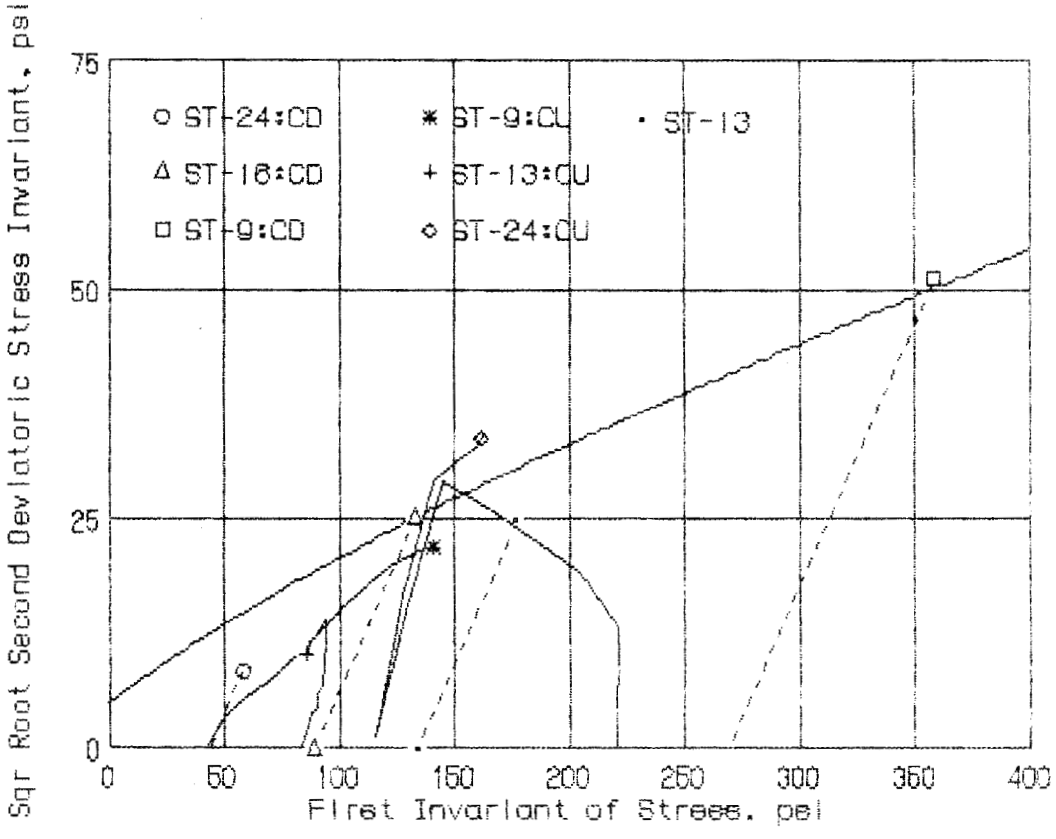

Fig. B.1. Shear strength of undisturbed samples in stress invariant space.

$$J_{2d} = \frac{1}{6}\left[(\sigma_1 - \sigma_2)^2 + (\sigma_2 - \sigma_3)^2 + (\sigma_1 - \sigma_3)^2\right] , \qquad \text{(B.2)}$$

and

σ_1, σ_1, σ_3 = principal stresses.

The values for the parameters used in the analysis are provided in Table B.1. The parameter determination process is described below.

Table B.1. Summary of cap model parameters

E = 1.532E+5 kPa	μ = 0.30	γ = 18.81 kN/m^3
α = 103.4 kPa	β = 0.001279 kPa^{-1}	γ = 68.95 kPa
θ = 0.0997	T_{cut} = 50 kPa	
Z = 0.0 kPa	$XL_{initial}$ = 30 kPa	

Elastic Parameters

Young's modulus, E, is taken as 1530 MPa from the approximately linear, unloading portion of the triaxial data from Sample ST-9 shown in Fig. B.2. The unloading portion of the hydrostatic curve from samples ST-9 and ST-13 (Fig. B.3) yields a value of the bulk modulus, K = 120.6 MPa. Thus, Poisson's ratio, μ, is determined as:

$$\mu = \frac{1}{2}\left(1 - \frac{E}{3K}\right) = 0.29 \quad or \quad 0.3 \quad . \tag{B.3}$$

The parameters E and μ are sufficient to describe the linear elastic components of the stress-strain relationship.

Fixed Failure Surface

The stresses at failure obtained from the triaxial tests are used to determine a fixed failure surface, F_1, in the J_1- $\sqrt{J_{2d}}$ stress space (Fig. B.1) where:

$$F_1(J_1, \sqrt{J_{2d}}) = \sqrt{J_{2d}} - [\alpha - \gamma\, e^{(\beta J_1)} - \theta J_1] \quad , \tag{B.4}$$

where α,β,θ, and γ are material parameters. The function F_1, used in the analysis, is superimposed on the laboratory data in Fig. B.1. The $\sqrt{J_{2d}}$ intercept of the function F_1 corresponds to the difference α - γ . This results in the formation of a tension zone where the function F_1 is less than zero. An additional parameter T_{cut} is a tension cut-off utilized to limit the magnitude of the tensile stresses that can develop in the soil. A value of T_{cut} = 50 kPa was used in this analysis. Note that the model slightly overestimates the shear strength at low values of J_1.

Plasticity Parameters and Hardening Yield Surface

An elliptical yield cap, which translates with the stress point in stress space during loading, defines the strain hardening response of the soil. This cap is the yield function F_2, expressed as an ellipse in the stress invariant space and is defined as:

$$F_2(J_1, \sqrt{J_{2d}}, \kappa) = \sqrt{J_{2d}} - \frac{1}{R}\{[X(\kappa) - L(\kappa)]^2 - [J_1 - L(\kappa)]^2\}^{\frac{1}{2}}, \tag{B.5}$$

where

R = the aspect ratio of the elliptical cap surface
$X(\kappa)$ = the J_1 value at which the current cap intersects the J_1 axis
$L(\kappa)$ = the J_1 value at which the current cap intersects the fixed failure surface, F_1
κ = the hardening parameter.

The value of $X(\kappa)$, which corresponds to the position of the cap, depends on the plastic volumetric strain and is expressed as:

$$X(\kappa) = -\frac{1}{D}\ln\left(1 - \frac{\varepsilon_{vol}^{P}}{W}\right) + Z \quad , \tag{B.6}$$

where D, W, and Z are material parameters. The location of the initial hardening cap is defined by parameter Z, which is the value of J_1 at the intersection of the J_1 axis and the initial cap. Parameter Z is related to the preconsolidation stress in the soil. As in analysis described here, Z is often assumed to be zero, resulting in the development of plastic strains from the onset of loading.

The hardening parameter κ is implicitly defined as a function of the plastic volumetric strain by the following hardening rule:

$$\varepsilon_{vol}^{P} = W\left[e^{D\,X(\kappa)} - 1\right] \quad . \tag{B.7}$$

Hydrostatic test data are used to determine the values for D and W, which govern the magnitude volumetric plastic strain. Parameter W is taken as the value of strain asymptotically approached by a hydrostatic sample at large stresses.

From Fig. B.3, the constant W is estimated to be 7% or 0.07 m/m. Knowing W and Z, constant D is then determined by a trial and error process to provide a satisfactory fit to the hydrostatic data. A value of $D = 0.001$ kPa^{-1} was selected to represent the range of response exhibited in Fig. B.3.

The aspect ratio of the yield cap, represented by parameter R, governs the relative magnitudes of the volumetric and deviant plastic strains, and plays an important role in the behavior of the model. To determine parameter R, contours of equal volumetric plastic strain are plotted in the invariant stress space. These contours define yield surfaces and can be approximated by a family of ellipses. The aspect ratio of the ellipses, which corresponds to parameter R, was found to vary from less than 2 to greater than 4. Consequently, the parameter calibration process or tuning of the model was concentrated on parameter R.

Calibration of Cap Model Parameters

With the initial estimates of the cap model parameters, the model was calibrated by performing a series of finite element analyses on idealizations of the laboratory tests. Based on a comparison of the stress-strain response of the laboratory data and that predicted by the finite element analysis, a value of $R = 6.0$ was chosen. No other parameters were modified. The performance of the material model with the selected parameters can be evaluated by comparing the laboratory stress-strain response with that predicted by a finite element analysis of laboratory tests.

The final finite element prediction of the hydrostatic compression response is shown with the actual data in Fig. B.3. The model parameters were selected to best represent the range of hydrostatic response observed in the laboratory. A prediction of the conventional triaxial compression test with a confining stress of 621 kPa (90 psi) is provided in Fig. B.2. A similar comparison with a confining stress of 207 kPa (30 psi) is shown in Fig. B.4. Considering the variations in the observed test data, the predictions can be considered to be excellent. Fig. B.5 compares the stress-strain response of three finite element idealizations at different confining stresses. It should be noted that the finite element prediction at a confining stress of 103 kPa (15 psi) indicates a shear strength of about 200 kPa (29 psi), which is somewhat greater than that measured in the laboratory test ST-24, Fig. B.1. This is because of the difference between the chosen ultimate failure function F_1 and the measured failure stresses at low confining pressures.

Note that the cap model captures the unloading-reloading response of the triaxial test ST-9, Fig. B.2. This unloading can occur around the void in the residual soil as the stresses are redistributed and must be properly represented in the material model.

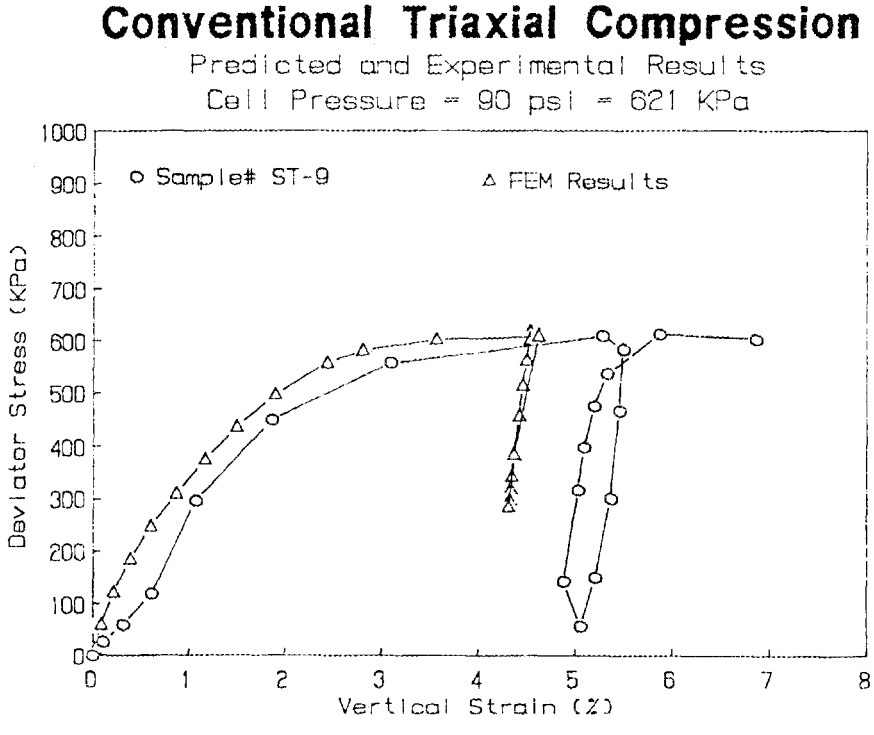

Fig. B.2. Deviator stress-axial strain response, sample ST-9.

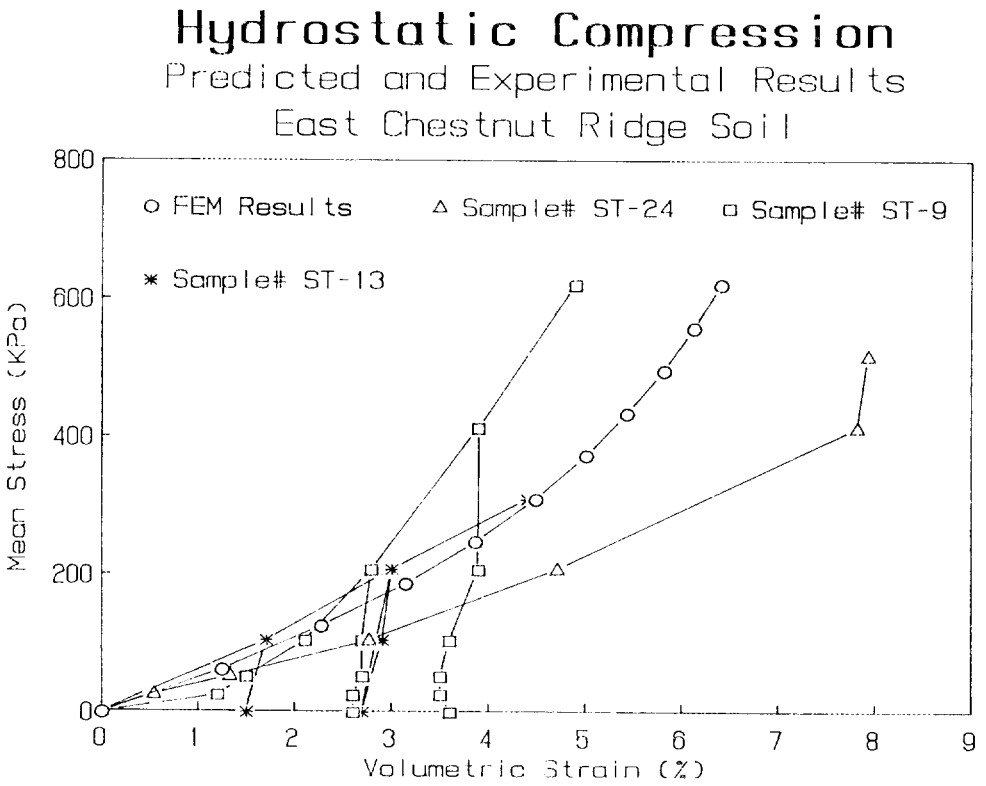

Fig. B.3. Hydrostatic stress-volumetric strain response.

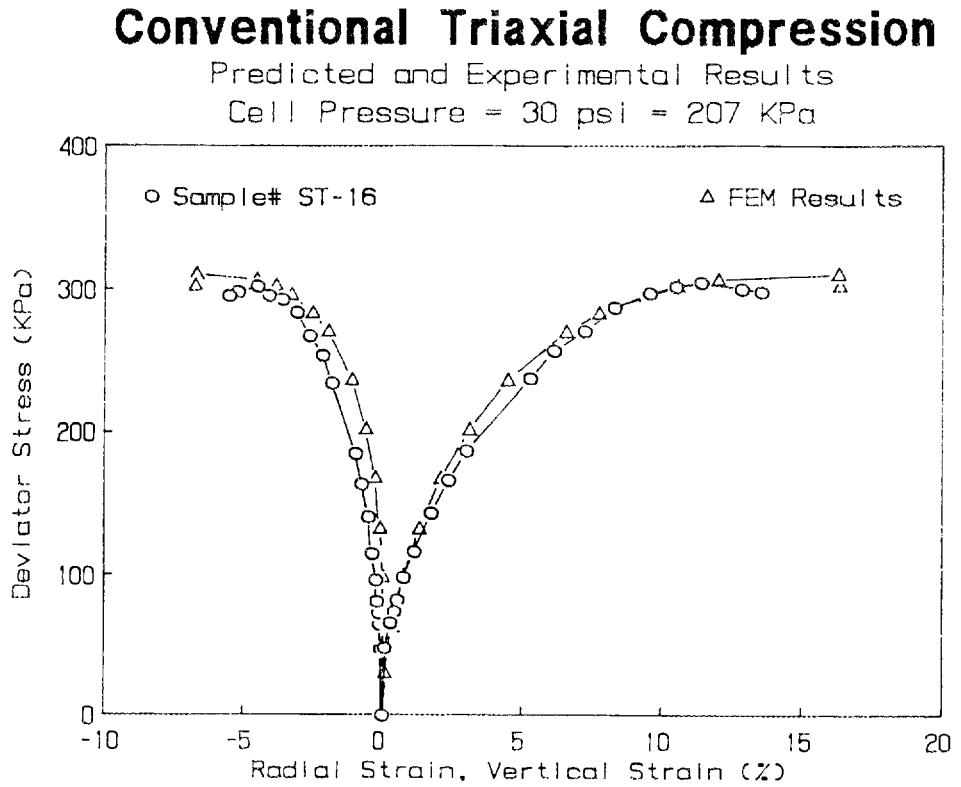

Fig. B.4. Deviator stress-axial strain response for sample ST-16.

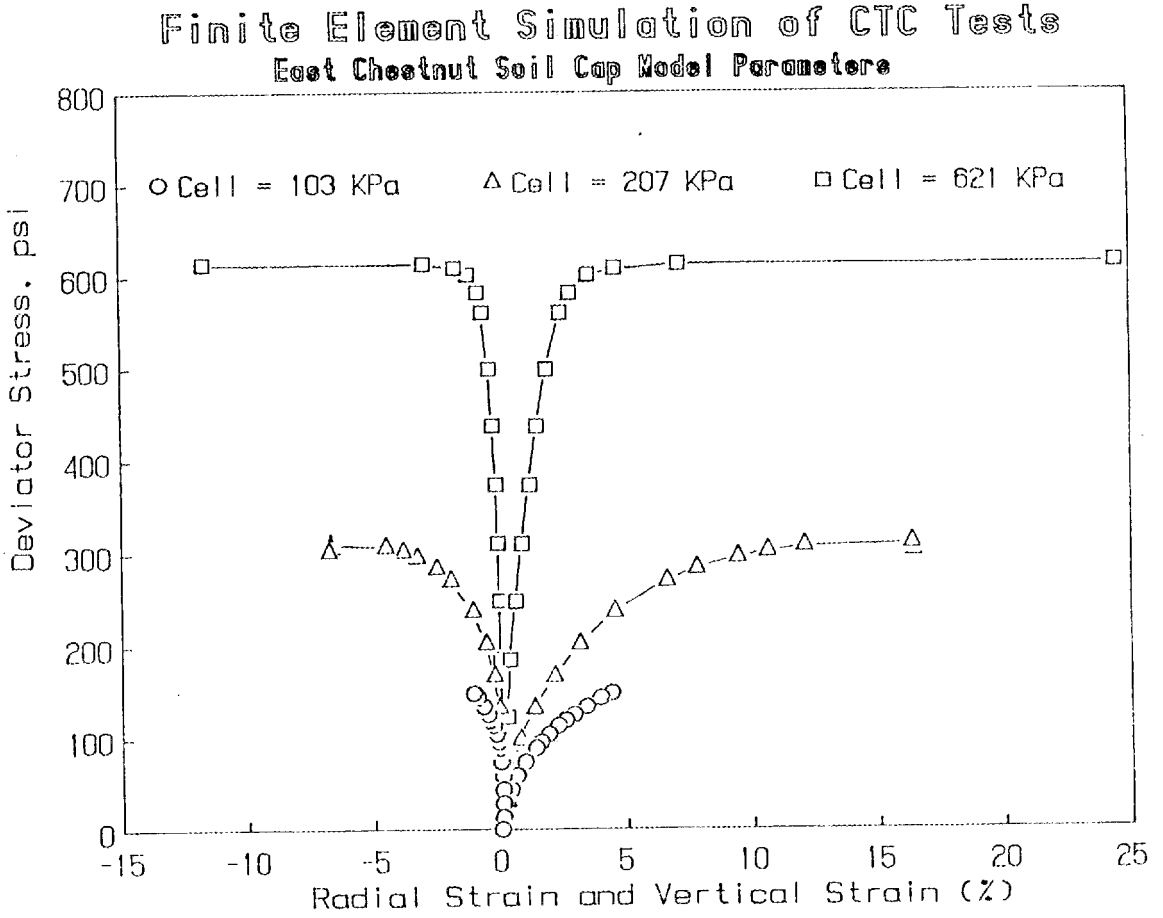

Fig. B.5. Finite element simulation of triaxial response.

APPENDIX C: SUMMARY OF ANALYSIS RESULTS—EMPIRICAL AND GEOMETRIC PARAMETERS

C-1 Field profiles and the exponential function

Profile	S_o (m)	L (m)	α	β	R^2
01 west	1.28	15.2	4.35	4.44	0.997
01 east	1.31	15.2	3.78	4.82	0.996
01 south	0.88	10.7	4.38	3.24	0.974
01 north	1.04	15.2	2.93	2.59	0.973
02 west	0.23	9.1	2.65	3.82	0.957
02 east	2.44	18.3	3.06	3.87	0.996
02 south	0.20	6.7	3.15	3.11	0.997
02 north	1.53	15.2	2.96	3.31	0.978
03 west	0.94	15.2	4.16	4.11	0.998
03 east	2.61	18.3	2.76	4.27	0.994
03 south	0.96	12.2	3.65	3.40	0.994
03 north	2.59	21.3	2.44	5.47	0.987
04 west	4.68	30.5	3.15	3.69	0.995
04 east	2.57	22.9	3.01	6.64	0.994
04 south	2.57	24.4	3.30	3.53	0.999
04 north	4.69	36.6	2.76	5.21	0.983
06 east	2.08	34.23	2.07	2.32	0.942
06 south	1.22	13.08	2.95	3.33	0.995
06 west	1.17	5.85			
07 north	1.74	8.81	3.44	4.15	0.999
07 east	1.26	8.75	2.78	2.82	0.995
07 west	1.49	8.81	2.53	2.46	0.988
08 west	0.30	8.53	2.69	1.33	0.992
08 east	1.87	14.51	2.54	2.79	0.987
08 north	1.31	11.61	2.21	1.78	0.971
08 south	1.96	14.63	2.62	2.92	0.995
09 north	1.45	16.58	3.46	4.69	0.999
09 south	1.20	16.98	2.39	4.47	0.989
09 east	2.58	20.45	3.77	5.78	0.990
09 west	2.21	14.81	2.56	4.02	0.991
10 south	5.40	63.79	2.40	4.11	0.968
10 north	1.67	23.53	2.35	3.08	0.991
10 north/east	2.55	35.30	2.50	2.74	0.996
10 north/west	1.12	29.32	1.99	2.37	0.956

Table C.1 (continued)

Profile	S_0 (m)	L (m)	α	β	R^2
10 south/east	2.26	23.16	2.54	2.31	0.993
10 south/west	5.14	46.24	2.52	3.51	0.997
11 north	1.23	9.75	2.85	1.87	0.995
11 south	4.60	14.26	2.97	2.45	0.972
11 west	4.50	14.48	2.84	1.91	0.999
Average all profiles:			2.93	3.49	
Composite best fit:			2.50	3.30	0.926

Table C.2. Field profiles and the hyperbolic function

Profile	S_0 (m)	B (m)	C	R^2
01 west	1.28	10.00	3.36	0.996
01 east	1.31	10.85	3.67	0.990
01 south	0.88	6.37	2.42	0.970
01 north	1.04	9.54	2.07	0.961
02 west	0.23	6.49	2.65	0.956
02 east	2.44	12.53	2.84	0.994
02 south	0.20	4.15	2.32	0.995
02 north	1.53	10.24	2.54	0.975
03 west	0.94	10.03	3.10	0.995
03 east	2.61	13.47	3.21	0.987
03 south	0.96	7.77	2.67	0.990
03 north	2.59	16.98	3.99	0.983
04 west	4.68	20.30	2.69	0.995
04 east	2.57	18.23	4.83	0.993
04 south	2.57	15.73	2.65	0.997
04 north	4.69	28.41	3.78	0.978
06 east	2.08	24.38	1.90	0.914
06 south	1.22	8.96	2.63	0.985
06 west	1.17	3.78	2.30	0.989
07 north	1.74	5.97	3.28	0.998
07 east	1.26	5.36	2.09	0.994
07 west	1.49	5.33	1.86	0.987
08 west	0.30	3.05	1.05	0.956
08 east	1.87	9.51	2.12	0.986
08 north	1.31	6.68	1.44	0.971
08 south	1.96	9.24	2.16	0.993
09 north	1.45	11.80	3.50	0.998
09 south	1.20	13.11	3.34	0.983
09 east	2.58	14.94	4.37	0.990
09 west	2.21	10.82	2.94	0.988
10 south	5.40	48.49	2.92	0.964
10 north	1.67	16.34	2.32	0.987
10 north/east	2.55	21.70	2.00	0.992
10 north/west	1.12	18.99	1.69	0.971

Table C.2. (continued)

Profile	S_0 (m)	B (m)	C	R^2
10 south/east	2.26	13.53	1.74	0.995
10 south/west	5.14	32.10	2.59	0.996
11 north	1.23	4.48	1.46	0.981
11 south	4.60	7.35	1.70	0.952
11 west	4.50	6.92	1.40	0.993
Average all profiles:			2.60	
Composite best fit:			2.63	0.967

Table C.3. Hyperbolic model profiles, geometric parameters

Profile (m)	r/H	S_0 (m)	L (m)	B (m)
r = 0.3, H = 15.0	0.0200	0.001	20.85	10.5
= 22.5	0.0130	0.003	31.08	16.3
= 30.0	0.0100	0.005	41.57	22.2
= 37.5	0.0080	0.007	54.98	28.8
= 45.0	0.0067	0.008	68.14	35.8
r = 0.6, H = 15.0	0.0400	0.006	20.90	10.3
= 22.5	0.0267	0.012	31.35	15.8
= 30.0	0.0200	0.019	41.86	21.4
= 37.5	0.0160	0.020	56.49	28.5
= 45.0	0.0133	0.031	68.20	35.0
r = 1.0, H = 15.0	0.0667	0.019	21.08	9.9
= 22.5	0.0444	0.036	31.52	18.3
= 30.0	0.0333	0.058	42.21	20.5
= 37.5	0.0267	0.084	55.99	22.6
= 45.0	0.0222	0.076	67.55	33.4
r = 2.0, H = 15.0	0.1333	0.158	19.08	8.7
= 22.5	0.0889	0.432	26.99	10.5
= 30.0	0.0667	0.882	35.34	13.7
= 37.5	0.0533	0.721	50.25	18.9
= 45.0	0.0444	0.429	65.55	28.7
r = 4.0, H = 15.0	0.2667	6.904	15.46	8.7
= 22.5	0.1778	6.677	23.83	13.7
= 30.0	0.1333	7.001	29.25	15.0
= 37.5	0.1067	19.080	41.11	20.5
= 45.0	0.0889	20.760	41.59	24.8

Table C.4. Cap model profiles, geometric parameters

Profile (m)	r/H	S_0 (m)	L (m)	B (m)
r = 0.3, H = 15.0	0.0200	0.029	10.38	8.57
= 22.5	0.0130	0.021	10.74	8.50
= 30.0	0.0100	0.019	15.95	9.19
= 37.5	0.0080	0.016	19.32	9.98
= 45.0	0.0067	0.013	22.50	12.01
r = 0.6, H = 15.0	0.0400	0.032	5.57	4.20
= 22.5	0.0267	0.047	10.75	5.06
= 30.0	0.0200	0.055	13.49	6.40
= 37.5	0.0160	0.054	24.94	8.40
= 45.0	0.0133	0.048	21.35	10.42
r = 1.0, H = 15.0	0.0667	0.036	8.38	3.66
= 22.5	0.0444	0.056	10.32	6.42
= 30.0	0.0333	0.066	9.11	7.10
= 37.5	0.0267	0.107	16.82	6.47
= 45.0	0.0222	0.108	16.45	9.04
r = 2.0, H = 15.0	0.1333	0.106	3.89	2.47
= 22.5	0.0889	0.119	7.87	3.79
= 30.0	0.0667	0.160	11.53	5.46
= 37.5	0.0533	0.193	15.02	7.69
= 45.0	0.0444	0.205	18.38	9.56
r = 3.0, H = 15.0	0.2000	0.204	9.90	3.42
= 22.5	0.1333	0.241	8.22	2.22
= 30.0	0.1000	0.170	11.28	6.39
= 37.5	0.0800	0.260	18.21	7.13
= 45.0	0.0667	0.274	18.67	10.68
r = 4.0, H = 15.0	0.2667	0.322	10.69	4.78
= 22.5	0.1778	0.595	11.29	3.94
= 30.0	0.1333	0.373	11.51	4.91
= 37.5	0.1067	0.336	14.27	9.33
= 45.0	0.0889	0.368	19.13	9.73

INTERNAL DISTRIBUTION

1. Bailey, J. K.
2. Baldwin, J. S.
3. Barton, W. D.
4. Beavers, J. E.
5. Burke, S. A.
6. Cannon, J. B.
7. Dreier, R. B.
8. Early, T. O.
9. Haase, C. S.
10. Hatcher, R. D.
11. Howard, S. C.
12. Huff, D. D.
13. Jernigan, D. G.
14. Johnson, R. O.
15. Jones, L. S.
16. Jones, S. B.
17–21. Ketelle, R. H.
22. King, H. L.
23. Kuliasha, M. A.
24. Lee, D. W.
25. Lee, R. R.
26. Lee, S. Y.
27. Manrod, W. E.
28. McMaster, W. M.
29. Mezga, L. J.
30. Moore, G. K.
31. Myrick, T. E.
32–36. Owen, P. T.
37. Pierce, T. J.
38. Reichle, D. E.
39. Rizk, T. A.
40. Selfridge, R.
41. Shelton, R. B.
42. Staub, W. P.
43. Stow, S. H.
44. Witten, A. J.
45. ORNL Patent Office
46. Central Research Library
47. Document Reference Section
48–50. Lab Records
51. Lab Records—Record Copy

EXTERNAL DISTRIBUTION

52. Dr. Bruce G. Buchanan, Computer Sciences Department, University of Pittsburgh, 206 Mineral Industries Building, Pittsburgh, PA 15260

53. Mr. John J. Cuttica, Vice President, End Use, Research and Development, Gas Research Institute, 8600 W. Bryn Mawr Avenue, Chicago, IL 60631

54. Dr. Allan Hirsch, President, Dynamac Corporation, The Dynamac Building, 11140 Rockville Pike, Rockville, MD 20852

55. Dr. Denton E. Morrison, 333 Oxford Road, East Lansing, MI 48823

56. Dr. Martin Williams, Professor, Department of Economics, Northern Illinois University, DeKalb, Il 60115

57–66. OSTI, U.S. Department of Energy, P.O. Box 62, Oak Ridge, TN 37831

67. C. T. Rightmire, CH2M Hill Corporation, 800 Oak Ridge Turnpike, Oak Ridge, TN 37831

68. Stan Crownover, Department of Soil Science, University of Florida, Gainesville, FL 32611.

69. David Lietzke, Route 3, Box 607, Rutledge, TN 37861

70–74. E. C. Drumm, Department of Civil Engineering, University of Tennessee, Knoxville, TN 37996-2010

75–79. W. F. Kane, Department of Civil Engineering, University of Tennessee, Knoxville, TN 37996-2010

80–81. J. Ben-Hassine, Department of Civil Engineering, University of Tennessee, Knoxville, TN 37996-2010

82–83. J. Scarborough, ERC/EDGE, 725 Pellissippi Parkway, Knoxville, TN 37933-0879.

84. Office of Assistant Manager for Energy Research and Development, DOE-ORO, P.O. Box 2001, Oak Ridge, TN 37831-8600